Ultra Fast Beam Loss Mechanisms at the LHC and their Detection for Use in Machine Protection

Dissertation

zur Erlangung des Doktorgrades
an der Fakultät für
Mathematik, Informatik und Naturwissenschaften
Fachbereich Physik
der Universität Hamburg

vorgelegt von

Oliver Stein

Hamburg

2017

Erklärung der Urheberschaft

Ich erkläre hiermit an Eides statt, dass ich die vorliegende Arbeit ohne Hilfe Dritter und ohne Benutzung anderer als der angegebenen Hilfsmittel angefertigt habe.

Genf, den 20.11.2017   Unterschrift:

Liste der aus dieser Dissertation hervorgegangenen Vorveröffentlichungen

Konferenzbeiträge

- O. Stein, et al, "Investigation of Injection Losses at the Large Hadron Collider with Diamond Based Particle Detectors", Proceedings of IPAC16, Busan, South Korea, 2016

- F. Burkart, O. Stein, et al, "Beam Losses at CERNs PS and SPS Measured with Diamond Particle Detector", Proceedings of IPAC16, Busan, South Korea, 2016

- O. Stein, et al, "Response of Polycrystalline Diamond Particle Detectors Measured with a High Intensity Electron Beam", Proceedings of IPAC15, Richmond, Virginia, USA, 2015

- O. Stein, et al, "Feasibility Study of Monitoring the Population of the CERN-LHC Abort Gap with Diamond Based Particle Detector", Proceedings of IPAC15, Richmond, Virginia, USA, 2015

- F. Burkart, O.Stein, et al, "Experimental Results from the Characterization of Diamond Particle Detectors with a High Intensity Electron Beam", Proceedings of IPAC14, Dresden, Germany, 2014

Berichte

- O. Stein, et al, "MD456: Monitoring of abort gap population with diamond particle detectors at the BGI in IP 4", CERN-ACC-2016-0011, CERN, Geneva, Switzerland, 2016

- O. Stein, et al, "Injection quality measurements with diamond based particle detectors", CERN-ACC-NOTE-2016-0021, CERN, Geneva, Switzerland, 2016

Zusammenfassung

Im Large Hadron Collider (LHC) werden Protonenstrahlen mit Intensitäten von mehr als 3.2×10^{14} Teilchen pro Strahl auf bis zu 7 TeV beschleunigt. Bei maximaler Energie und Intensität sind 362 MJ pro Protonstrahl gespeichert. Der Verlust von hoch energetischen Teilchen führt zu Energiedeposition in den Beschleunigerkomponenten. Schon der Verlust von Bruchteilen der gespeicherten Strahlenergie über eine kurze Zeit kann zum Verlust der Supraleitfähigkeit der Magnete führen, oder im schlimmsten Fall zu strukturellen Schäden. Daher werden die Strahlverluste während des Betriebs entlang des gesamten Beschleunigers genau beobachtet. Falls die Verluste vorher festgelegte Grenzwerte überschreiten wird ein Strahlabbruch eingeleitet. Die Teilchenstrahlen werden dann innerhalb von 270 µs sicher aus dem LHC extrahiert.

Während des Beschleunigerbetriebs wurden Teilchenverluste beobachtet, die schneller auftreten als die Strahlen aus dem LHC extrahiert werden können. Die Zeitstruktur dieser ultra schnellen Verluste kann mit den herkömmlichen Strahlverlustmonitoren nicht aufgelöst werden. Deshalb wurden im Rahmen dieser Arbeit diamantbasierte Verlustmonitore installiert, die eine zeitliche Auflösung im Nanosekundenbereich bieten und auf Grund eines weiten dynamischen Bereich die Erfassung von Signalen mit sehr unterschiedlichen Amplituden erlauben. Die Analyse des zeitlichen Verlustverlaufs gibt Aufschluss über die zu Grunde liegenden Verlustmechanismen.

In dieser Arbeit werden zunächst die Ergebnisse von Effizienzmessungen der diamantbasierten Detektoren präsentiert. Des Weiteren werden verschiedene Szenarien von ultra schnellen Verlusten und deren Ursachen vorgestellt. Im Speziellen werden Injektionsverluste betrachtet, die auf Grund ihrer hohen Teilchenverlustraten Strahlabbrüche ausgelöst und somit den Beschleunigerbetrieb beeinträchtigt haben. Die Messungen haben zum ersten Mal im Detail gezeigt, dass der ankommende Strahl vor und nach dem eigentlich zu injizierenden Zug von Teilchenpaketen weitere ungewollte Teilchen aufweist. Diese passieren die Injektionsmagnete, während sich die Felder dieser Magnete verändern. Die resultierende fehlerhafte Ablenkung der Teilchen führt zu deren Verlust an den Absorberblöcken in der Injektionsregion. Als eine weitere Ursache für Injektionsverluste sind Teilchen, die außerhalb der bereits gefüllten Regionen im LHC zirkulieren. Diese passieren die Injektionsmagnete während der Injektion des neu ankommenden Strahls und werden durch die Magnetfelder abgelenkt. Basierend auf den in dieser Arbeit identifizierten Verlustmechanismen wurden Techniken entwickelt, die in den Betriebsablauf des LHC mit aufgenommen wurden und in einer Reduzierung der Injektionsverluste von einer Größenordnung resultierten.

Abstract

At the Large Hadron Collider (LHC) high intensity proton beams are accelerated up to 7 TeV resulting in 362 MJ of stored energy in each beam. Losses of high energetic beam particles lead to energy deposition in the accelerator components. The deposition of a fraction of the total beam energy over a short time in the accelerator components can cause quenches in the superconducting magnets and in the worst case result in structural damage. Therefore, the beam losses are carefully monitored all along the LHC. When the beam losses, and thus the energy deposition, exceeds pre-defined limits the beam dumping system is triggered to extract the beams in a controlled manner within 270 µs.

During the LHC operation losses were observed that occur in time scales below the reaction time of the beam dumping system. In order to protect the LHC from these losses the loss amplitudes have to be reduced. Therefore, it is important to understand the loss mechanisms causing these ultra fast losses. The time structure of these ultra fast beam losses cannot be resolved by the regular beam loss monitoring system. In the scope of this thesis diamond based beam loss monitors (dBLMs) were installed at the LHC, which provide nanosecond resolution and cover a wide range of loss amplitudes. These detectors were used to perform high resolution measurements of the ultra fast beam losses in order to identify the underlying loss mechanisms.

The results presented in this thesis include characterisation experiments of the installed dBLMs and the analysis of several scenarios of ultra fast beam losses during the LHC operation. The losses during beam injection, which were limiting the LHC operation in 2015 and 2016, will be discussed in great detail. Mitigation techniques based on this analysis were implemented in the LHC operation and allowed to reduce the injection losses by one order of magnitude.

Dies ist die Summe aller kleinen Schritte.

Contents

1 Introduction

This thesis presents the measurements and the analysis of ultra fast beam losses at the Large Hadron Collider (LHC) and their implications for machine protection. Diamond based particle detectors were used to measure these losses with nanosecond time resolution. This allowed to develop mitigation techniques, which were successfully implemented in the standard accelerator operation.

The principal task of high energy particle physics is to get a better understanding of the Standard Model of particle physics and to explore the physics beyond this theory. At the LHC, the world's most powerful accelerator/storage ring, scientists observe the interaction of particles by colliding them in the centre of four large detectors ALICE, ATLAS, CMS and LHCb. According to Einstein's formula of mass and energy equivalency, particles can be created during these interaction events depending on the centre of mass energy and the underlying physics. The characteristics of these often very short living particles and their decay products are measured with the aforementioned detectors and then compared to theoretical predictions. For these experiments high intense particle beams at highest energies are required to produce heavy particles at significant rates. As a consequence, when the LHC is completely filled with a total beam intensity of 3.2×10^{14} particles at maximum energy of $7 \, \text{TeV}$, $362 \, \text{MJ}$ are stored in each beam[1]. Uncontrolled losses of fractions of the beams at these energies can cause severe damage in the accelerator components [1]. For safe accelerator operation the LHC needs highly reliable and fast reacting systems protecting the accelerator from risks during operation. The LHC is therefore equipped with many diagnostic tools for identifying potential risks and systems to protect the accelerator from these dangers, which include failures of the accelerator hardware, beam instabilities and operational mistakes. One of the most important diagnostic tools that provides information on the beam conditions at the LHC is the beam loss monitoring system. As part of this system, about 3600 beam loss monitors are installed along the LHC. If the beam loss monitors detect losses, which exceed a certain threshold a beam abort is triggered, called a dump. The beam dumping system is capable of extracting the beam from the LHC within $270 \, \mu\text{s}$. Losses with durations below the reaction time of the beam dumping system are are referred to as ultra fast losses. The main source for ultra fast losses are failures in the fast injection and extraction systems, where fast gated kicker magnets are use to inject or extract the beam. Particles passing the kicker magnets during the rise time of the magnetic fields are mis-steered and lost downstream of the kicker systems. Dedicated absorber blocks are installed in the LHC in order to protect the accelerator from these losses. With the increased beam energy of $6.5 \, \text{TeV}$ and the bunch spacing of $25 \, \text{ns}$ after the long shut down the intensities of the ultra fast

---

[1] These are the design parameters. In 2016 the LHC reached beam energies of $6.5 \, \text{TeV}$ and 2.55×10^{14} protons resulting in a stored beam energy of $265 \, \text{MJ}$.

injection losses increased accordingly. During the injection process the losses were constantly close to the loss limits and sometimes caused beam dumps. In order to reduce these ultra fast losses the loss signatures were studied by recording the signals with diamond based beam loss monitors, which provide nanosecond resolution. Based on these measurements mitigation techniques were developed, which allowed the injecetion losses to be reduced by a factor 10.

Outline

An overview of the LHC and its key parameters is given in chapter 2. The basic principles of accelerator physics will be briefly introduced.

In chapter 3 the challenges for protecting the LHC from potential dangerous situations during operation will be introduced with a focus on beam losses. In this chapter different scenarios for beam losses are briefly discussed. These loss scenarios are then categorised by their loss duration before the losses reach levels, which trigger a beam abort. The beam losses are distinguished into slow, fast, very fast and ultra fast losses. The focus of this thesis is on the ultra fast losses, i.e. shorter than 270 µs. The need for a very fast beam loss monitor system for measuring the ultra fast beam losses is motivated.

In chapter 4 the principles of beam loss detection and the layout of ionisation chamber beam loss monitors are discussed with focus on the fast responding solid state ionisation chamber detectors, the diamond based beam loss monitors. Two types, single and polycrystalline diamond based beam loss monitors are introduced and their advantages over the standard LHC ionisation chamber beam loss monitor are pointed out.

The characterisation experiments for measuring the response function of LHC type diamond based beam loss monitors are presented in chapter 5. The beam test facility and the measurement setup are described. The results of the response function measurement and the derived charge collection efficiencies of the tested detectors are discussed.

At the LHC ten diamond based beam loss monitors are installed. In chapter 6 the layout of the detector setups, the frontend electronics and the data acquisition systems of the installed detectors are described. An overview of the detector applications is given and their locations are briefly introduced.

The studies of the injection loss measurements are presented in chapter 7. The identified loss mechanisms are discussed in detail. Based on the knowledge of the loss mechanics, techniques for mitigating the injection losses were developed. The different techniques and the results of dedicated tests are presented in chapter 7.5. In

addition the advantages of measuring the injection losses continuously with nanosecond resolution for identifying injection failures are discussed.

In chapter 8 further applications of the diamond based beam loss monitors at the LHC are presented. The optimisation of the detector setup in extraction region for recording the beam losses during an asynchronous beam dump event[2] without losing information due to saturation effects are discussed in chapter 8.1.
The first measurements with an experimental setup using diamond based beam loss monitors for measuring the particle population in the abort gap[2] are presented in chapter 8.2. Further optimisation steps are discussed.
Loss signatures of UFO-events (unknown falling objects) recorded with the recommissioned diamond based beam loss monitor setup after the long shut down 1 are briefly introduced in chapter 8.3.

In chapter 9 the characteristics of diamond based beam loss monitors for detecting ultra fast beam losses are discussed and underlined with examples from this thesis.

The final conclusion and a reflection of the main results of the presented work are given in chapter 10.

---

[2] In order to avoid the losses due to mis-steered particles during the rise time of the extraction kicker magnets, the kicker magnets are synchronised to an ideally particle free gap in the circulating beam, the abort gap. During an asynchronous beam dump the extraction kickers are not synchronised to the abort gap, which leads to losses with very high amplitudes in the extraction regions.

---

2 Overview of the Large Hadron Collider

The LHC is a circular accelerator with a circumference of 26.7 km. The accelerator has eight straight insertion regions (IRs), which are connected by the arc sections. In the middle of four of the insertion regions the four large experiments ATLAS, ALICE, CMS and LHCb are installed. In the other four insertion regions accelerator systems for controlling the beams are inserted, see Fig. 1. The two stored particle beams are collided in the centre of the four experiments to produce particle interactions.
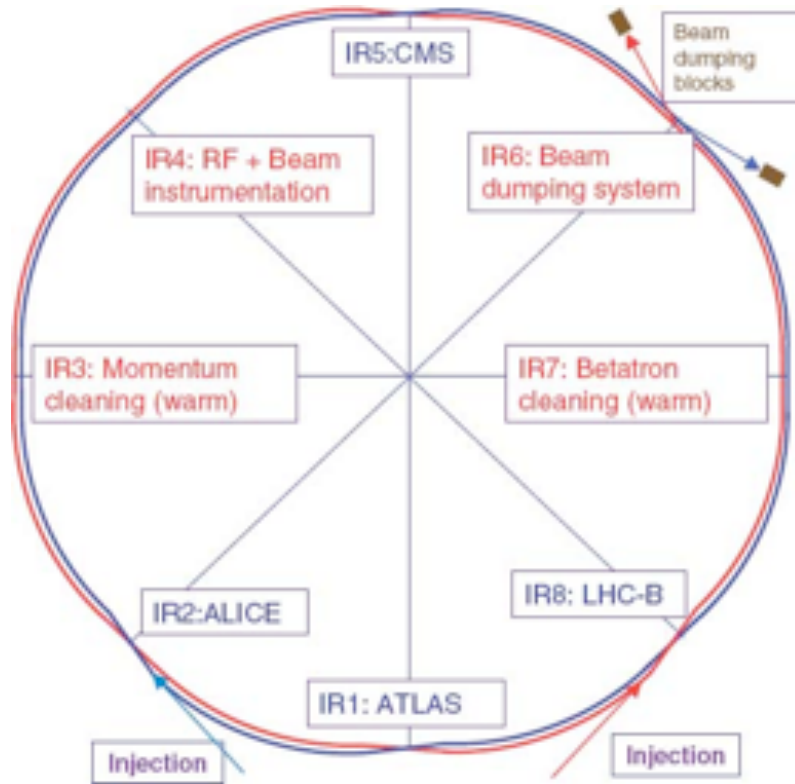
Figure 1: Schematic layout of the LHC [2]. The insertion regions (IRs) are interconnected by the arc sections. In four of the IRs the four large experiments, ATLAS, ALICE, CMS, and LHCb, are installed. In addition the IRs house accelerator equipment for controlling the beams. The beams are injected in IR 2 and IR 8. The main collimation systems are installed in IR 3 and IR 7. IR 4 houses the RF-cavities for accelerating the beams. The beam dumping systems in IR 6 extracts the beam at the end of a fill.

Table 1: LHC design parameters for proton-proton operation. Values for 2016 only displayed if they differ from the design parameters [3], [4], [5]

Parameter		Design	2016
Beam energy			
Injection	GeV	450	
Extraction	GeV	7000	**6500**
Circumference	m	26658.883	
Revolution frequency	kHz	11.245	
Revolution period	µs	88.925	
RF frequency	MHz	400.8	
Beta func. in IP1/IP5 (β^*)	m	0.55	**0.4**
Harmonic number		35640	
Max. number of bunches		2808	**2220**
Bunch spacing	ns	25	
Nom. bunch intensity	protons	1.15×10^{11}	
Norm. transverse emittance	µmrad	3.75	**2.8**
Peak luminosity IP 1/IP 5	cm^{-2}s^{-1}	1×10^{-34}	$\mathbf{1.5 \times 10^{-34}}$
Num. of main dipoles		1232	
Bending radius	m	2803.95	
Nom. dipole field	T	8.33	**7.74**
Num. of main quadrupoles		392	

The count rate of a specific event depends on the event's cross section σ_p and the luminosity $\mathcal{L}$, which describes the number of particle collisions per time in the interaction point.

$$\frac{dN}{dt} = \sigma_p \mathcal{L} \tag{1}$$

The luminosity of a collider depends on the transverse beam size σ_x, σ_y of the colliding beams, the number of particles and the revolution frequency.

$$\mathcal{L} \approx f \frac{n N_1 N_2}{\sigma_x \sigma_y} h \tag{2}$$

In Eq. (2) the total number of particles is given by the intensity of the bunches N_1 and N_2 times the number of colliding bunches n. The luminosity is corrected by the geometric factor h, which takes the crossing angle of the colliding beams
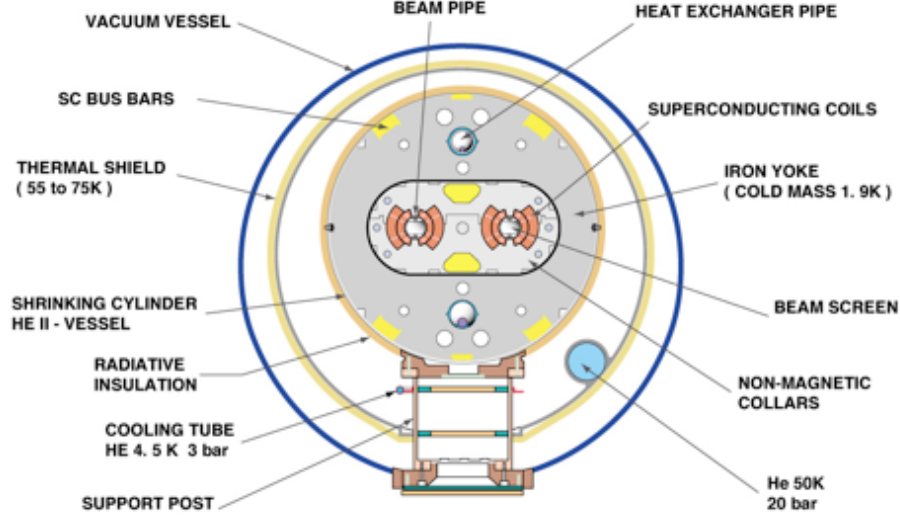
Figure 2: Schematic cross section of a LHC dipole. The geometry of the super conducting coils along the beam pipe define the magnetic field. The magnet is housed in a cryostat in order to allow an efficient cooling of the coils [7].

into account[3]. Assuming gaussian beams the beam sizes are usually expressed in the RMS-value of the distribution. In order to achieve a high event rate the luminosity needs to be as high as possible. As a consequence, many bunches with a high particle density are required. In the LHC for proton-proton operation the maximum number of bunches is 2808 with a nominal intensity of 1.15×10^{11} protons per bunch. With its design parameters, which are listed in Tab. 1 a nominal luminosity of $1 \times 10^{34}\,cm^{-2}s^{-1}$ can be obtained[4]. In order to investigate the production process of heavy particles, proton collisions at highest centre of mass energies are required. The bending radius of the existing tunnel allows beam energies of $7\,\mathrm{TeV}$ by using superconducting Nb-Ti dipole magnets with a nominal dipole field of $8.33\,\mathrm{T}$. The maximum achievable centre of mass energy is therefore $14\,\mathrm{TeV}$ [3]. The dipole magnets are installed in the arcs of the LHC. In Fig. 2 the schematic cross section of a LHC superconducting dipole is shown. In the centre the two beam pipes are visible. The arrangement of the superconducting cables around the beam pipe is optimised for creating the dipole field. The magnet coils are cooled with superfluid helium down to $1.9\,\mathrm{K}$.

---

[3] At the CMS and ATLAS the crossing angle is about $285\,\mathrm{\mu rad}$. The bunches do not collide head on resulting in a geometric factor smaller than one [6].

[4] With optimised accelerator settings and smaller beam size in the collision points a even higher luminosity of $1.5 \times 10^{34}\,cm^{-2}s^{-1}$ was achieved in 2016 [5].
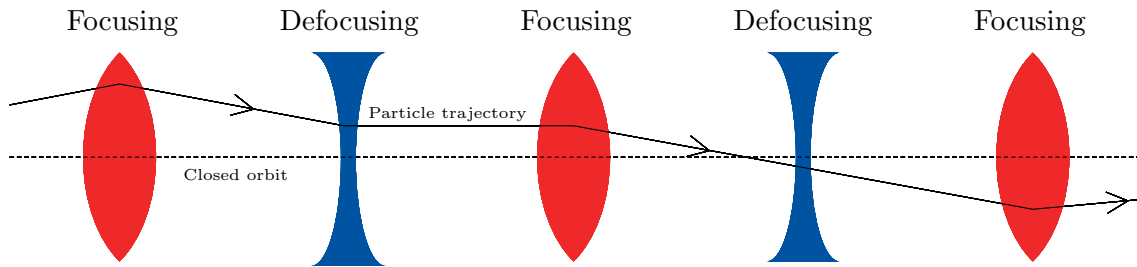
Figure 3: By inserting quadrupole magnets the particles are focused towards the closed orbit. Quadrupoles focus in one plane while they defocus in the other plane. With a sequence of focusing and defocusing quadrupoles an overall focusing effect can achieved. The particles oscillate around the closed orbit along their path around the LHC.

For long-term storage of the particles in the collider the divergent beams need to be re-focused. For the LHC's strong focusing magnet lattice[5] superconducting quadrupoles with alternating field gradients are inserted regularly into the sequence of the bending magnets [8]. While a quadrupole focuses the particles in one plane, e.g. the horizontal plane, it defocuses it in the other plane. An overall focusing is achieved by choosing the right sequence of quadrupoles and the correct field strengths[6]. On their trajectory around the LHC the particles oscillate around the closed orbit, see Fig. 3. Superconducting magnets are very sensitive towards energy deposition, which can lead to quenches, resulting in a beam dump.

While magnetic fields are used for bending and focusing the circulating particles, electric fields are used for particle acceleration. In order to realise a turn-by-turn acceleration high frequent alternating fields are needed. These fields are generated by electromagnetic waves resonating in cavities. These oscillations are driven by supplying these cavities with radio frequency power (RF). Due to the alternating field vector the beam needs to be sequenced into bunches which are synchronised to the accelerating electric fields. In order to allow multiple bunches in the accelerator the RF is operated at multiples of the revolution frequency. The LHC revolution frequency is 11.245 kHz and the harmonic number is 35640, resulting in a RF-frequency of 400.8 MHz.

Since the orbit length depends on the particle's energy, particles with a higher energy have a longer orbit and thus a lower revolution frequency. Particles with lower

---

[5] The lattice describes the sequence accelerator components along the beam pipe, e.g. the bending and focusing magnets.

[6] The particle transport along the accelerator can be described by transforming the initial particle state by applying a lattice specific transport matrix. The linear approximated particle trajectories are stable if the trace of the transport matrix, the Twiss matrix M,
is smaller than two ($|TrM| \leq 2$) [9].
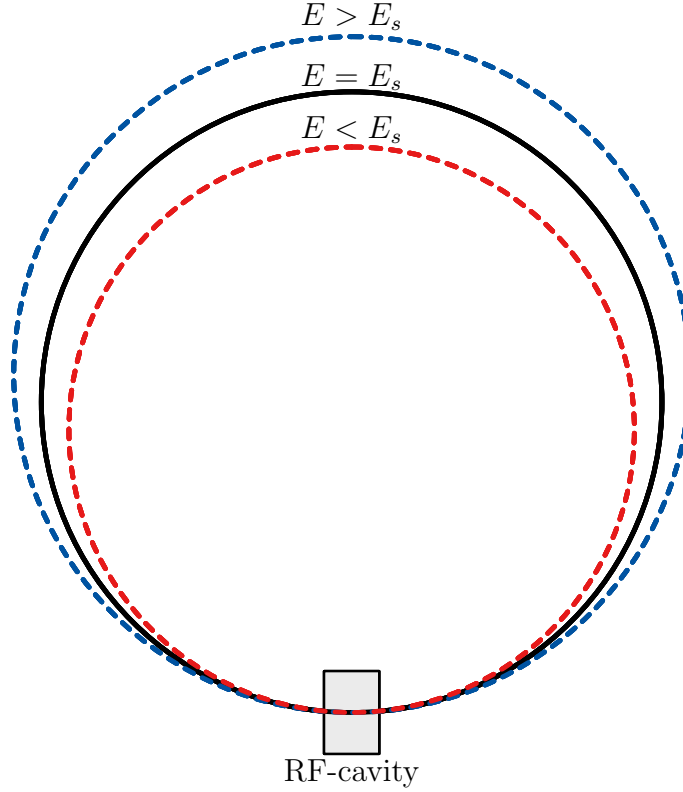
Figure 4: For relativistic particles the orbit length depends on the particle energy. Particles with a lower energy than the synchronous particle s have a shorter orbit, which results in a higher revolution frequency, red. Particles with a higher energy have a longer orbit and, thus, a lower revolution frequency, blue.

energy have a higher revolution frequency, see Fig. 4. In a stored beam the synchronous particle of a bunch is synchronised to the zero point of the RF-wave and therefore does not gain energy, see Fig. 5. Particles with low energy arrive earlier than the synchronous particle in the cavity, i.e. their orbit is shorter. The particle is accelerated by the positive amplitude of the accelerating field. With the additional energy the particle's orbit increases and so the revolution frequency decreases. For the next turn the particle will arrive later. The negative amplitude of the electric field decreases the particle energy, which results in a higher revolution frequency for the next turn. This cause the particles to oscillate around the synchronous particles. This phase-focusing preserves the bunch structure of the circulating beam. In Fig. 6 the $\Delta E\,\phi$ phase space with the synchronous particle in the middle is displayed. The particles move on stable elliptic trajectories around the synchronous particles if the energy and the phase deviation are small. The stable trajectories are called the RF-bucket. However, if the energy and phase deviation is too large the particles are

not captured. They slip along the bucket structure and are referred to as coasting beam [10]. The stable trajectories and the un-stable trajectories are distinguished by the separatrix. It's area defines the RF-bucket's acceptance. The acceptance can be modified by changing the RF-parameters, e.g. the amplitude of the voltage.

Coasting beam can be created during the injection of the beam due mismatches between the transfer line optics and the optics of the accelerator. Multiple effects like Touschek scattering, intra beam scattering, non linear motions due to long range beam-beam collisions at top energy and Coulomb scattering of the circulating particles with the rest gas can cause the particles to diffuse out of the stable RF-buckets onto trajectories outside the separatrix. The result is a continuous particle distribution around the accelerator. The coasting particles lose energy due to synchrotron radiation until they exceed the accelerator's energy acceptance and are hence lost. The energy loss due to synchrotron radiation depends on the particle's energy, which leads to different life times of the coasting particles. For the LHC the life time of a scattered proton at injection energy of $450\,\mathrm{GeV}$ has a life time of about 390 hours and 6.5 minutes at an energy of $7\,\mathrm{TeV}$ respectively [11].

To accelerate the particles the dipole fields are slowly ramped up. The increased magnetic field causes a smaller bending radius, resulting in a shorter orbit length. The synchronous particle arrives in the cavity when the electric field still has a positive amplitude and therefore the particles gain energy every turn, see Fig. 7. Coasting particles outside the separatrix are lost during the acceleration process. The RF-cavities are installed in IR 4 of the LHC, see Fig. 1.
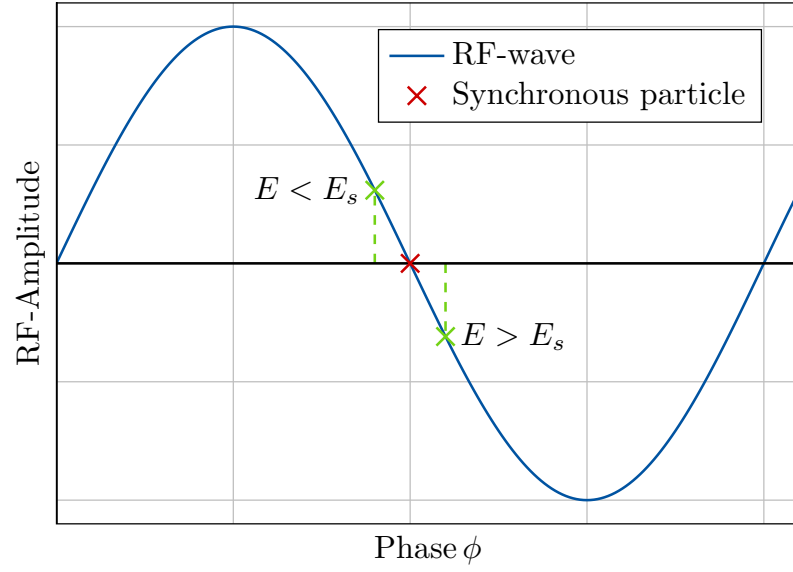
Figure 5: Phase of the synchronous particle with out acceleration. The synchrotron motion of the off-momentum particles keep the beam bunched.
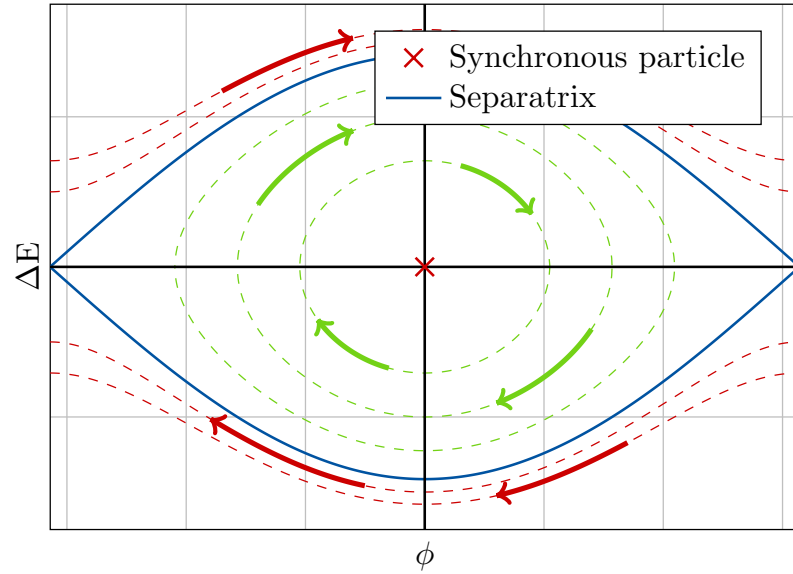
Figure 6: $\Delta E \phi$-phase space of a stored bunch with the synchronous particle in the middle, no energy gain, see Fig. 5. The particle inside the bucket, green, move on ellipses around the synchronous particle, green arrows. The beam stays bunched within the RF-buckets. Particles outside the bucket coasts along the RF-structure. Stable and unstable trajectories are separated by the separatrix.
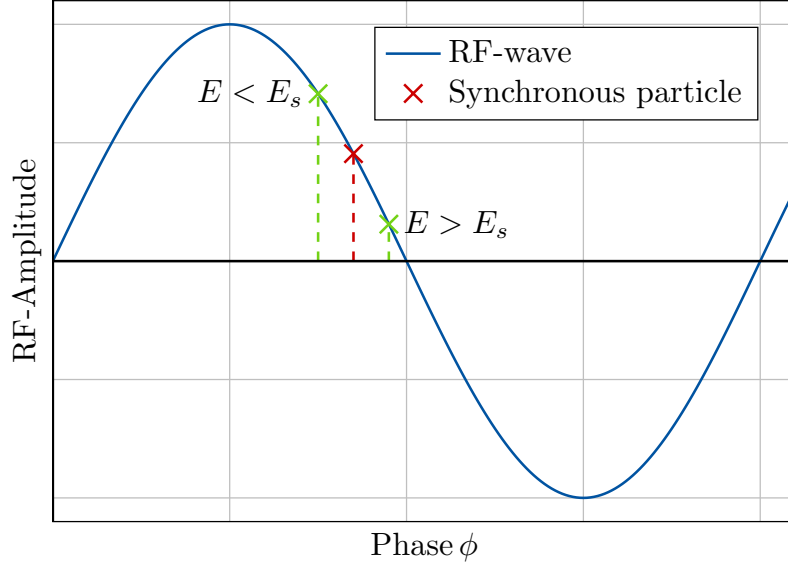
Figure 7: Period of the RF-wave. During the energy ramp the synchronised particle passes the cavities while RF-wave has a positive amplitude so it gains energy at every turn.
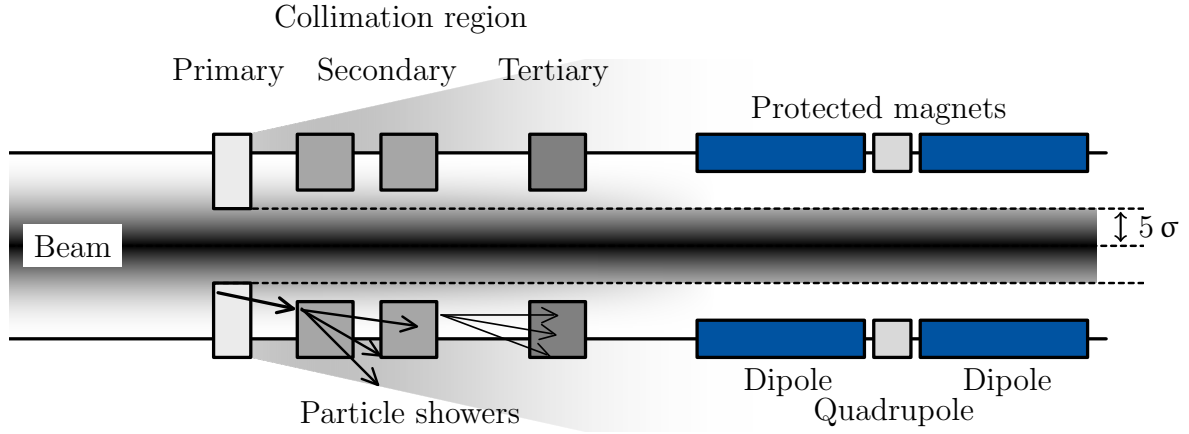
Figure 8: Schematic representation of the multi-staged beam collimation in the LHC. The primary collimators form the aperture bottleneck, so that they intercept the particles. Downstream of the primary collimators the secondary and tertiary collimators are installed in order to attenuate and to absorb the secondary showers created by the particles impacting on the collimators. Downstream accelerator components with a larger aperture are in the shadow of the collimators.

In order to protect the accelerator components from beam losses and to localise the losses in supervised areas dedicated absorbers, i.e. collimators, are installed in the LHC. Particles with a too large energy offset will be lost on the collimators in IR 3. Particles deviating too far from the design orbit are lost on the collimators in IR 7. The primary collimators in IR 7 form with an opening of $5\,\sigma$ from the beam axis the aperture bottleneck. The downstream secondary and tertiary collimators attenuate and absorb the secondary particle showers resulting from the impinging particles on the primary collimators. The movable jaws of a primary collimator are made of carbon composite materials so that they can withstand the impact of high energetic particles. By positioning the collimators close to the beam, the outer particles of the beam, the halo, are intercepted. For an effective beam cleaning a multistage collimation system and multiple passes of the particles are necessary. All other accelerator elements are in the shadow of these absorber blocks. Additional collimators and absorber blocks are installed upstream and downstream of the experiments to protect the accelerator components from collision debris. In the injection and extraction regions collimators absorb the injection and extraction losses [3].
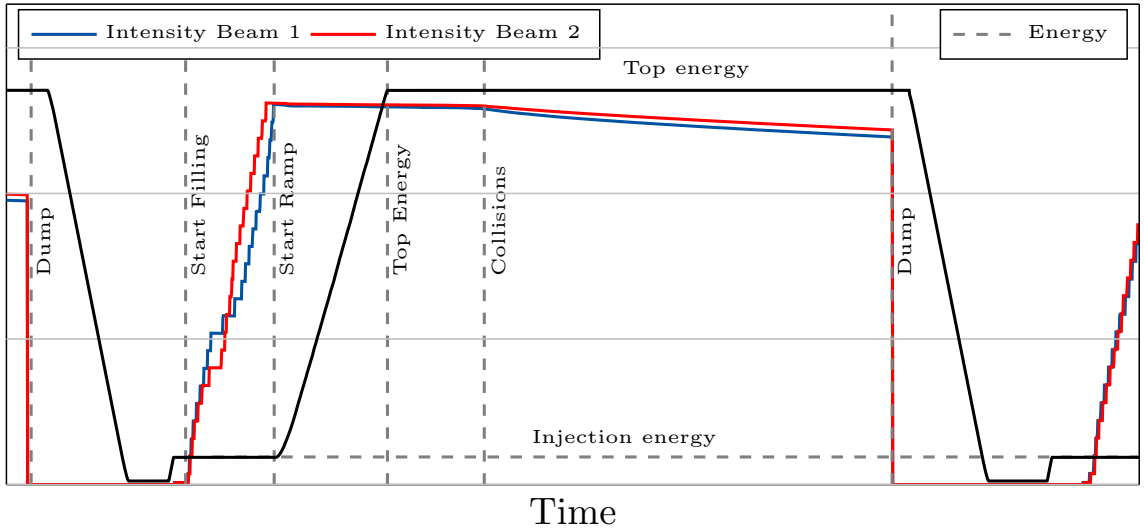
Figure 9: Cycle of the LHC operation. After a fill the beams are dumped and the magnets are ramped down to injection energy. For filling both beams, multiple bunch trains are injected into the LHC. The particles are accelerated to top energy during the ramp. After the preparation of the accelerator for collision production both beams are collided in the centre of the experiments. During the collision production the intensity of the beams decreases. When the beam intensities are too low the beams are dumped and the accelerator is prepared for the next fill.

The LHC operation is divided into fills. In the beginning of a fill the magnets are at the injection plateau[7]. During this time the accelerator is filled by injecting multiple bunch trains, which were prepared by the pre-accelerator complex. The desired number of bunch crossings in the experiments is optained by injecting the bunch trains into specific positions of the LHC beams. The sequence of the circulating bunch trains is the filling pattern. The injection energy in the LHC is $450\,\mathrm{GeV}$. The injection system for beam 1, the clockwise circulating beam, is installed in IR 2. The anticlockwise circulating beam, beam 2, is injected in IR 8. The beam preparation will be discussed in chapter 7. After the LHC has been filled, the beams are accelerated to top energy. At the end of the acceleration the LHC is prepared for particle collisions, e.g. the beam is focused to the centre of the experiments. As a last step the beams are brought into collisions and the experiments can start recording data. During the collision process the beams' particle intensity decreases due to the luminosity burn-off. At a certain point the intensity and hence the luminosity is decreased so far that a refill of the machine is more efficient than continuing with the low intensity beams. At the end of a fill the beam dumping system extracts the beams from the LHC and directs them into the dump lines. At the end of these beam lines, carbon dump blocks are installed, which absorb the beam safely. After the dump the magnets ramped down to the injection plateau. The turn around time, i.e. the time from stable beams to stable beams is in the range of two to three hours [3]. The LHC cycle with the different steps is shown in Fig. 9. If the beams are dumped due to errors during the accelerator operation, e.g. failures of accelerator components, the turn around time can be much longer. In 2015 the average turn around for LHC operation with $25\,\mathrm{ns}$ bunch spacing was $6.8\,\mathrm{h}$ [12] and in $7.1\,\mathrm{h}$ in 2016. The shortest achieved turnaround time in 2016 was $2.5\,\mathrm{hours}$, which is close to the minimum turnaround time of about $2.2\,\mathrm{h}$[8] [13].

[7] The minimum accepted beam energy is $450\,\mathrm{GeV}$ corresponding to $0.535\,\mathrm{T}$ in the LHC dipole magnets.

[8] This time is valid for the LHC turnaround process in 2016.

3 Machine protection challenges at the LHC
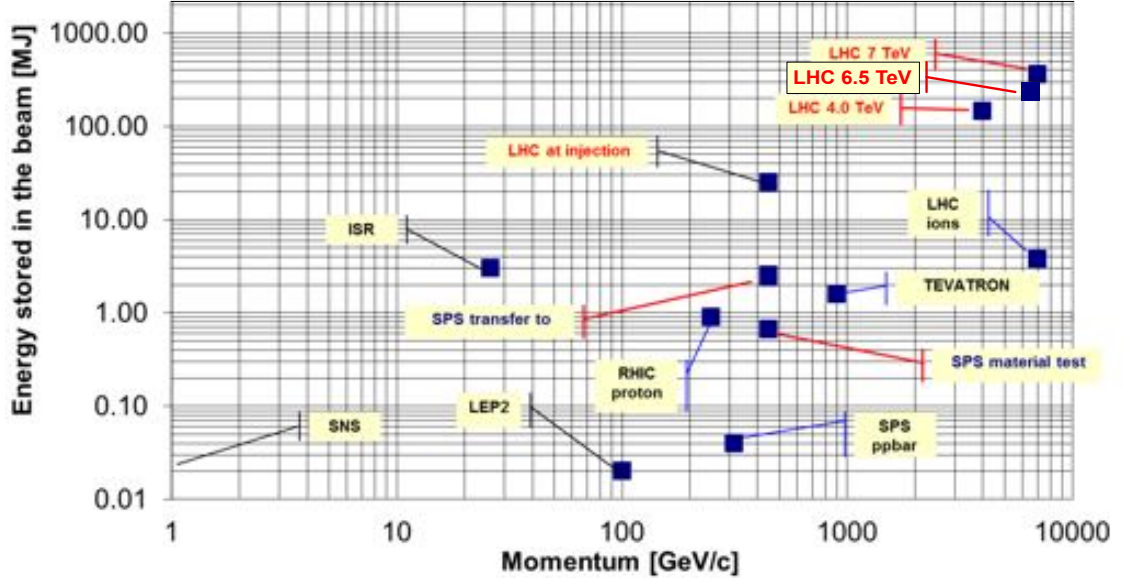
Figure 10: Stored beam energy in different particle accelerators over the momentum of the particles. For the LHC operation in 2015 and 2016 at 6.5 TeV 265 MJ were stored in each beam. With design parameters, 7 TeV and 2808 bunches 362 MJ will be stored.[14].

As introduced in chapter 1 the goal of the LHC is to provide high collision rates at highest energies as long as possible. Therefore it is of importance to minimise the unwanted downtime due to failures. In order to reduce the commissioning time of the superconducting magnets after the long shut down, from 2013 - 2015, it was decided to operate the LHC at 6.5 TeV beam energy instead of 7 TeV from 2015 onwards[9]. During the accelerator operations in 2015 and 2016 the maximum achieved number of bunches was 2220 bunches per beam, which resulted in a stored beam energy of 265 MJ in each of the two beams in the LHC. This has never been achieved in any particle accelerator before, see Fig. 10. The loss of 5×10^9 particles at 7 TeV exceeds the damage limits of the tertiary collimators, this intensity compares to less than 5% of a nominal bunch [16]. The shower particles, which resulted from particle losses can cause failures in the close-by electronics [17]. In addition, impacts of high energetic particles lead to unwanted activation of the materials. Before the damage limit of the components is reached, energy depositions in the superconducting magnets can lead to quenches. Therefore one of the prominent risks at the LHC are massive losses of

---

[9] The superconducting magnets need to be trained before they can reach the current densities, which are required for the high energetic beams. During the training phase the superconducting magnets are deliberately quenched, which allows them to reach higher currents afterwards. The number of training quenches increases with the current density [15].
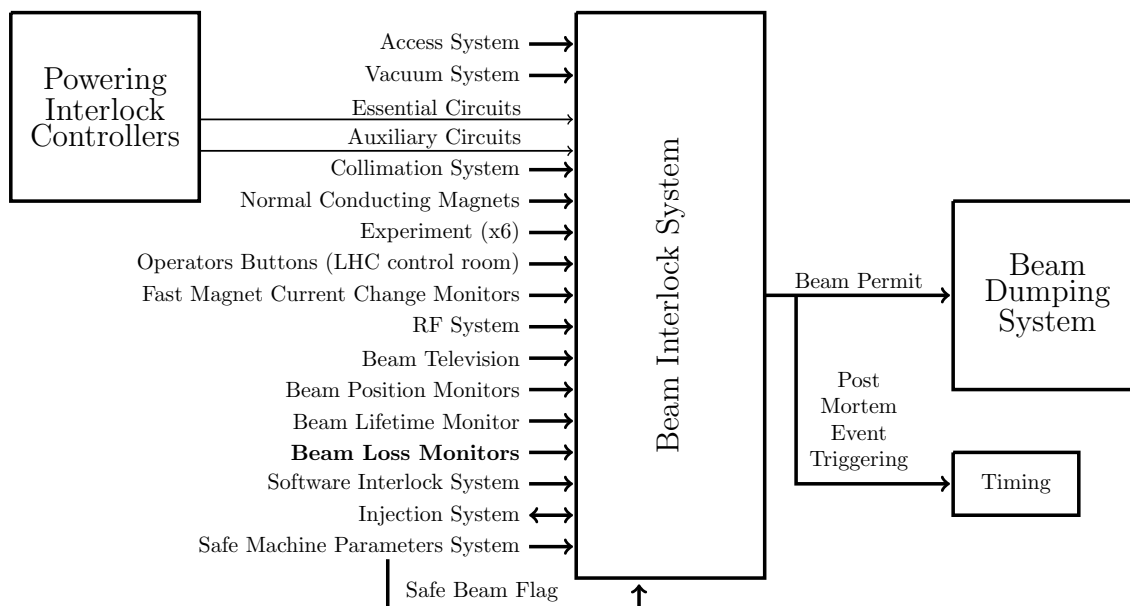
Figure 11: The beam interlock system gets input from various subsystems. If one of the subsystems raises an error the beam permit is cancelled and the beams are dumped [18].

the LHC beams induced by failures in the accelerator hardware or errors during the accelerator operation. Only if the accelerator parameters are within the pre-defined safe limits can beam operation be possible. Therefore input from many different systems are used for monitoring the status of the LHC. The beam interlock system is the backbone of beam related protection. It gets input from several subsystems, for example from the beam loss monitoring system, see Fig. 11. If the parameters of only one subsystem raises a failure the beam permit is cancelled and a beam dump is triggered. The time between failure registration, cancelling the beam permit, synchronisation of the kicker magnets to the abort gap and the actual beam dump is about 270 µs, which corresponds to about three turns of the LHC. The dumping procedure consists of three phases: losses exceeding the dump threshold and trigger the beam dump, synchronising the extraction kicker magnets to the abort gap and the actual beam extraction. Even if the abort gap is already synchronised and there is no delay due to the signal processing in the electronics, the minimum time for extracting the beam is one LHC turn, 89 µs, the time the complete beam needs to pass the extraction kicker magnets. In case of a beam dump, the data buffers of the accelerator systems and subsystems are stored which allow the recreation of the accelerator status seconds before the dump[10] for detailed analysis and the

---

[10]The status of the subsystems is monitored with different sampling rates ranging from MHz down to tenth of a hertz. In average 1000 samples are stored for fast sampling monitors and few tens samples are stored for low sampling systems [19].

Figure 12: Installed ionisation chamber beam loss monitors (icBLM), yellow cylinders, outside a superconducting quadrupole magnet cryostat. With about 3600 installed icBLMs the beam losses are closely monitored along the LHC.

identification of the cause for the dump [20]. Only if the cause for the dump was identified and the safe beam conditions are re-established, then the beam permit is granted again such that the accelerator operation can continue.

3.1 Monitoring the beam losses

Particles get lost when they leave their stable trajectories. Ideally, these particles are absorbed by the collimators. If not they impact in the beam pipe in the accelerator. By interacting with matter the high energetic particles create showers of secondary particles. The lost particle and the secondary showers particles deposit energy in the accelerator components leading to ionisation, thermal effects, activation or in case of electronics to single event effects. During the accelerator operation small amounts of particles are continuously lost due to diffusion effects, see chapter 2. The location and loss signature[11] give information about the conditions of the circulating beams in the LHC. In order to monitor the losses with a high granularity, the LHC is equipped with a beam loss monitoring system consisting of about 3600 ionisation beam loss monitors (icBLMs) and dedicated readout electronics [21],[22]. The icBLMs are installed all along the LHC close to the beam pipe or in the locations of superconducting magnets outside the cryostat, see Fig. 12. In the IRs the high density of icBLMs allows detailed measurements of the local losses.
The accelerator components in the LHC have different sensitivities to beam losses.

---

[11]In this thesis the the signal over time is referred to as loss signature.

While the collimators can cope with continuous energy deposition of 97 kW, the quench limit of the superconducting magnets are in the range of milli-watts [3], [23]. In order to protect the accelerator elements from too high beam losses, maximum loss limits were defined for the beam loss monitors. The beam loss monitoring system is connected to the beam interlock system, so if these limits are exceeded the beams are dumped. Therefore these limits are called dump thresholds. The threshold signal is calculated from the signal in the monitor created by one lost particle (Q) and the maximum allowed number of particles (N_p) of the protected device. The signal height created by a single particle depends on the accelerator geometry, i.g. the components, which shield the loss induced showers, and on the beam energy (E_{beam}). The maximum allowed number of lost particles strongly depends on the sensitivity of device, which is protected by the BLM. These limits were defined by Monte Carlo simulations and validated during accelerator operation. In order to cope with thermodynamic effects the maximum number of allowed particles depends on the loss length (Δt) as well. An extra safety margin is added by introducing the monitoring factor (MF). The final formula for calculating the threshold T is then [24],[25]:

$$T(E, \Delta t) = MF \times Q(E_{beam}) \times N_p(E, \Delta t) \tag{3}$$

The acceptable loss intensities depend on the duration of the losses. Therefore the beam loss monitoring system integrates the losses for different time intervals[12] in parallel. These intervals last from several tens of seconds down to 40 µs. Following the Nyquist-Shannon sampling theorem the temporal resolution limit of the beam loss monitoring system for the 40 µs integration interval is 80 µs [26].

---

[12]The LHC beam loss running sums range from 83.9 s down to 40 µs. Thresholds for every location, running sum and beam energy are defined.

3.2 Categorisation of beam losses in terms of the loss duration

At the LHC beam loss events differ strongly in their duration and intensity. There are various mechanisms and failures, which lead to an increase of the beam losses. These loss scenarios can be categorised by their duration from the start time of the losses until the losses reach critical levels if no countermeasures are applied. The scenarios are distinguished into the following four categories:

Slow

- Time range: $\geq 1\,\text{s}$

Long loss events are related to abnormal conditions of the LHC and failures, which evolve over seconds, e.g. orbit and tune[13] drifts. These drifts can result from failures in the feedback systems which correct the orbit and tunes during the acceleration phase [27]. If not corrected the drifts will cause beam losses triggering a beam dump eventually.

Fast

- Time range: $\geq 15\,\text{ms}$

Fast failures can cause potentially dangerous losses in time scales down to 15 milliseconds. In case of a quench the quench protection system opens diodes to divert the current into a normal conducting bypass in order to protect the magnet from damages due to resistive heating. The change of the magnetic fields will lead to orbit perturbation resulting in beam losses. Therefore whenever a quench is detected the beams are dumped [15]. Trips of the accelerating cavities lead to debunching of the beams resulting in high coasting beam intensities. In order to avoid a high abort gap population, due to the coasting beams, the beams are immediately dumped. At top energy the energy losses due to synchrotron radiation of the coasting beam causes an orbit drift, which leads to high losses [28].

---

[13]The tune is the number of oscillations the particles perform in the transverse plane around the closed orbit on their trajectory around the accelerator. In order to avoid resonant excitation of the beam due to magnetic field imperfection the non-integer part of the tune has to be a non-fractional irrational number.

Very fast

- Time range: $\geq 270\,\mu s$

Very fast failures result within a few turns of the LHC into massive beam losses. Equipment related scenarios in this category are failures in the normal conducting magnet power supplies. Due to the high radiation fields resulting from the collision debris of the particle interactions the separation magnets upstream and downstream of the experiments can not be superconducting. These magnets are normal conducting with a relatively high resistivity of about $850\,m\Omega$ compared to superconducting magnets. In case of failures in the magnets' power converters, the field decay time[14] is approximately 2 s. In combination with the large amplitude of betatron function [15], of about 2000 m, field changes results in large orbit perturbations [29]. Beside the hardware failures there are beam related scenarios reaching in very short times high loss amplitudes. Free electrons in the beam pipe can be accelerated in the field of the circulating particles. When these electrons hit the beam screen secondary electrons can be created, which then experience the accelerating field of the circulating beam and the process repeats itself. The resulting electron cloud can cause instabilities in the beam. The time to built up the electron cloud is in the order ten to several hundred turns [30].

Another prominent example for very fast beam losses are micro particles falling into the beam. These events are know as UFOs, unknown falling objects. The circulating beam scatters on these falling particle resulting into massive localised beam losses. These losses are so fast that they are close the reaction limit of the LHC beam dumping system. In some cases the losses due to the falling particles exceeded the quench limit before the beams were dumped [31], [32].

Ultra fast losses

- Time range: $< 270\,\mu s$ (Three turns of the LHC)

The losses with durations below the reaction time of the LHC protection systems are classified as ultra fast losses. One major source for ultra fast beam losses are failures in the injection and extraction systems. Fast rising kicker magnets with rise times between $0.9\,\mu s$ and $2.8\,\mu s$ are used for steering the incoming beam into the LHC and for extracting the beam in case of a beam dump. If these systems are falsely triggered, the deflection of the circulating beam causes massive beam

---

[14]The decay time τ depends on the inductance H and the inner resistivity R of the magnet, $\tau = H/R$. In case of the LHC normal conducting separation magnets: $R = 850\,m\Omega$ and $H = 1740\,mH$

[15]The betatron function describes the focusing and defocusing effects of the accelerator lattice on the particle trajectory.

losses. Synchronisation errors between the particles and the phase of the kicker magnet[16] can lead to high beam losses. The losses due to mis-steered beam can reach potentially dangerous levels within few microseconds long before the beam dumping system can extract the beams. Since the LHC can not be actively protected by the beam dumping system the accelerator is equipped with absorber block and collimators downstream of the injection and extraction systems. Even without an actual failure continuously high amplitudes of ultra fast beam losses during the beam injection process were observed, which sometimes exceeded the loss thresholds. The measurements and analysis of these losses are presented and discussed in chapter 7. Another source for ultra fast beam losses are failures in the crab cavity system[17], which is part of the LHC upgrade for the High Luminosity LHC. A cavity quench or electron multipacting[18] will result in a phase or voltage change leading to mis-steering of the bunches within time scales of $100\,\mu s$ [32].

3.2.1 Amplitudes of ultra fast injection losses at the LHC before and after the long shut down

In case of beam losses the reaction time of the LHC machine protection systems, including beam loss monitoring system, is short enough to extract the circulating beams from the accelerator so that the LHC is protected from slow, fast and very fast losses. The ultra fast injection and extraction losses were anticipated, therefore passive absorber blocks were installed in the injection and extraction region. The loss amplitudes of ultra fast beam losses during the LHC operation in Run 1[19] before the long shut down were low enough so the operation of the LHC was not influenced. After the long shut down the injection kicker waveforms were changed to a flat top length of about $5.1\,\mu s$ and the bunch spacing was reduced to 25 ns. The resulting increase of the injection losses lead to continuously high loss amplitudes reaching more than 95% of dump thresholds of the BLMs in the injection regions.

---

[16]The kicker magnets follow a specific wave form, kicker off, rising, flat-top, falling and off again. Particles which are not synchronised to the correct phase are mis-steered and lost downstream of the kickers.

[17]For the High Luminosity LHC the crossing angle of the beams in the experiments will be increased in order to reduce long range beam beam effects. The resulting luminosity reduction will be compensated by chirping the transverse momentum of the bunches longitudinally in the horizontal or vertical plane by applying a time-varying transverse kick to the bunches such that the bunches completely overlap at the interaction point [33], [34].

[18]Multipacting is the repeated effect of multiplying electrons, which are accelerated in the cavity and are then impacting in the cavity walls creating further electrons due to secondary emission. The resulting avalanche effect drains power from the cavity.

[19]Run 1 is the LHC operation period before the long shutdown, March 2010 until February 2013. During this period the LHC was operated with 7 TeV centre of mass energy, which was increased to 8 TeV from April 2012 on. The nominal bunch spacing was 50 ns.

Occasional dumps due to exceeded thresholds during the injection even limited the LHC availability.

3.3 Advantages of fast responding beam loss monitors with nanosecond time resolution

In this thesis the focus is on measuring and reducing the loss intensities of ultra fast beam losses, which results in a reduction of beam dumps. Reducing the number of dumps due to ultra fast beam losses by just increasing the dump thresholds is not favourable. Even if the losses do not induce damage immediately, the constant exposure to the high energetic particle showers causes an accelerated ageing effect due to the accumulated ionising dose and activation of the accelerator components. The mixed field radiation can cause single event effects which compromises the performance of the exposed electronics.

In order to mitigate the intensities of the beam losses the loss mechanisms have to be identified. Diamond based beam loss monitors (dBLMs) provide a double peak resolution of $5.6\,\text{ns}$[20]. In addition they cover an intensity range of 10^2 up to 10^7 particles within $10\,\text{ns}$ dynamic range, which allows the measure of losses with very different amplitudes. Paired with an adequate data acquisition system the diamond based beam loss monitors are an excellent tool for measuring the ultra fast beam losses with a high temporal resolution. In chapter 4.2 the diamond based beam loss monitor and its characteristics are described. In Fig. 13 and in Fig. 14 the injection loss signals of the same injection are displayed. The loss signature shown in Fig. 13 was recorded with an icBLM, with a sampling rate of 25kHz ($40\,\mu\text{s}$ integration time). The second plot depicts the injection loss signature recorded with a dBLM is depicted. Both detectors are installed in the LHC injection region at the same position[21]. From the dBLM data the actual loss signature can be resolved into two even shorter losses with different amplitudes. The trends and the timing of these two losses are typical for the injection losses, which give indications on the loss mechanisms. The length of the actual loss is about $12\,\mu\text{s}$, which was derived from the high resolution data. The yellow bar in Fig. 13 indicates the measurement interval displayed in Fig. 14.

The LHC beam loss monitoring system allows the measurement of the loss location due to the high granularity of the many installed icBLMs. The data from the diamond based beam loss monitors shows impressively the advantages of a loss detection system with high time resolution for measuring the loss structure of ultra fast beam losses.

---

[20]The double peak resolution is the minimal temporal separation of two maxima, which allows to identify the signals as two individual peaks.

[21]The distance between the detectors is less than $50\,\text{cm}$.
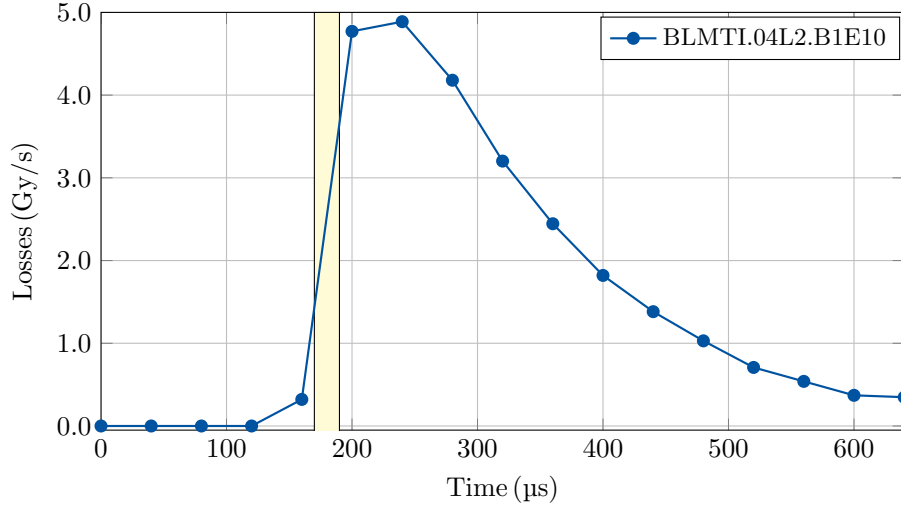
Figure 13: ultra fast injection loss signal recorded by the beam loss monitoring system with the shortest integration window length of 40 µs. The losses occur in the time window indicated with a yellow bar. The signal length is dominated by the response time of the beam loss monitor and the data acquisition system, long fall time after the initial short signal.
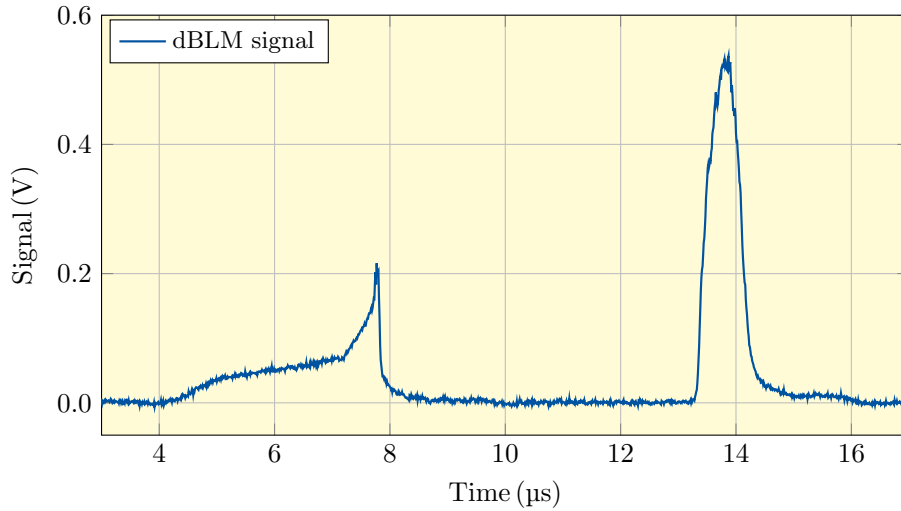
Figure 14: Diamond based beam loss monitor signal of the event which was displayed in Fig. 13. The sampling rate was 1 GHz. The displayed data show the injection loss structure. The displayed time corresponds to the yellow window indicated in Fig. 13.

23

4 Beam loss detection

In the beginning of this section the principle mechanisms of charge creation due to ionisation will be introduced. Based on the principle of a solid state ionisation chamber the diamond-based beam loss monitor (dBLM) and its characteristics will be described.

4.1 Ionisation due to impinging charged particles

High energetic charged particles interact with matter in various ways. The impinging charged particles in this case interact with the electron shell of the atoms. Due to these interactions the incoming particle loses energy while propagating through the material. The energy loss of hadrons and ions over a certain length (dE/dx) follows the Bethe formula

$$-\frac{dE}{dx} = \frac{n_e z^2 e^4}{4\pi\epsilon_0^2 m_e c^2 \beta^2} \left[\ln\left(\frac{2m_e c^2 \beta^2}{\langle E_b \rangle \left(1 - \beta^2\right)} \right) - \beta^2 \right] \tag{4}$$

with the parameters listed in Tab. 2. If the energy transfer from the impinging particle towards the atom exceeds the binding energy, the atom is ionised. In a gas ionisation creates free electrons and ions. In a solid state insulator/semi-conductor electron-hole pairs are created by exciting the electrons across the band gap.

Table 2: Parameters of the Bethe formula, Eq. (4)

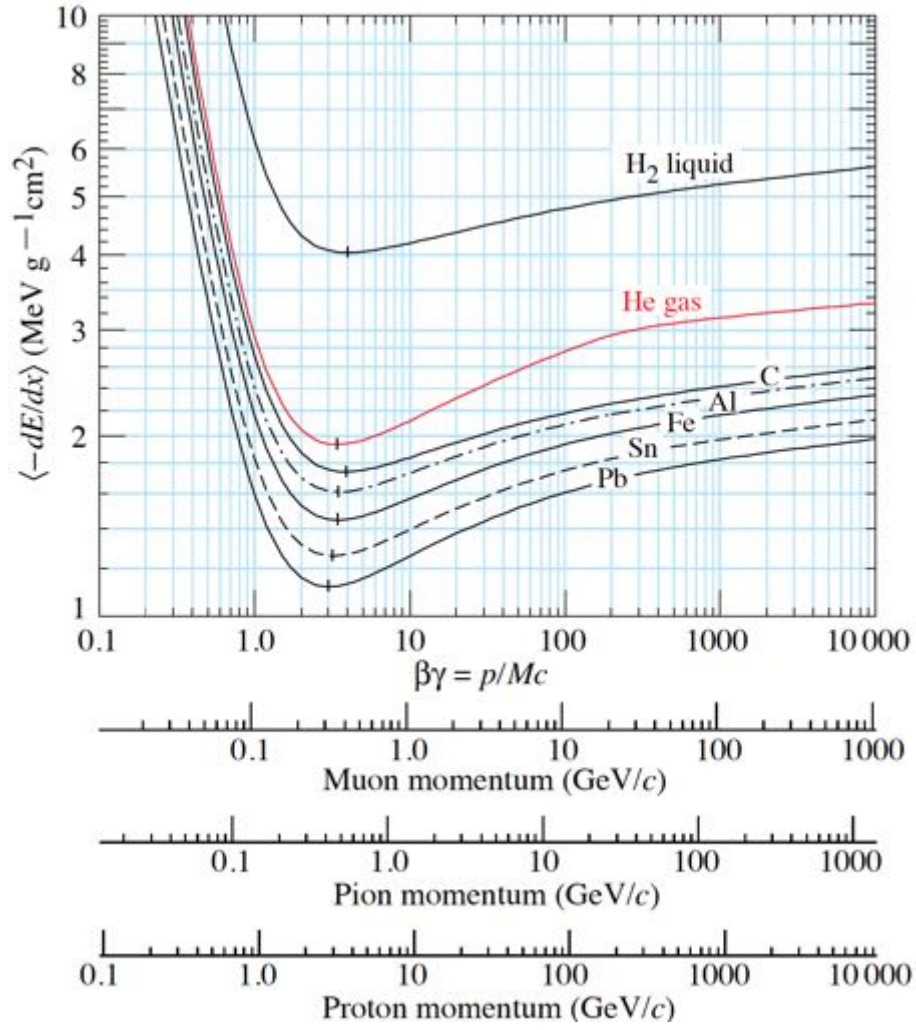| Parameter	
n_e	electron density
z	charge of the impacting particle
e	charge of an electron
e_0	vacuum permittivity
c	speed of light
$\beta = v/c$	relativistic β
$\langle E_b \rangle$	mean excitation energy

Figure 15: Energy loss per unit length over particle momentum for different impinging particles and materials [35].

The energy deposition in the material depends on the particle type and the particle energy. Figure 15 shows the energy loss of charged particles at medium energies impinging on different materials. The different functions fall with the increasing particle energy until the global minimum is reached. Particles with energies at the function's minimum are called minimum ionising particles (MIP). For protons impinging on diamond this energy is about $3.5\,\mathrm{GeV}$. From there the energy loss per unit length increases logarithmically. In the LHC the secondary particles in a loss induced particle shower have energies in the GeV regime. Since the energy loss grows only logarithmical with the particle's energy, the shower particles are treated as minimum ionising particles in this thesis. For higher particle energies, energy losses due to bremsstrahlung need to be taken into account, see Fig. 16. The energy loses due to radiation effects per path length (dE/dx) are described by;

$$\left(\frac{dE}{dx}\right)_{rad} = \frac{4 n_\alpha Z^2 \alpha^3 (\hbar c)^2 E_e}{m_e c^4} \cdot \ln \frac{a(E)}{Z^{1/3}} \tag{5}$$

with the relevant parameters listed in Tab. 3. The total energy loss is a superposition of losses due to ionisation and radiation losses. For electrons impinging on diamond radiative energy losses become dominant at particle energies above $100\,\mathrm{MeV}$, see Fig. 16. The minimum ionising particle energy of an electron impinging on a diamond crystal is about $2.3\,\mathrm{MeV}$.

Table 3: Parameters for Eq. (5) describing the energy loss due to radiation

Parameter	
E_e	kinetic energy of the impacting electron
n_a	atomic density of the material
Z	charge of the nuclei
α	fine structure constant
$a(E)$	numerical factor governing at which maximum impact parameter the electron is sufficiently scattered to produce radiative energy losses
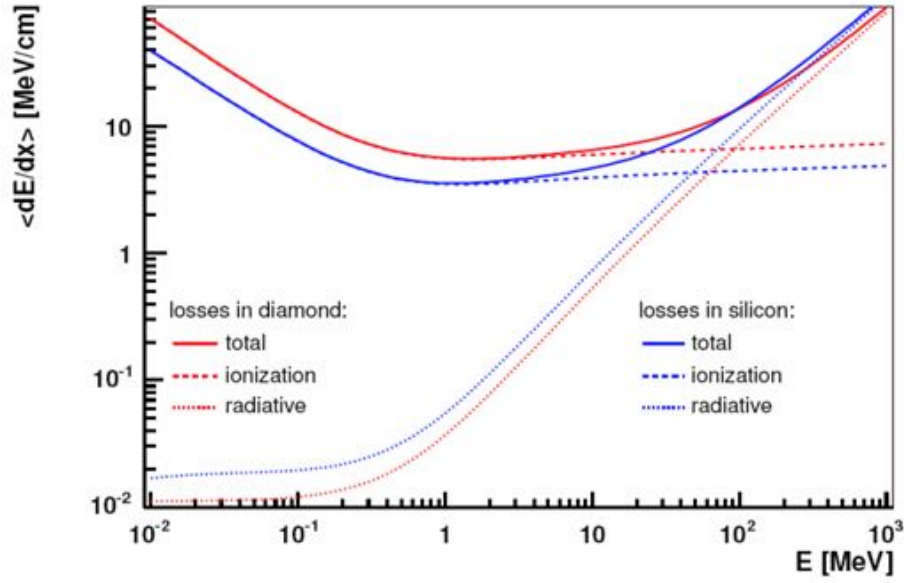
Figure 16: Combination of the energy losses due to ionisation and radiative effects for electrons in diamond and silicon materials [36].
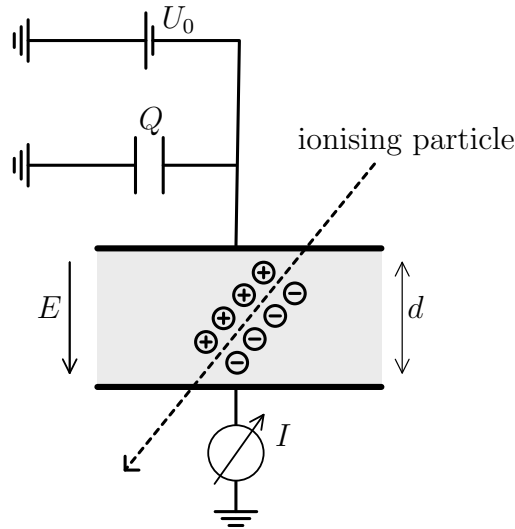
Figure 17: Schematic layout of a diamond based detector. The bias voltage U_0 creates an electric field E in the diamond crystal. The impinging particle creates charges while traversing through the crystal of width d. The created current which is proportional to the impinging particle intensity is then measured. The capacitor Q is a buffer which helps stabilising the electric field.

4.2 The diamond-based beam loss monitor

As the name indicates, the active medium of diamond based beam loss monitors (dBLM) is a diamond crystal, which is metalised from two opposite sides to form the electrodes. The applied bias voltage U_0 creates the electric field E in the crystal. Traversing particles create electron-hole pairs in the diamond crystal. The electrons and the holes drift along the field in the direction of the anode and cathode. The induced current which is proportional to the impinging particle intensity is then measured. In Fig. 17 the schematic layout of a dBLM is displayed.

Signal creation in a diamond based detectors

The typical gradient of the electric field created by the bias voltage is $1\,\text{V}/\text{µm}$ [22]. A minimum ionising particle (MIP) creates in average 36 electron hole pairs per µm [37], [38], [36]. The self space charge forces are weak compared to the separating force of the external electrical field. With parallel electrodes creating the electric field the force acting on the electrons and holes can be written as

$$F = \frac{qU_0}{d} \tag{6}$$

with the charge q, the electric field U and the thickness of the material d. Following the Shockley-Ramo theorem the moving charges induce a current I on the electrodes. The current is expressed as a function of the charge drift velocity v and the thickness of the material. The drift velocity depends on the electrical field and the charge mobility:

$$I = \frac{qv}{d} \quad \text{with} \quad v = \mu E \tag{7}$$

The current density i on the electrodes can be calculated by using equation Eq. (7) and the charge density ρ. Both expressions are time dependent:

$$i(t) = \rho(t)\mu E \quad \text{with} \quad \rho(t)\mu = \rho_-(t)\mu_- + \rho_+(t)\mu_+ \tag{8}$$

The charge density is a superposition of the movement of both types of charge carriers, electrons and holes, see Eq. (8).

---

[22] The electric field has to be stronger than the self space charge effects of the created charges, which could lead to the recombination of the electron hole pairs. Still, a charge multiplication due to additional ionisation created by the drifting charges has to be avoided.

Crystal defects and impurities can cause charge trapping, which enhances recombination of the electrons with the holes. Taking the recombination effect into account a mean lifetime τ of the charge carriers can be introduced:

$$i(t) = \rho(t)\mu E \cdot e^{-t/\tau} \tag{9}$$

The integration of the current density over time gives the collected charge (Q_{coll}). The ratio of the collected charge and the charge created by ionisation in the diamond crystal ($Q_{ionisation}$) is called charge collection efficiency CCE, which is an important parameter of diamond based beam loss monitors. The expression for the charge collection efficiency is given in Eq. (10) with n_p the number of ionising particles traversing the crystal creating 36 electron-hole pairs per µm.

$$CCE = \frac{Q_{coll}}{Q_{ionisation}} = \frac{Q_{coll}}{n_p\, e \cdot (36\, d)} \tag{10}$$

The charge collection distance (CCD) is the second characterising parameter. It is the mean free path length (MFP) of the charge carriers before they are stopped by the crystal's surface or by a local effect, e.g. at the grain boundaries in polycrystalline diamonds. The charge collection distance is calculated from the thickness of the diamond crystal and the mean free path length:

$$CCD = \sum_{k=e,h} MFP_k \left(1 - \frac{MFP_k}{d}\left(1 - e^{-\frac{d}{MFP_k}}\right)\right) \tag{11}$$

The relation between the charge collection distance and the charge collection efficiency is given in Eq. (12).

$$CCD = CCE \cdot d \tag{12}$$

The exposure of the crystal to particle radiation will lead to damages in the crystal increasing the probability that the drifting charges are trapped, which leads to a reduction of the charge collection distance and the charge collection efficiency. In Fig. 18 the charge collection distance over the fluence, i.e. the number of particles, which traversed the diamond crystal, is shown. A decrease of the charge collection distance was observed at particle fluences above 1×10^{15} particles.
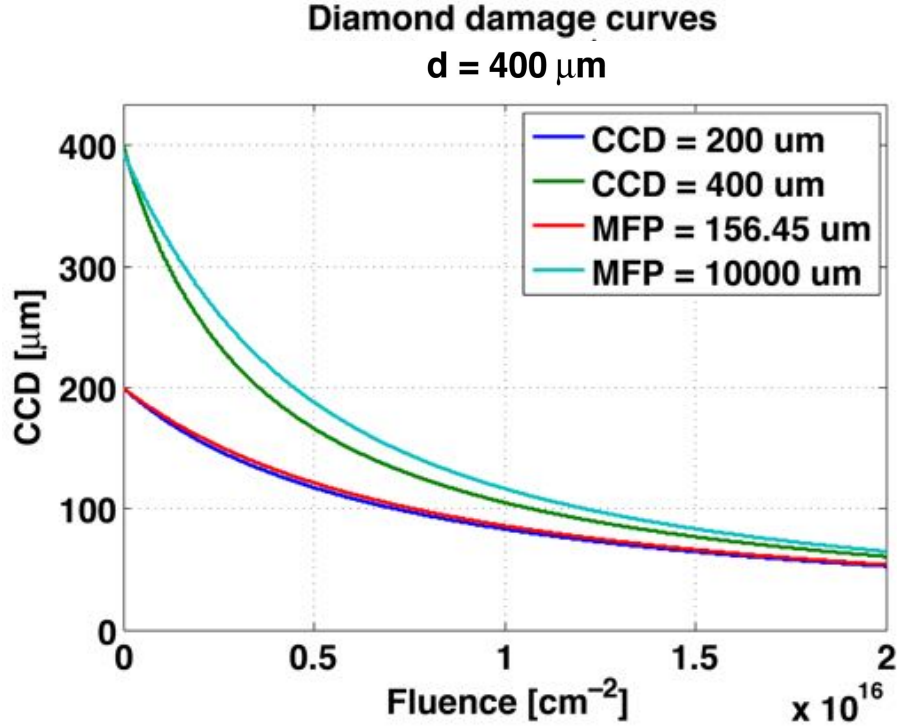
Figure 18: Damage curves of diamond crystals with different charge collection distances and means free path lengths. The CCD decreases with the increasing particle fluence [36].

Properties of diamond crystals

In this section the properties of the diamond crystals are discussed. Since silicon is a widely used material for detectors its properties are displayed for comparison. The key parameters of diamond and silicon are listed in Tab. 4. Diamond crystals have the characteristics of an insulator or of a semiconductor with a wide band gap respectively. The band gap is $5.45\,\mathrm{eV}$ for diamonds, which is very wide compared to typical semi-conductors like silicon with $1.12\,\mathrm{eV}$. This means the diamond crystal has a very high resistivity which results in dark currents in the order of only pico amperes. The stopping power, the energy loss per µm, in diamond is about $550\,\mathrm{eV/µm}$. From the stopping power the average number of 36 electron-hole pairs per minimum ionising particle can be calculated. The high electron and hole mobility of $1800\,\text{-}\,4500\ \mathrm{cm/Vs}$ for electrons and $1200\,\text{-}\,3800\ \mathrm{cm^2/Vs}$ for holes results in a much faster signal pick up than in silicon.

The radiation hardness of diamond crystals for hadron radiation at energies above $0.1\,\mathrm{GeV}$ is almost a magnitude larger compared to silicon crystals [39].

Table 4: Properties of CVD diamond crystals and silicon [36],[38]

Parameter		Diamond	Silicon
Density	g/mc^3	3.52	2.32
Bandwidth	eV	5.45	1.12
Stopping power per MIP	eV/μ	550	350
Resistivity	Ωcm	10^{13}-10^{16}	2.5×10^5
Breakdown field	V/cm	10^7	3×10^5
Electron-hole pairs per MIP/µm		36	100
Electron mobility μ_-	cm^2/Vs	1800 - 4500	1350
Hole mobility μ_+	cm^2/Vs	1200 - 3800	480
Radiation length	cm	18.8	9.4

Types of diamond detectors

In the context of this thesis two different types of diamond based beam loss monitors (dBLM) are used. Both types were grown in an epitaxial process with the chemical vapour deposition method (CVD) [40], but they differ in the crystalline structure of the diamond. The two crystal structures are shown schematically in Fig. 19. The grey coloured part indicates the substrate on which the crystal (white) was grown. Depending on the initial substrate and the growth process the resulting crystal structure is either single crystalline or polycrystalline. Single crystalline diamonds have no grain boundaries or other defects, which can lead to recombination effects due to charge trapping. As a consequence the average life-time of the charges is large compared to the drift time through the diamond bulk resulting in very high charge collection efficiencies. In this thesis charge collection efficiencies larger than 95% were considered for the singe crystalline detectors.

The second dBLM type is based on a polycrystalline diamond. The seed substrate is a composition of multiple crystals with different orientations. This leads to grain boundaries between different diamond domains during the growth process. These boundaries can cause charge trapping and thus recombination of free electrons and holes. This results in a reduced charge collection efficiency. The charge collection efficiency strongly depends on the grain boundary density, which can vary between different crystal samples. The polycrystalline diamond based particle detectors used at the LHC have a charge collection efficiency in the range of 20% - 40%.

The accumulated fluence of the installed detectors due to prior installation at the LHC or characterisation tests is in the order of 1×10^{10} particles.
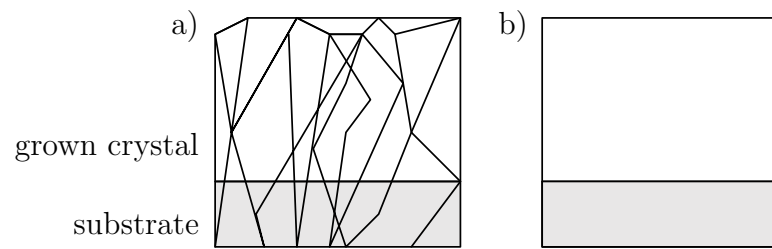
Figure 19: Poly (a) and single (b) crystalline diamond structures. The crystal (white) is grown on an initial substrate (grey). The crystalline structure of the initial substrate determines the resulting crystal.

5 Measurements of the detector response of polycrystalline dBLMs with a 500 MeV electron beam

Beside qualitative measurements the dBLMs will be used for quantitative measurements as well. In order to calculate the intensity of impinging particles from the signal the detector response is required. In addition to quantitative measurements the information about the detector response allows the prediction of the signal heights for a known particle intensity impacting on the detector. For for new dBLM installation the data acquisition system can be adjusted so it can cope with the expected signals without being limited due to resolution limits. For LHC type dBLMs this function is known in the regime below 10^4 particles per pulse [41]. In the scope of this thesis the response functions of two LHC type dBLMs in the intensity range from 5×10^3 up to 2×10^7 particles per pulse were measured. To determine the response function characterisation experiments were performed at the beam test facility (BTF) at the INFN in Frascati, Italy [42][43]. At this test facility electron bunches with an energy of $500 \, \text{MeV}$ were directed onto the diamond crystal of the dBLM. Since the response function of LHC ionisation chamber beam loss monitor is known, this type of detector was used as a reference for calculating the intensity of the impinging particles.

Table 5: Parameters of the beam configuration during the characterisation tests at the beam test facility (BTF)

Parameter	
Particles	electrons
Beam energy	$500 \, \text{MeV/c}$
Repetition rate	$1 \, \text{Hz}$
Intensity per pulse	10^5 to 10^9 electrons
Pulse length	$10 \, \text{ns}$
Beam size $(\sigma_x \times \sigma_y)$	$2 \, \text{mm}$ x $2 \, \text{mm}$

5.1 The beam test facility and beam parameters

The Beam Test Facility is operated in parasitic mode in respect to the DAΦNE collider ring. The initial electron beam consisting of a long bunch train is provided by a drift tube linac. Downstream of the linac and diagnostic stations a kicker magnet steers single electron bunches into the test facility beam line. The intensity of this electron bunch is in the order of 1×10^{10} with a duration of 10 ns. The pulse by pulse repetition rate was 1 Hz. All relevant parameters of the beam test facility are listed in Tab. 5.

In the DAΦNE ring electrons and positrons are collided. To provide continuous operation the collider has to be refilled frequently. Therefore positrons and electrons are produced variantly. During the positron production no beam was available in the beam test facility. The production mode was changed every 20 to 30 minutes. The beam intensity can be adjusted with movable slits. Several pairs of these devices are inserted in the beam line and allow scraping of the beam in the horizontal and vertical plane. The schematic layout of the beam line towards the test facility is displayed in Fig. 20.
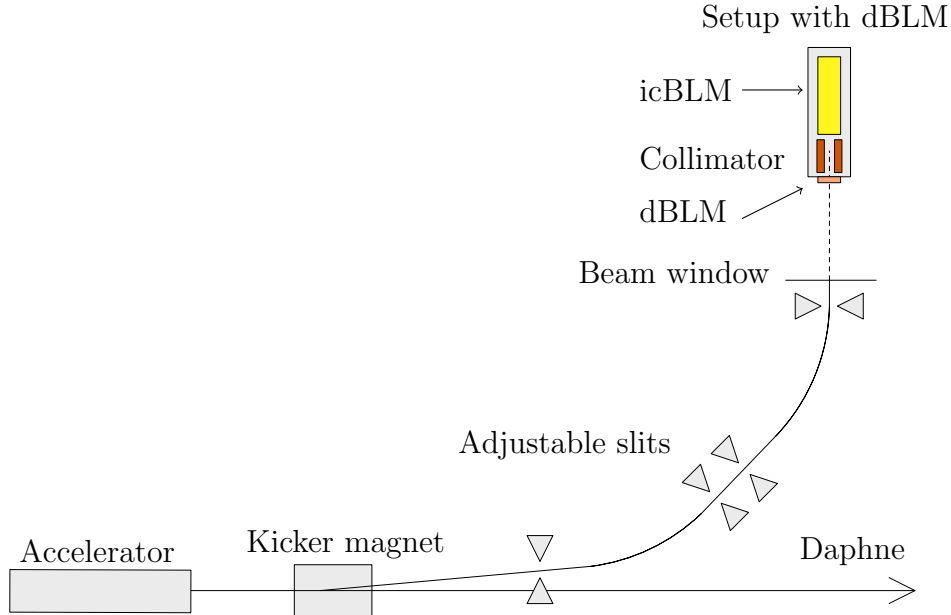
Figure 20: Layout of the beam line providing electron beams to the test facility. The bunch train is created in the linear accelerator. The last bunch of the train is kicked by a fast magnet into the beam line towards the test facility. The beam intensity is adjustable by moving slits into the beam. The setup is aligned to the electron beam.

5.1.1 Detector setup in the beam test facility

The schematic layout of the experimental setup is displayed in Fig. 21. The setup with the diamond based detector was positioned on the electron beam axis in the test hall. The distance between beam window and dBLM was 0.35 m. The icBLM was installed downstream of the dBLM. A collimator was installed between the two detectors in order to guarantee that only particles are recorded in the icBLM, which passed through the dBLM. This collimator consisting of a sequence of hollow copper and lead cylinders absorbing the electrons. The opening of the collimator direct downstream of the dBLM was 10 mm. In order to allow a beam deviation of 10 mrad the collimator opening was increased from 10 mm to 13 mm over a length of 15 cm[23]. The length of the lead cylinder was 6 cm with an opening of 15 mm. The losses due to shower creation between the dBLM and icBLM are taken into account in the error estimation of the icBLM signal. For these measurements the contribution of gamma radiation to the signal is assumed to be about two orders of magnitude lower than the contribution of the charged particles. Therefore electromagnetic radiation effects are negligible. The setup was shielded with lead in order to keep the prompt radiation below the limits of the beam test facility.
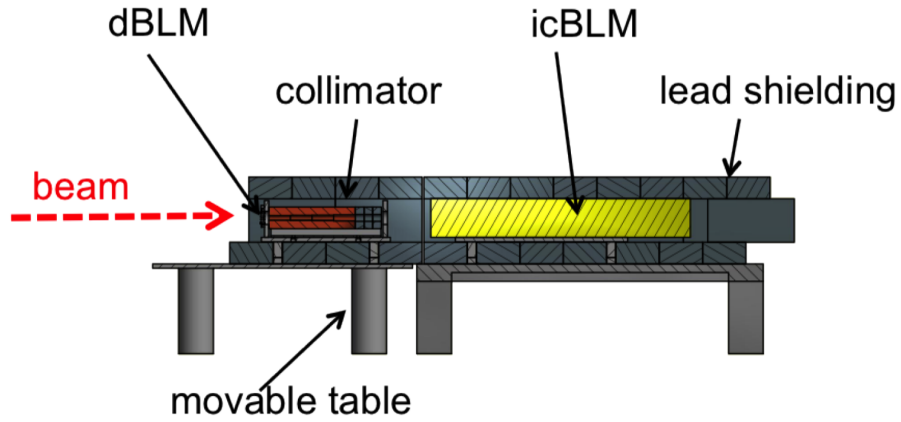

Figure 21: Schematic layout of the test setup. The diamond based particle detector (dBLM) and the reference detector (icBLM) are aligned to the electron beam axis. A collimator guaranteed that only particles which passed through the dBLM hit the icBLM.

---

[23] 15 cm is about ten times the radiation length of copper $\lambda_L = 1.436$ cm.
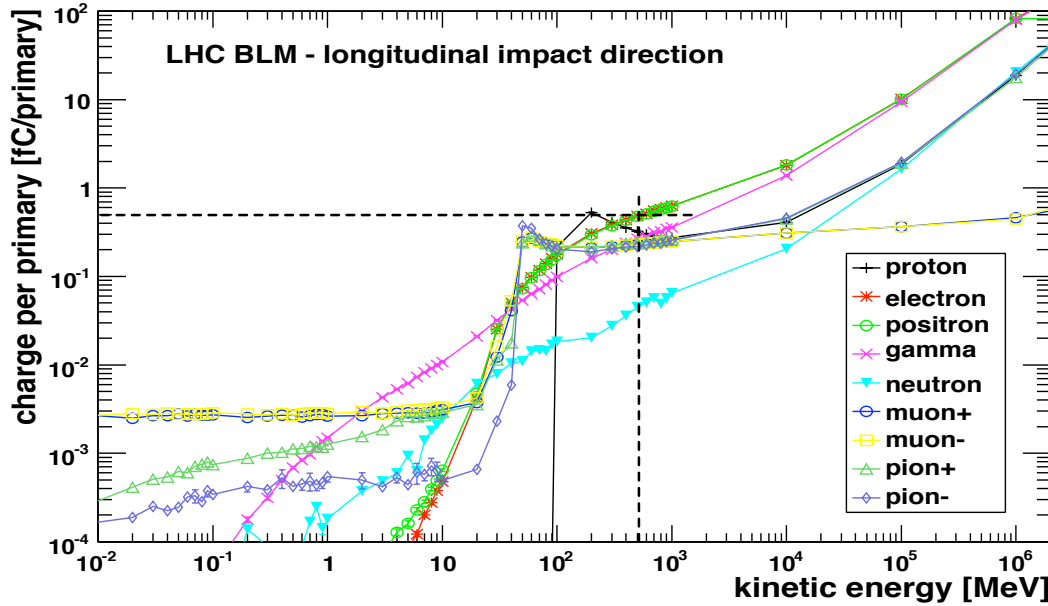
Figure 22: Charge per particle ratio for different particle types over the particle
energy. The dashed lines indicate the conversion factor of 0.5 fC for
500 MeV electrons. Below a certain threshold, e.g. 3 - 4 MeV for elec-
trons and positrons, the particles are absorbed by the detector walls so
they do not reach the active detector volume. For particle energies above
1×10^4 MeV the signal increases almost linearly due to secondary particle
production [44].

5.1.2 Using the LHC ionisation beam loss monitor as a reference detector

The response functions of the ionisation chamber beam loss monitor for different
impinging particle types and energies are known, see Fig. 22. For an electron beam
with an energy of 500 MeV the detector response is 0.5 fC per particle. This allows
a direct conversion of the signal into particles intensities. An impinging particle
ionises the neutral gas and creates electrons and ions, which drift along the electric
field towards the electrodes. It is assumed that the same amount of charge carriers,
electrons and ions, arrive at the electrodes. Therefore, the electrons and the ions
contribute in equal parts to the signal. Trapping effects at the electrodes are as-
sumed to be negligible. Recombination effects reduce the amount of charge carriers
equally.

Due to the different masses of the charge carriers, the electrons have a much higher
mobility, which results in a faster signal response than the signal from the ions.
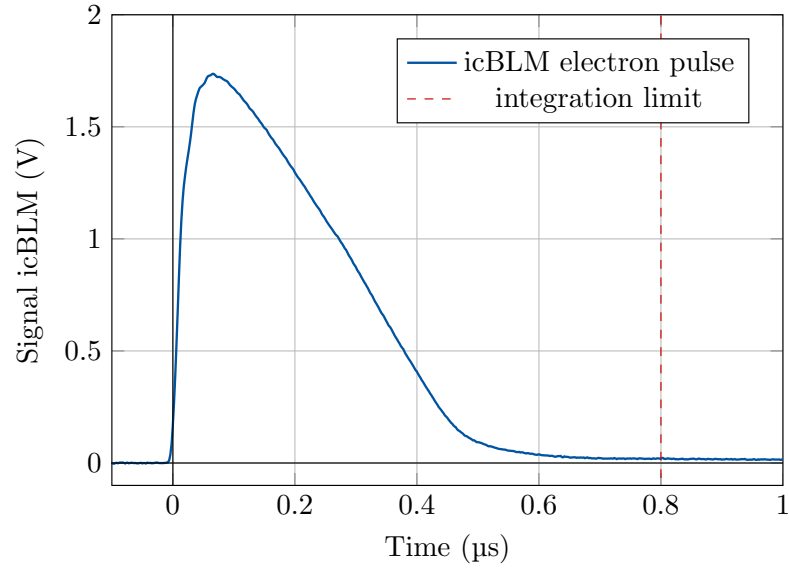
Figure 23: Averaged electron pulse shape of the icBLM. The signal created by the much more mobile electrons is about 0.8 µs long and has an amplitude of 1.7 V, which is much higher than the ion pulse.
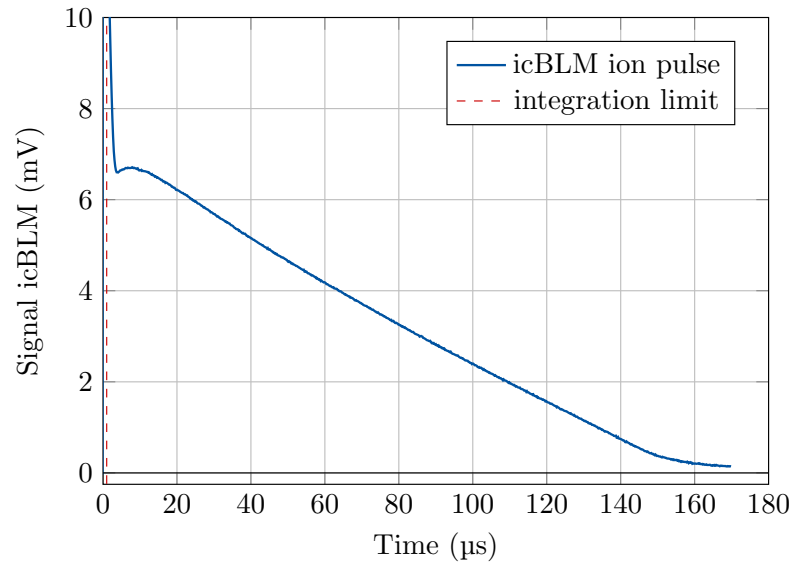
Figure 24: Averaged ion pulse shape of the icBLM. Compared to the electron pulse the signal created by the ions is much longer, about 170 µs. The amplitude is about 6.8 mV. The integrals of the electron signal and the ion signal are the same.

In Fig. 23 and Fig. 24 the averaged shape of the electron part and the ion part of the signal are shown. The length of the electron and ion pulses were calculated from the integrals of the signals. By averaging over more than 50 measurements the signal fluctuations were taken into account. The length of the electron pulse per shot was $0.8 \pm 0.05\,\mu s$. The signal of the ions is about $170\,\mu s$. The red dashed line in Fig. 23 and Fig. 24 separates the electron part of the signal from the ion part. The integrals of both parts are equal. During the characterisation measurements of the dBLMs only the electron signal was recorded.

5.2 Results of the characterisation experiments

For both detectors, L1 and L2, more than 5000 data sets were recorded. For the detector L1 measurements were performed in the intensity range of 3×10^3 up to 3×10^7 electrons per shot. For the detector L2 a range between 1×10^4 and 3×10^7 electrons per shot was covered.

5.2.1 Calculation of the particle intensity per shot

The actual particle intensity per shot was calculated by integrating and doubling the electron signal of the reference detector. With the known signal to particle conversion factor of $0.5 \, \mathrm{fC}$ the particle intensity was derived, which was introduced in chapter 5.1.2. The error for this conversion factor is assumed to be $2.5\,\%$. The estimated error of the standard ionisation chamber beam loss monitors (icBLM) signal is $5\,\%$ of the signal integral. Following the propagation of uncorrelated uncertainties the error of the intensity per shot was calculated.

5.2.2 Detector responses

In Fig. 25 the data of the response measurements of dBLM L1 are shown. For the measurements of intensities below 10^5 electrons/bunch no shunt or attenuator was used. In order to cover the whole intensity range the readout electronics had to be adjusted to cope with the high signals above 10^5 electrons/bunch. For high intensities a 1-Ω-shunt system[24] was used. At the lower ends of the intensity range of both acquisition configurations an increase of the data spread is visible. In the data sets of the second detector, L2, no increase of the signal spread is visible at the lower ends of the intensity ranges of the used setup configurations, see Fig. 26. In this case the signals were attenuated by $20 \, \mathrm{dB}$ in the lower intensity regime. With this setup the overlap of both configurations was increased. The data sets from the two different setups overlap nicely.

---

[24]Attenuators and shunts are used to protect the data acquisition system from too high voltages and currents at the input channel of the readout electronics.
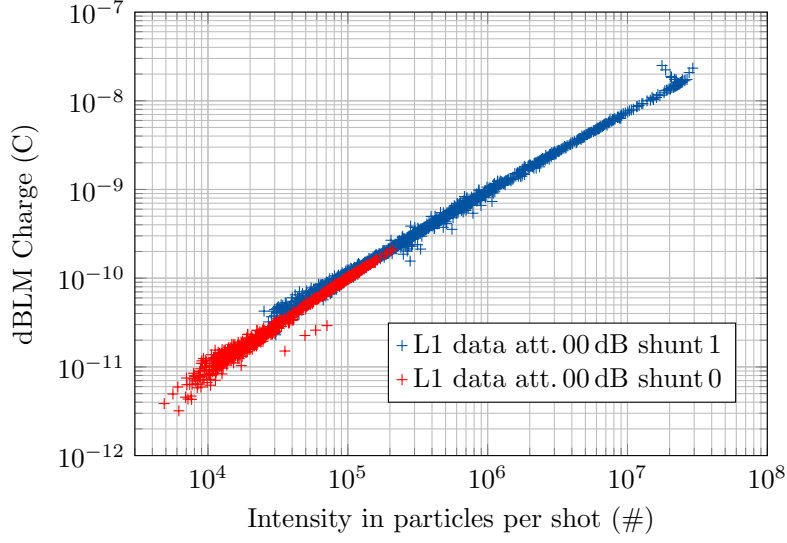
Figure 25: Response measurements of the detector L1. Two acquisition configurations were used. No shunt or signal attenuation in the intensity regime of less than 10^5 electrons/bunch. A 1-Ω-shunt system was used for measurements in the intensity regime of more than 10^5 electrons/bunch. The measurements with both configurations overlap.

Figure 26: Response measurements of the detector L2. Two acquisition configurations were used. The signal was attenuated by 20 dB in the intensity regime below 4×10^6 electrons/bunch. A 1-Ω-shunt system was used for measurements in the intensity regime of more than 10^5 electrons/bunch. The measurements with both configurations overlap.

Figure 27: Charge collection efficiency (CCE) of the LHC type dBLM L1.

Figure 28: Charge collection efficiency (CCE) of the LHC type dBLM L2.

5.2.3 Charge collection efficiencies of the tested detectors

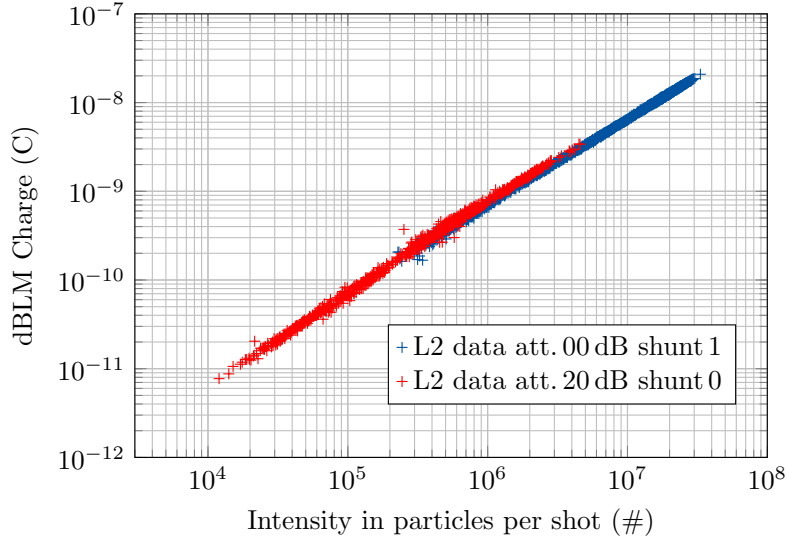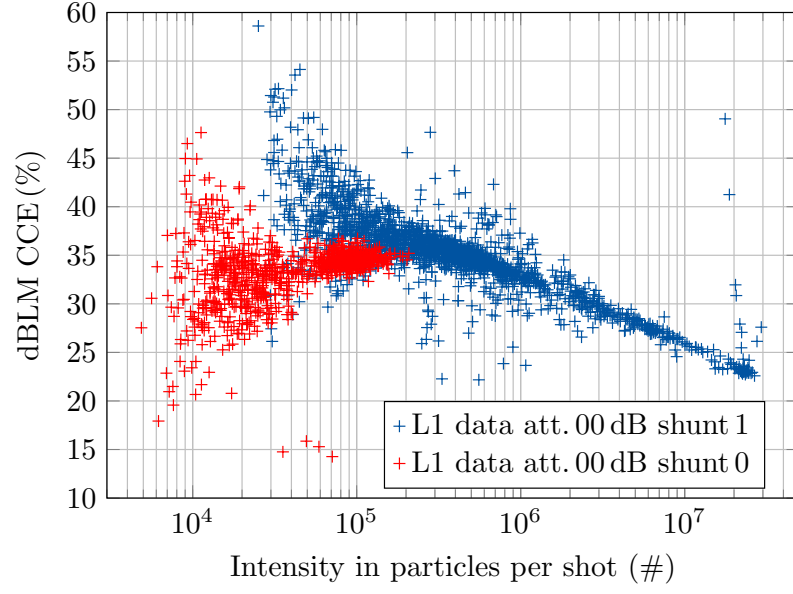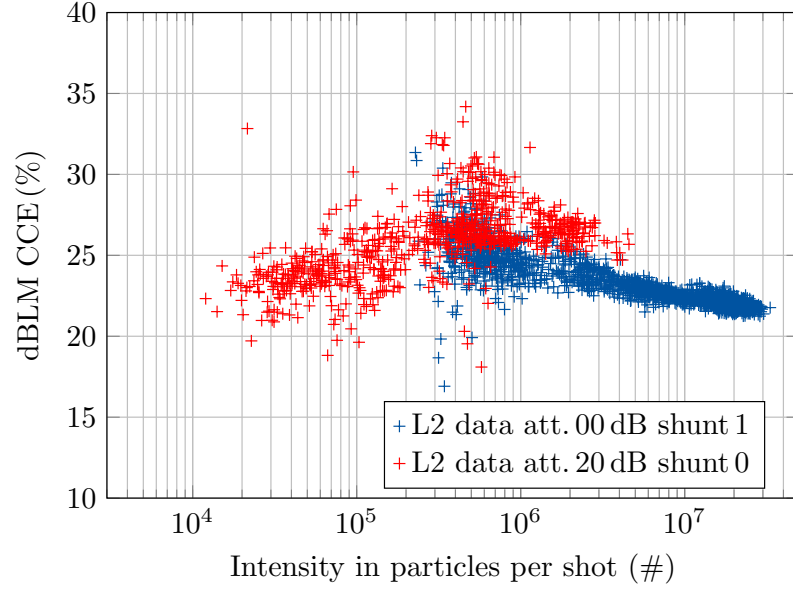The charge collection efficiency (CCE) can be calculated from the response data by using formula Eq. (10). The first detector, L1, has a charge collection efficiency in the range from 1×10^3 to 2×10^5 particles per shot of about 30% to 35%. Above this intensity the charge collection efficiency drops down to 25% as shown in Fig. 27. The above mentioned widening of the signal results in a wider spread of the detector efficiency data[25].

The charge collection efficiency of the second detector, L2, is about 25 %. Similar to L1 a reduction of the charge collection efficiency is visible at high intensities. However, in this case the charge collection efficiency drops only by two to three percent, see Fig. 28.

5.3 Discussion of the dBLM characterisation results

For both detectors the data from the measurements with the two setup configurations overlap nicely. The differences in the data trends between the two setups is very small. The increase in the data spread which can be observed in the measurements of the detector L1 results from the resolution limits of the data acquisition system due to internal settings. Due to these limits the signal to noise ratio was not sufficiently large enough. The random noise in the electronics had large impact on the signal integrals. This caused the wide spread in the data. With higher signals the signal to noise ratio improved so that the spread decreased for higher intensities. The setup configuration for the measurements of L2 were optimised to avoid the increase of the data spread due to the readout electronics resolution limits.

The response and the data spread for both detectors are shown in Tab. 6. The spread is displayed as the standard deviation of the data for the given intensity in percent in respect to the mean response of the detector.

As previously stated the spread of the response in the lower intensity regime is relatively large for the L1 detector. For higher intensities and both detectors the spread is below 10%. The spread of the L1 efficiency data is correlated to the response data, see Eq. (10).

In Fig. 27 and Fig. 28 a decrease of the charge collection efficiency above an intensity of 10^5 electrons per shot is visible. This efficiency decrease is more distinctive for the L1 detector with a higher overall efficiency compared to the L2 detector. The decrease of the charge collection efficiency is small compared to the covered intensity range. The decrease of the charge collection efficiency is a result of the high ionisation in the diamond. The created charges start drifting towards the electrodes where they obstruct the electric field which results in a reduction of the electric

---

[25]Due to the linear representation of the efficiency the spread is more visible.

field strength in the diamond. In addition, the trapping of the charges at the grain boundaries in the polycrystalline diamond reduces the electric field strength in these regions. The probability of recombination electrons with holes increases due to the reduced field strength. This effect can be compensated by increasing the bias voltage. The efficiencies of both detectors are in the expected range from 20 to 40 %. The difference between the two detectors is about 10 % of the total efficiency.

Table 6: Detector response of L1 and L2 and their standard deviations for a given intensity

Intensity (#)	L1 resp. (C)	σ L1 (%)	L2 resp. (C)	σ L2 (%)
1×10^4	8.8×10^{-12}	15.0		
5×10^4	5.3×10^{-11}	21.0	3.3×10^{-11}	3.5
1×10^5	1.0×10^{-10}	6.5	6.8×10^{-11}	7.5
5×10^5	5.0×10^{-10}	4.4	3.8×10^{-10}	7.5
1×10^6	9.7×10^{-10}	6.4	7.0×10^{-10}	5.0
5×10^6	4.0×10^{-9}	4.3	3.3×10^{-9}	3.0
1×10^7	7.4×10^{-9}	2.5	6.4×10^{-9}	1.6

5.4 Conclusion

The characterisation experiments at the beam test facility were successful. Two LHC type diamond based detectors, L1 and L2, were tested in the range of 3×10^3 to 3×10^7 electrons per shot. The responses for both detectors have been derived, see table 6. The wide spread in the L1 data results from resolution limits in the data acquisition system. Both detectors show charge collection efficiencies in the expected range between 20% and 40%. The efficiencies of both detectors differ by 10% to 15% due to their individual polycrystalline structure. For both detectors the observed efficiency drops above intensities of 10^5 electrons, which can be caused by saturation effects and charge trapping in the diamond crystal. The drop of the charge collection efficiency is small compared to the covered intensity range. The measurements show which intensity regimes the LHC type diamond based beam loss monitors can be used and which configurations of the readout electronics are needed. For measurements in the regime of 1×10^4 up to 1×10^6 particles an attenuator of 20 db can be used for reducing the voltage peaks at the input channel of the readout electronics. Above these intensities the readout system can be protected from high currents by installing a shunt. The measurements have shown that these detectors can be used for measuring fluencies up to 1×10^7 particles/10 ns. For

measurements in the intensity regime above 1×10^6 particles per shot an increase of the bias voltage can compensate saturation effects. This defines the intensity range in which the LHC type diamond based beam loss monitors can be used for particle detection. If absolute measurements shall be performed a characterisation of every single diamond based detector is necessary in order to determine the efficiency for every detector.

6 Diamond based beam loss monitors at the LHC

The diamond based particle detectors qualify as fast beam loss monitors, which allows the detection of the time structure of the very fast and even ultra fast beam losses with nanosecond time resolution. Therefore, in the content of this thesis two different types of dBLMs were installed at different positions in the LHC where these losses occur. The positions of the dBLMs and the data acquisition systems will be presented in the following section.

6.1 Diamond based beam loss monitors for measurements of ultra fast beam losses with high time resolution

For the beam loss measurements two types of dBLMs are installed. The LHC type dBLM is based on a polycrystalline CVD diamond. The second type is the CMS type detector based on a single crystalline CVD diamond system, which is used by the CMS collaboration.

6.1.1 Properties of the LHC type dBLM and frontend electronics

The LHC type dBLM is based on a polycrystalline diamond with an area of $10 \times 10 \, \text{mm}^2$ and a thickness of $500 \, \mu\text{m}$. The applied bias voltage is $1 \, \text{V}/\mu\text{m}$, i.e. $500 \, \text{V}$. These detectors are provided by the CIVIDEC company [45]. Depending on the quality of the polycrystalline diamond bulk the efficiency of the dBLMs varies between 20% and 40%. The detector provides a time resolution in the lower nanosecond regime[26] due to the high charge mobility in the diamond crystal. All important properties of the LHC type dBLMs are summarised in Tab. 7.

The schematic layout of the frontend electronics of the LHC type dBLM are shown in Fig. 29. The AC/DC splitter decouples the DC signal from the raw dBLM signal so that only high frequency signals are transmitted. For specific applications, when the signal amplitudes are very small, amplifiers[27] are installed directly behind the splitter or the dBLM itself (no splitter). In Fig. 30 the current frontend electronics configuration of the dBLM installed on the left side of IR 7 for beam 2 is shown. In order to protect the data acquisition system from radiation, the readout electronics are installed in the side tunnels where the radiation during LHC operation is significantly lower. The detectors and the data acquisition systems are connected with up

---

[26]The double peak resolution is 5 - 6 ns.

[27]The used amplifiers are limited to $\pm 1 \, \text{V}$ output voltage. If the incoming signal exceeds the amplification limit the amplified signal will show saturation effects. This results in signal drops and undershoots of the wave form.

Table 7: Properties of the LHC type dBLM and its frontend electronics [45]

Parameter	
Type	dBLM
Crystal structure	polycrystalline CVD diamond
Area	$10\times10\,\text{mm}^2$
Thickness	$500\,\mu\text{m}$
Bias voltage	$1\,\text{V}/\mu\text{m}$
Charge collection efficiency	20 - 40%
Dynamic range	$< 5\times10^3$ - 5×10^7 particles/shot
Frontend electronics	
Signal shape	raw signal, no shaper
Double peak resolution	5 - 6 ns

to 400 m long signal cables[28]. The dBLMs' signals are recorded with two different readout electronics, either with an oscilloscope or with the CIVIDEC ROSY system. The oscilloscope allows time loss measurements with sampling rates up to 5 GHz. The CIVIDEC ROSY system provides two acquisition modes, the oscilloscope mode with time loss measurement and a histogram mode [46].
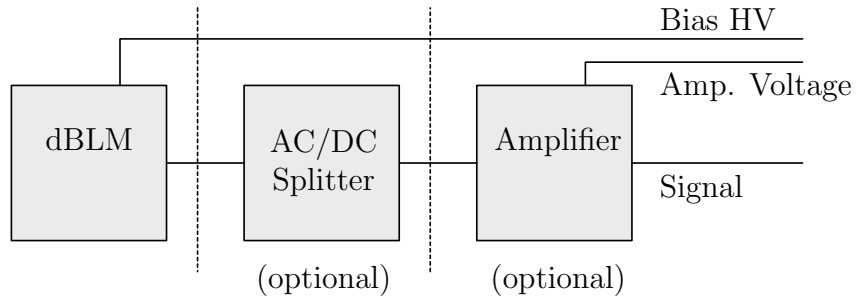

Figure 29: Schematic layout of the CIVIDEC type dBLM frontend electronics.

---

[28]CK50 coax-cables are used for signal transmission. These cables have attenuation factor below 1 dB/100 m for signals in the 10 MHz range.

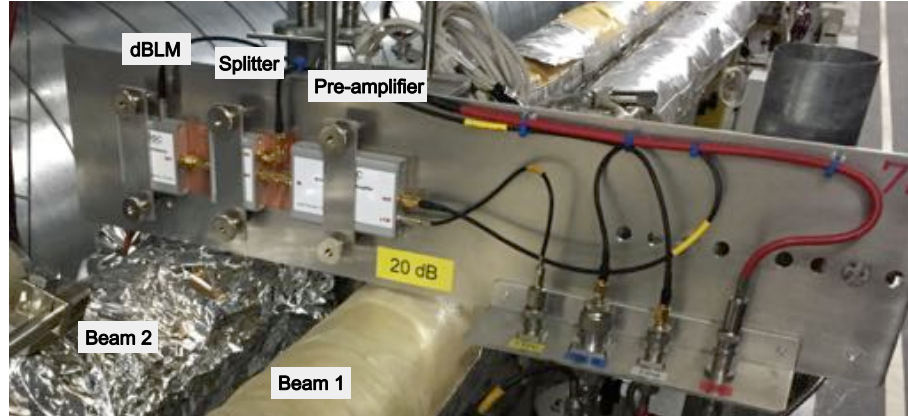Figure 30: Frontend electronics of the LHC type dBLM as it is installed in IR 7 beam 2. The dBLM is installed centred above the beam pipe of beam 2. The signal AC signal is split from the DC component by a splitter. The adjacent pre-amplifier amplifies the signal by 20 dB.
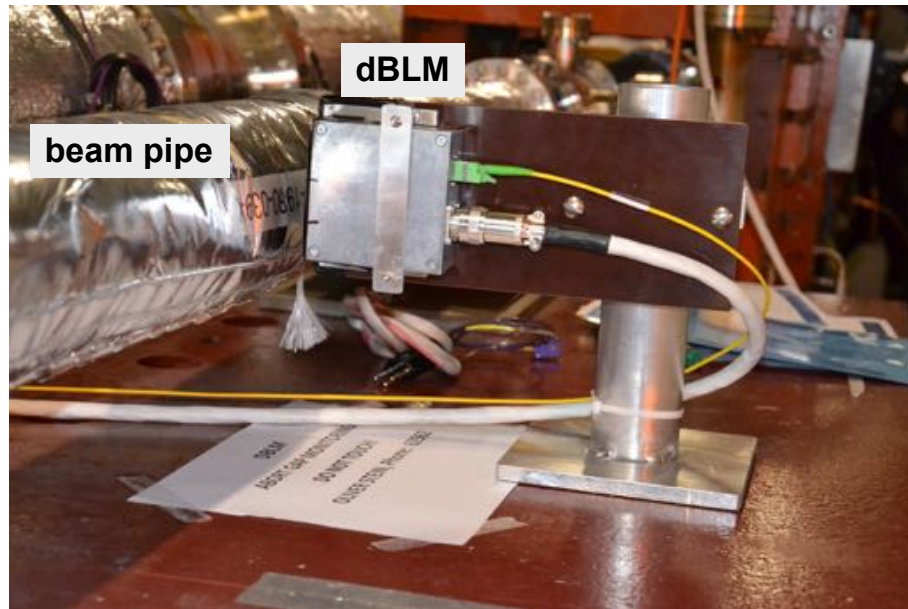

Figure 31: Installed CMS type dBLM in IR 4 of the LHC. The dBLM and the frontend electronics are housed in an RF-tight box.
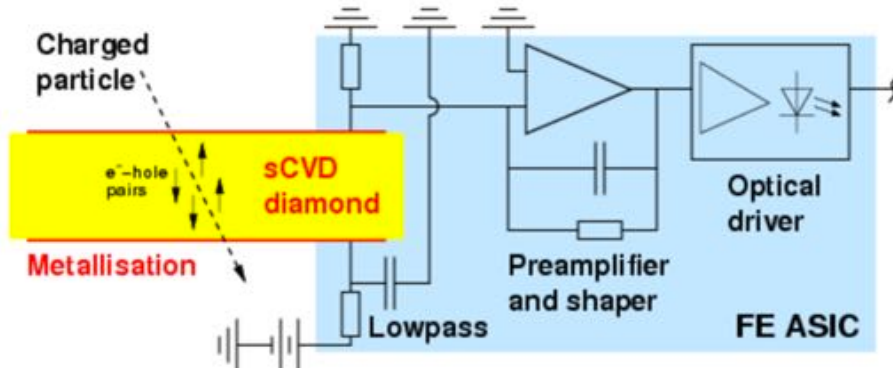
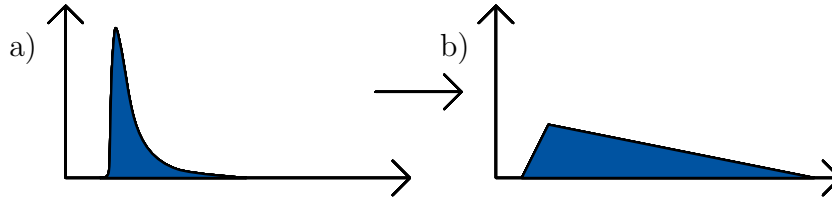Figure 32: Schematics of the CMS type dBLM frontend electronics [47].

Figure 33: The raw signal (a) is shaped to a triangular shape. The integral of the signal is preserved.

6.1.2 Characteristics of the CMS type diamond based beam loss monitor

The second type of diamond based beam loss monitor is adapted from the CMS collaboration for beam loss measurements at the LHC. At the CMS experiment diamond based detectors, the BCM1F, are used as beam arrival and quality monitors [36]. The single crystalline diamond has a size of $5{\times}5\,\mathrm{mm}^2$ and a thickness of $500\,\mathrm{\mu m}$. The bias voltage is $1\mathrm{V}/\mathrm{\mu m}$. Due to the single crystalline properties of the diamond bulk the efficiency is about 95%[29]. The properties of the CMS dBLMs are summarised in Tab. 8. The frontend electronics are housed in an RF-tight aluminium box, see Fig. 31. The bias high voltage, the power for the integrated pre-amplifier and the control cables are fed to the detector through a multi wire cable (grey). The signal is converted into an analog optical signal, which is then transmitted via an outgoing fibre (yellow). The schematics of the frontend electronics are displayed in Fig. 32 [47]. The shaper in the frontend electronics converts the raw signal into a triangular shaped signal as it is illustrated in Fig. 33, while the integral of the signal is preserved. The length of the transformed signal is about $100\,\mathrm{ns}$, which stays constant.

---

[29]The absorbed particle fluence of each detector is much smaller than the threshold for reducing the charge collection efficiency due to damages in the crystal structure.

Table 8: Properties of the CMS type BCM1F4LHC dBLM
and its frontend electronics [48]

Parameter	
Type	dBLM
Crystal structure	single crystalline
	CVD diamond
Area	$5 \times 5 \, mm^2$
Thickness	$500 \, \mu m$
Charge Collection Efficiency	$>95\%$
Bias voltage	$1 \, V/\mu m$
Frontend electronics	
Signal shape	shaped, triangular
Double peak resolution	$140 \, ns$

6.2 Comparison of the LHC type and CMS type dBLM

The two dBLM types differ in the used diamond crystal and the volume of the active material. For the LHC type detector a polycrystalline diamond is used, which have a charge collection efficiency of $20 \text{-} 40\%$. These detectors are used in radiation environments with an expected particle fluence above 1×10^3 particles/cm^2. Below these intensities the signal to noise ratio is very small and a reliable signal detection is difficult. The single crystalline CMS type dBLMs have charge collection efficiencies of more than 95%. These detectors allow measurements below 1×10^3 particles/cm^2. With an optimised readout electronics even single particles can be detected [49]. Therefore these detectors are excellent in environments with very low particle fluencies. The polycrystalline LHC type dBLMs have a surface area of $10 \times 10 \, mm^2$ and a thickness of $500 \, \mu m$, whereas the single crystalline CMS detectors have a surface area of $5 \times 5 \, mm^2$ and a thickness of $500 \, \mu m$. In addition, the two detector types require different infrastructure for the signal transfer to the readout electronics. The CMS type dBLM has a compact frontend electronic. The signal is converted in a shaped analogue optical pulse, which allows long distance signal transmissions. The frontend electronics of the LHC type dBLM is less compact and therefore allows the installation of additional attenuators or amplifiers in order to adapt the setup to the particle fluence. The signal is transmitted via an BNC cable, which limits the distance between detector and readout electronics to few hundred meters[30].

---

[30]The longest distance between the dBLM and the readout electronics is 400 m in IR 7.

6.3 Applications of the diamond based beam loss monitors and their position at the LHC

The diamond based beam loss monitors are installed in location where ultra fast beam losses occur. As stated in chapter 3, absorber blocks protect the downstream components from showers due to ultra fast beam losses. In most of the cases the diamond-based beam loss monitors (dBLM)s are installed downstream of these absorber blocks. The impinging particles create showers, which are measured with the dBLMs. Due to the Lorentz boost of the high energetic particles the shower has a dominant forward component. In order to get high signal amplitudes the detectors are installed close to the beam pipe where the shower intensities are the highest.
In total 10 dBLMs are installed around the LHC to detect the ultra fast beam losses. In Fig. 34 the positions of the dBLMs at the LHC are indicated. The colour indicates the dBLM type, green for the CMS type, yellow for the LHC type dBLMs. All installed detectors, their positions and the connected data acquisition systems are listed in Tab. 9.
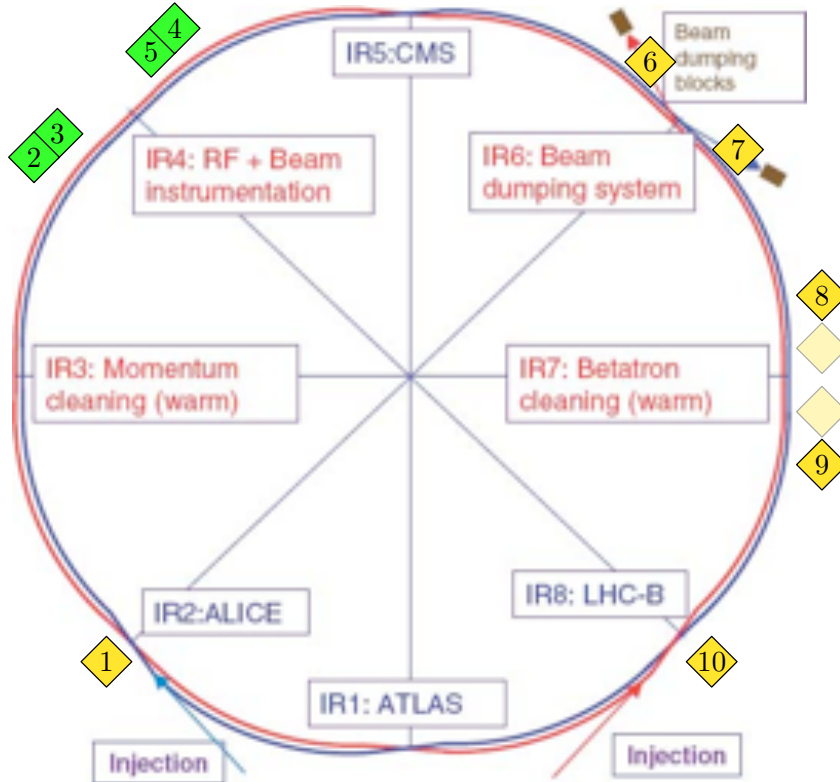

Figure 34: Positions of the diamond based beam loss monitors (2016). The LHC type dBLMs are marked yellow, the CMS type dBLMs are green.

6.3.1 Injection loss detection in IR 2 and IR 8

In IR 2 and IR 8 the injection systems are installed. Beam 1 is injected in IR 2 and circulates clockwise in the LHC. Beam 2 circulates counter-clockwise and is injected in IR 8. At the end of the transfer lines from the SPS, which transport the beams to the LHC, fast kicker magnets steer the beam into the LHC. During the injection process high amplitudes of ultra fast beam losses were observed. To measure these ultra fast losses LHC type dBLMs are installed downstream of the injection loss absorber block[31]. Mis-steered particles are intercepted by this block, so that the downstream elements are protected. The measurements of the injection losses with high time resolution lead to a better understanding of the loss process, see chapter 7.

6.3.2 Beam gas interaction measurements, IR 4

The LHC beams consists of sequence of bunches with a spacing of 25 ns. Beside the nominal bunches, the LHC is populated with very low particle intensities. Monitoring these particle intensities outside the nominal bunches is of interest for the LHC operators. Especially, the measurements of the particle population in the 3 µs long abort gap. An experimental setup of CMS type dBLMs is installed in IR 4 for demonstrating that dBLMs can be used for detecting showers from interactions of single circulating particles and the rest gas in the beam pipe. The dBLMs are installed close to the vacuum chamber of the beam gas ionisation monitor where neon gas can be injected into the vacuum for increasing the rest gas pressure. From the detection rate and the known rest gas pressure the intensity of the interacting particles can be calculated. The location of the beam gas interaction in the filling pattern of the beam can be identified due to the high temporal resolution of the diamond based beam loss monitors.

Detection of dump losses, IR 6

In IR 6 the dump systems are installed, one for each beam. In case of a dump the here installed dump kickers are synchronised to the abort gap of the beam. At nominal field strength the extraction kicker magnets deflect the beam into the dump lines, which direct the beam onto the dump block. The rise time of the extraction kickers is about 2.9 µs, particles passing the extraction kicker while the

---

[31]The TDI is installed 70 m, i.e. 90° phase advance, downstream of the injection kickers in order to protect the downstream components from losses during failures in the kicker magnets system. The TDI acts as a beam stopper in case the incoming beam is not deflected into the LHC by the kicker magnets.

magnetic fields are rising are mis-steered. Dedicated absorber blocks downstream of the extraction kickers intercept these particles and protect the downstream magnets. LHC type dBLMs have been installed downstream of these absorber blocks in order to measure the ultra fast losses. In case of an asynchronous beam dump the expected loss amplitudes are very high. The wide dynamic range of the dBLMs allows the measurements of these losses without saturating. Based on the analysis of extraction loss measurements the LHC type dBLMs were exchanged with special dBLMs. These dBLMs have a deliberately low charge collection efficiencies and a smaller active volume in order to avoid to high signal peaks in the readout electronics during an asynchronous beam dump[50]. Beside the mentioned properties these detectors are similar to the LHC type dBLMs, i.e. they require the same readout infrastructure.

Measurements of global losses in IR 7

In IR 7 the multi-staged collimator system is installed with the primary collimators forming the aperture bottle neck. If the particles deviate too much from the closed orbit they will be intercepted by the primary collimators. If particle trajectories change during their path around the LHC, the increase of their oscillation amplitude around the closed orbit will increase. This will lead to an increase of the particle losses on the primary collimator. In order to investigate the loss structure, for instance the contribution of single bunches to the losses, LHC type dBLMs have been installed downstream of the primary collimators.

Table 9: Diamond based beam loss monitors installed at the LHC (2016)

Nr.	Type	crystal	IR	beam	position (dcum)	bias volt.	AC/DC splitter	pre-amp	DAQ	DAQ type	trigger
1	CIVIDEC	pCVD	2	1	3254.00	500	no	no	scope	TL	sig/inj/dump
2	CMS	sCVD	4	1	9929.46	500			ROSY	HIST	sig
3	CMS	sCVD	4	1	9936.93	500					
4	CMS	sCVD	4	2	10064.71	500					
5	CMS	sCVD	4	2	10057.23	500					
6	LHC	pCVD	6	2	16505.54	100	no	no	scope	TL	sig/dump
7	LHC	pCVD	6	1	16817.85	100	no	no	scope	TL	sig/dump
8	LHC	pCVD	7	1	19799.78	500	yes	yes	ROSY	TL/HIST	sig
9	LHC	pCVD	7	2	20188.54	500	yes	yes	scope / ROSY	TL / TL/HIST	sig / sig
10	LHC	pCVD	7	2	23392.63	500	no	no	scope	TL	sig/inj/dump

7 Injection loss measurements at the LHC

As introduced in chapter 1 the losses in the injection region were continuously on high levels close to the dump threshold during the accelerator operation in 2015 and 2016. For a continuous and safe LHC operation these losses had to be reduced. The trains of proton bunches are prepared in a multi staged injector chain. For filling the LHC multiple injections of beam from the SPS are needed. The prepared beam is extracted from the SPS by fast extraction kicker magnets (MKE). Only when the extraction kickers are at their nominal field strength the beam is steered into the transfer lines towards the LHC injection regions. At the end of the transfer lines, in the injection regions of the LHC, fast injection kicker magnets (MKI) steer the incoming beam onto the closed orbit in the LHC. The injection kicker magnets have a rise time of $0.9\,\mu s$, a maximum flat top time of about $5.1\,\mu s$[32] and a fall time of about $3\,\mu s$. The whole injection process takes place within less than $15\,\mu s$, the high losses during the injection are categorised as ultra fast losses.

To investigate the structure of the losses diamond based beam loss monitors were installed in the two injection regions in the LHC. Figure 35 displays a loss signature of an injection of 72 bunches. With sampling rates of $1\,GHz$ and the high time resolution of the dBLMs the measurements show the detailed loss structure. The injected bunch train can be identified by it's loss signals[33]. The bunch train arrival at the injection kickers is synchronised to the beginning of the injection kicker magnets' flat top plateau, i.e. the kicker magnets are at their nominal field strength. The loss signature displayed in Fig. 35 shows an injection loss measurement where the bunch train was injected at $t = 0$. The amplitude of the loss signal recorded before the injection of the bunches ($t < 0$) is two orders of magnitude higher than the loss amplitudes of the bunch train. That means that the majority of the injection losses is not created by the nominal bunches but from particles which arrive ahead of the nominal bunches in the injection region. Due to their longitudinal position, in respect to the nominal bunch train these particles are not synchronised to the kicker magnets. Particles arriving ahead of the bunch train are mis-steered by the rising kicker fields, which leads to losses downstream of the injection kicker magnets. A similar effect was observed during the fall time of the kicker magnets due to particles trailing the injected bunch train. The contribution of these *longitudinal losses* is more than 95% to the whole loss signal for regular beam injections. In this section the underlying processes are described, which lead to these injection loss structures. Based on this knowledge, mitigation techniques and their implementation in the LHC operation are presented. Additionally injection failures and their detection by using dBLMs are discussed.

---

[32] The flat top time of the MKIs is variable and can be increased up to $11\,\mu s$.

[33] The loss signature of a bunch train shows a regular pattern of loss maxima with $25\,ns$ spacing.
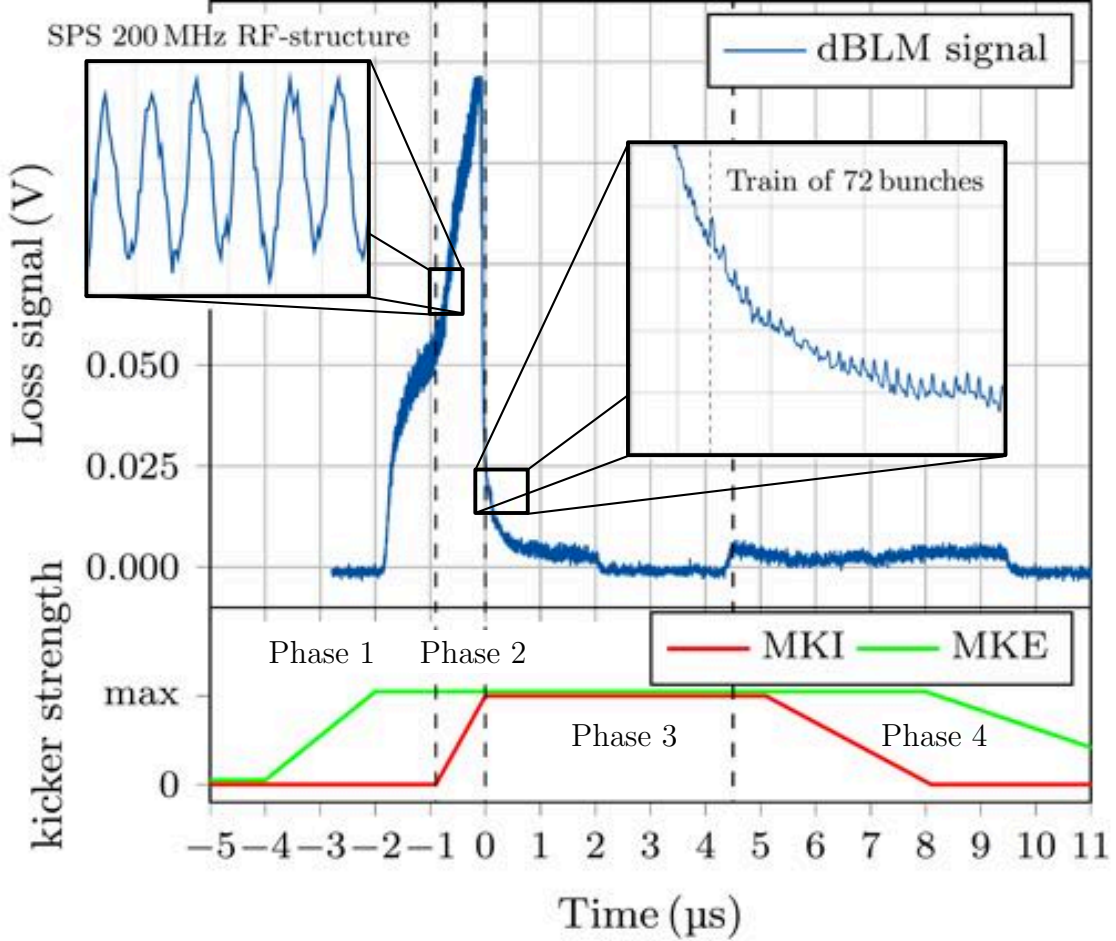
Figure 35: Loss signature of an injection of 72 bunches into beam 2 of the LHC. Only when the SPS extraction kicker magnets (MKE) are at their nominal field strength beam is transferred from the SPS towards the LHC. The zoom into the rising signal shows that the loss signature has a 200 MHz modulation, which correlates to the SPS RF-frequency. The second zoom into the loss signature at the beginning of the injection kicker flat top time allows the identification of losses from the injected bunch train. The amplitude of the losses in the injection region correlates with the deflection angle of the injection kicker magnets (MKI). The injection loss signature can be split into four phases correlating to the MKI conditions: MKI off, MKI rising, MKI at maximum deflection and MKI falling.
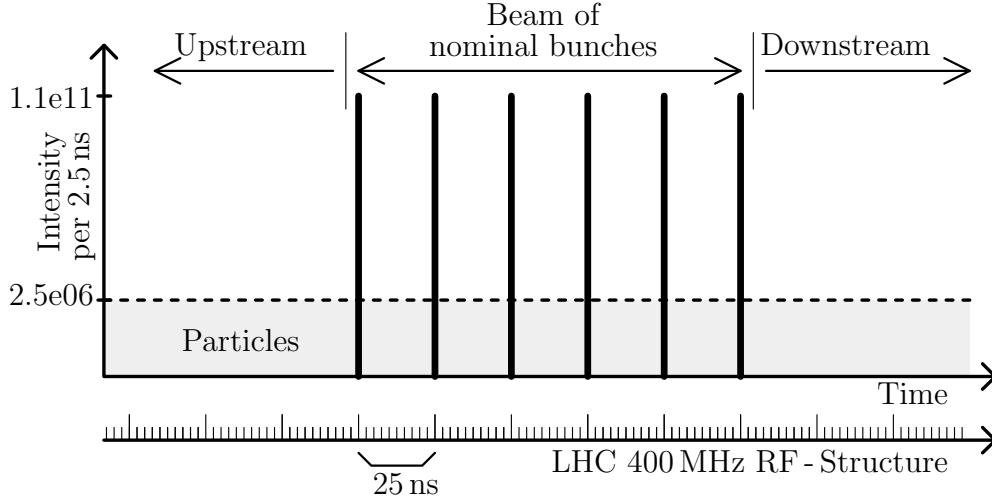
Figure 36: The LHC RF is operated at 400.8 MHz, i.e. one RF-period with one bucket is 2.5 ns long. The beam is composed of bunches with a spacing of 10 RF-buckets (25 ns bunch spacing) and a nominal bunch intensity of 1.15×10^{11} protons. Outside the filled buckets the LHC is populated with protons with an intensity of 2.4×10^6 protons/2.5 ns.

7.1 Identification of the longitudinal beam loss mechanisms

The proton beams consist of bunches. From summer 2015 on a bunch spacing of 25 ns was used, i.e. in a bunch train every 10th bucket of the 400.8 MHz RF-structure was filled. The proton intensity of a nominal bunch is 1.15×10^{11}. Beside the nominal bunches, the LHC can be populated with low intensities of particles, see Fig. 36. Whenever there is a mismatch between the transfer line and the LHC a small fraction of incoming particles is not captured in the RF-bucket resulting in coasting beam. Additional continuous diffusion effects cause an increase of the uncaptured particle intensities in the LHC, see chapter 2. During the beam preparation particles can be captured in buckets upstream and downstream of the nominal bunches. These particles have the correct longitudinal position and energy to be injected into buckets of the LHC RF-structure. Measurements have shown that the maximum particle intensities at injection plateau reached 3.3×10^6 protons/metre (2.4×10^6 protons/2.5 ns), which is five orders of magnitude lower than a nominal bunch [51]. In this thesis the proton beam is defined as the sequence of bunch trains consisting of nominal bunches, protons outside the nominal bunches are referred to as particles, which do not belong to the beam.

Measurements have shown that the injection loss signatures can be divided into four phases. These phases corresponds to the injection kicker magnets conditions, which are displayed in Fig. 37.

Phase 1: Injection kicker magnets off

In the first phase of the loss signature the kicker magnets are still off. Incoming particles are directed without deflection onto the absorber block (TDI) downstream of the injection kicker magnets, i.e. the particles impact on the absorber block with full impact parameter.

Phase 2: Rise of the injection kicker magnets

When the injection kicker magnets are triggered, the rising magnetic fields sweep the incoming particles over the absorber. In this second phase the impact parameter of the incoming particles change until the deflection angle is large enough to steer the particles into the LHC.

Phase 3: Injection kicker magnets at flat top

In the third phase the injection kicker magnets are at their nominal field strength, i.e. the kickers are at flat top. At the beginning of this phase the beam passes the kickers and the bunches are injected into the Large Hadron Collider (LHC). The first bunch in the bunch train is synchronised to the beginning of the flat top time.

Phase 4: Fall of injection kicker magnets

In the fourth phase the injection kicker magnets' fields are falling. Particle passing the kicker magnets during this phase are swept back over the absorber block until they hit the block with full impact parameter.

These four phases are indicated with dashed lines in the loss signature shown in Fig. 35. The plot below the loss signature shows the kicker strength. The loss signature changes for every phase of the kicker magnets. There are two sources, which result in particle distributions downstream and upstream of the bunch train resulting in longitudinal losses. The first cause for longitudinal losses are re-captured particles originating from the SPS, which are injected in the LHC with the nominal bunch train. The second cause for the longitudinal losses are mis-steered circulating particles.
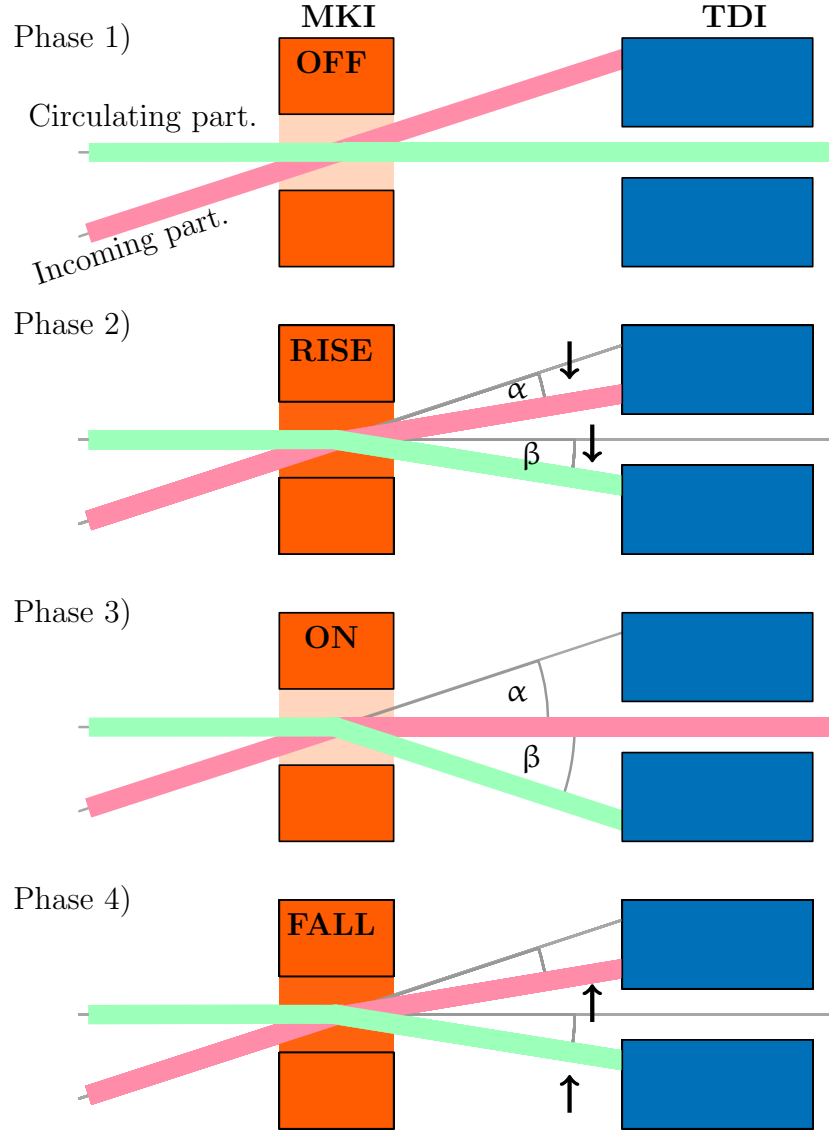
Figure 37: The four phases of the injection kicker, MKI. In phase 1) the MKI is off, no deflection. The incoming particles are absorbed by the TDI. The rising MKI field deflects the incoming and circulating particles in phase 2). The incoming particles are absorbed by the upper jaw, the circulating particles are absorbed by the lower jaw. The changing impact parameter during the rise of the MKIs' fields cause a change in the shower geometry of the impacting particles. In phase 3) When the MKI field is at its nominal strength (ON) the incoming particles and the beam are injected. The circulating particle hit the TDI with full impact parameter. In phase 4) is MKIs ramp down. The deflection angles α and β are the same. Only when the SPS extraction kicker magnet (MKE) is at nominal strength is beam transferred to the LHC injection regions. During the injection procedure no circulating beam should pass the MKI.

7.1.1 Losses due to re-captured particles

Re-captured particles populate the buckets upstream and downstream of the beam coming from the SPS. The intensities of the re-captured particles are in the order of 5×10^7 protons/5 ns. The re-capturing happens at the end of the injection plateau (injection energy) of the SPS. Due to an increase of the RF-voltage the bucket acceptance is increased so that coasting particles are re-captured and remain on stable trajectories. They are transferred with the beam towards the LHC. The loss signal before and during the rise of the injection kicker magnets shows a 200 MHz modulation which corresponds to the SPS RF-frequency proving that these losses are caused by particles coming from the SPS, see Fig. 35.

The re-capturing process will be discussed in further detail in chapter 7.2.4.

7.1.2 Losses due to mis-steered circulating beam

The second mechanisms is that *circulating* particles which populate the RF-buckets of the LHC outside the beam are deflected by the rising magnetic fields while passing the injection kicker magnets. The majority of these particles are lost on the internal absorber block downstream of the injection kicker magnets, see Fig. 37. The measurements showed that the losses from mis-steered circulating particles are a superposition of un-captured (coasting) particles and *ghost bunches*. Some of the loss signature shows a intensity modulation with a 25 ns period (bunch like structure). These ghost bunches originate from the beam preparation in the PS. The creation process of the ghost bunches will be presented in chapter 7.2.3.

7.2 Proton beam preparation for the LHC

In this section the preparation of LHC proton beams is briefly described. The processes leading to the creation of the longitudinal particle distributions will be discussed.

7.2.1 Initial proton pulse production in the LINAC 2

The initial proton pulse is produced in a duoplasmatron, which ionises the hydrogen gas. In the adjacent radio frequency quadrupole the proton beam is separated into a bunched proton pulse. The pulse is transported into the drift-tube LINAC 2. At the end of the linear accelerator the proton pulse has a length of up to 120 μs and an energy of 50 MeV [3].

7.2.2 Proton Synchrotron Booster

After the linear accelerator the protons are transferred into the Proton Synchrotron Booster (PSB), the first synchrotron accelerator. Due to the low energy of the protons (50 MeV) the particles experience strong space charge effects, which lead to an emittance blowup. To reduce these effects the incoming particle pulse is split into 6 parts, called beamlets. The proton distributor [34] directs the four high intensity parts of the incoming pulse to the four superposed beam pipes of the booster. The beamlets in the separated beam pipes are accelerated up to an energy of 1.4 GeV. After the acceleration process the extraction system recombines the protons to a train of four consecutive beamlets [52]. This process is illustrated in Fig. 38.

7.2.3 Beamlet splitting in the Proton Synchrotron and creation of ghost bunches

When the train of beamlets are injected into the PS the protons have an energy of 1.4 GeV. During the injection the RF-system of the PS is operated at the harmonic number seven. For normal beam preparation six of the seven buckets are filled with beamlets, this requires two injections from the PSB ((4+2) beamlets). The total beam intensity in the filled PS at the injection plateau is about 8.4×10^{12} protons. By changing the frequency of the RF-system the beamlets are split into bunches. At the end of this splitting process the RF-system is operated on harmonic number 84, which corresponds to a frequency of 40 MHz. Each beamlet is split into 12 bunches.

---

[34]The distributor consists of fast rising kicker magnets and septa magnets for distributing the four beamlets into the four rings of the PSB.
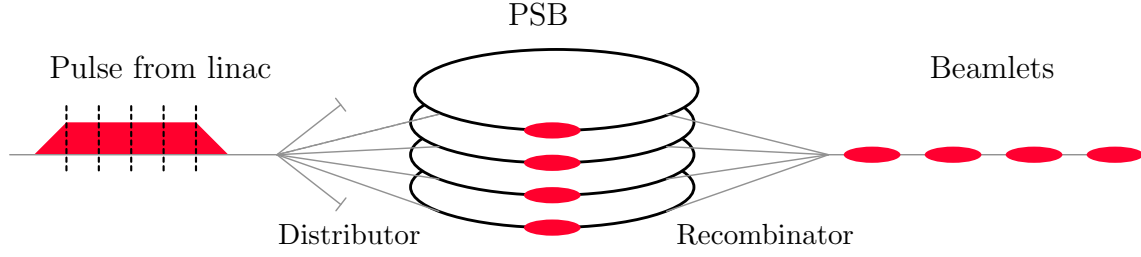
Figure 38: In order to reduce the space charge effects the incoming proton pulse from the LINAC2 is distributed to the four superposed beam pipes of the Proton Synchrotron Booster. The head and tail of the pulse are dumped. After the acceleration the protons are recombined to a consecutive train of maximum four beamlets per PSB cycle.
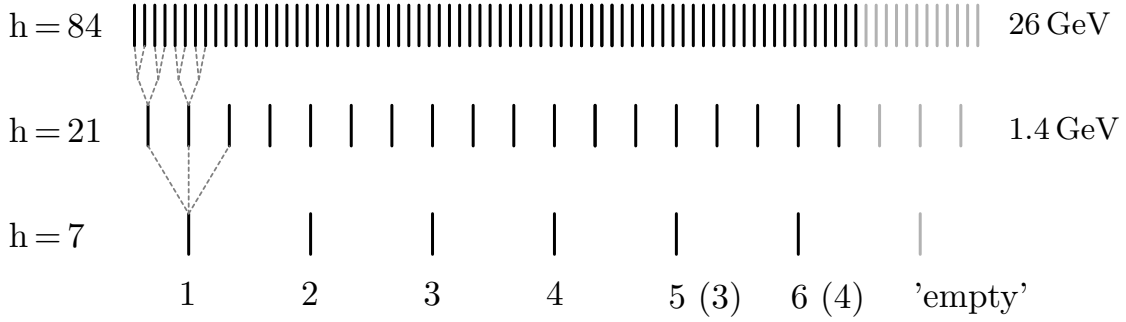

Figure 39: Schematic representation of the splitting of six beamlets from the PSB into a train of 72 bunches. The particle distribution in the initial seventh 'empty' bucket is split accordingly.

In Fig. 39 the splitting of the initial six beamlets is schematically displayed. The resulting bunch train consists of 72 equidistant bunches with a spacing of 25 ns. At the end of the PS cycle the protons have an energy of 26 GeV. In order to shorten the bunches, for fitting them in the 200 MHz SPS RF-structure, the bunches are rotated in the longitudinal phase space[35]. The procedure of the bunch rotation, which is displayed Fig. 40 is executed 300 µs before the beam extraction [3]. To minimise the extraction losses the extraction kickers are synchronised to the part without bunches, the formerly empty seventh bucket.

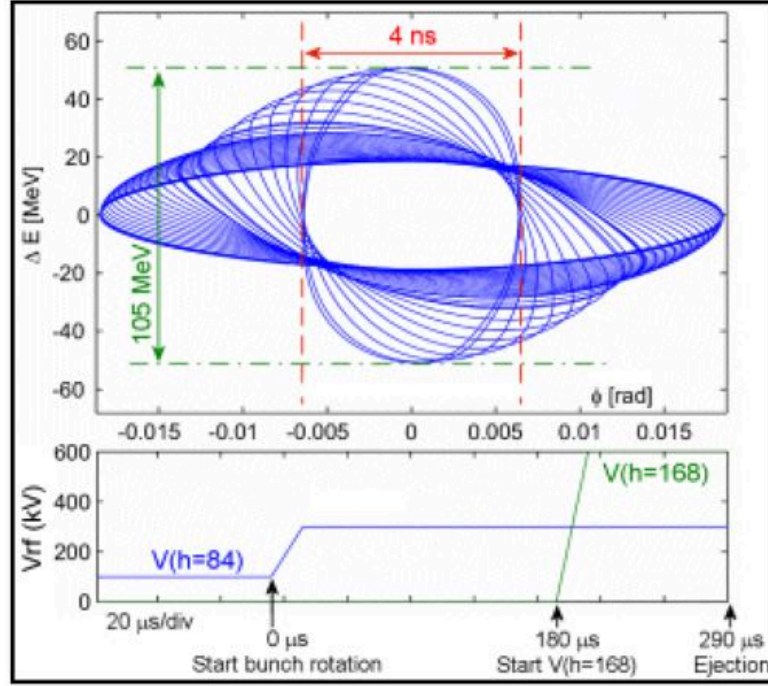[35] For the rotation additional higher order radio frequencies are applied non-adiabatically.

Figure 40: By increasing the RF-voltage and applying an additional higher harmonic (h = 164) the bunch is rotated in its phase space resulting in a shortening of the bunch length so that it fits in the 200 MHz SPS structure [3].

Creation of ghost bunches

Whenever slight mismatch of the transfer optics and the PS optics occurs during injection and due to non linear beam effects during the beamlet splitting, not only the initial six buckets are filled but also the seventh 'empty' bucket is filled with particles, see Fig. 39. The particle intensity in the 'empty bucket' is five to six orders of magnitude smaller than a nominal beamlet, which is in the order of 10^7 protons. These particles are split with the initial beamlets into 'bunches'. At the end of the PS cycle the part with initially no beamlet is populated with particles, which show an intensity distribution with a 25 ns modulation. Since this intensity distribution has bunch-like structure but it is not part of the beam, these 'bunches' are called ghost bunches. The number of ghost bunches depends on the number of 'empty' buckets in the PS. The PS extraction kicker has a rise time of 100 ns. The beginning of the flat top field of the extraction kicker is synchronised to the first nominal bunch of the beam. The flat top time of the kicker is longer than one period of the PS. The ghost bunches are extracted with the nominal beam into the SPS. These particles have the correct time structure and energy for being injected into the stable RF-buckets of the SPS where they are accelerated together with the beam.

7.2.4 Injection into the Super Proton Synchrotron and creation of re-captured beam

The beam with the trailing ghost bunches is injected into the SPS at an energy of 26 GeV. Up to four trains of 72 bunches (25 ns spacing) can be accelerated in the SPS at once. Due to the rise time of the SPS injection kicker magnets of about 200 ns the bunch trains are separated by 200 ns. After the bunch trains are injected the beam is accelerated to an energy of 450 GeV.

Creation of re-captured beam

Whenever there is a mismatch of the transfer line optics and the optics in the SPS a small fraction of the injected bunch train is not captured in the buckets of 200 MHz SPS's RF-structure, see Fig. 41 a). This can occur because of injection errors in phase and energy, or a mismatch between the transfer line optics and the optics of the SPS. These particles coast outside the sparatrix. Particles on unstable trajectories either slip along the bucket structure (positive momentum offset) or overtake the beam (negative momentum offset), Fig. 41 b). To accelerate the beam the voltage program of the SPS's RF-system is changed. During this adjustments the amplitude of the RF-voltage is increased, which leads to an increase of the separatrix acceptance, Fig. 41 c) . Particles on unstable trajectories outside the separatrix are now *re-captured* and continue on stable trajectories, Fig. 41 d). Now the buckets upstream and down stream of the nominal bunches are populated with particles. During the acceleration of the beam the remaining coasting particles are lost in the aperture because the trajectories of the off-momentum particles exceeds the aperture limits [9]. These re-captured particles are accelerated with the beam to the flat top energy of 450 GeV. Recaptured particles are extracted together with the nominal bunches. Measurements of particle intensity distribution in the SPS confirm the existence of un-captured beam at injection plateau, see Fig. 42. Beside the bunch train signals (red), the measurements show two intensity maxima (blue and green), which result from the un-captured particles. The un-captured particles with a positive momentum offset have a longer orbit so they fall behind, green distribution. Un-captured particles with a negative momentum offset have shorter orbit they overtake the captured particles, blue distribution. Consecutive measurements at injection plateau, Fig. 42 a) to e), proved that the two un-capture particle distributions move in opposite directions.

For injections into beam 1 of the LHC the SPS beam is extracted in the SPS' long straight section LSS6 and for injection into beam 2 the beam is extracted in LSS4 of the SPS. At both extraction points fast kicker magnets (MKE) steer the beam into the transfer lines. The flat top length of the extraction kicker magnets was about 10 µs.
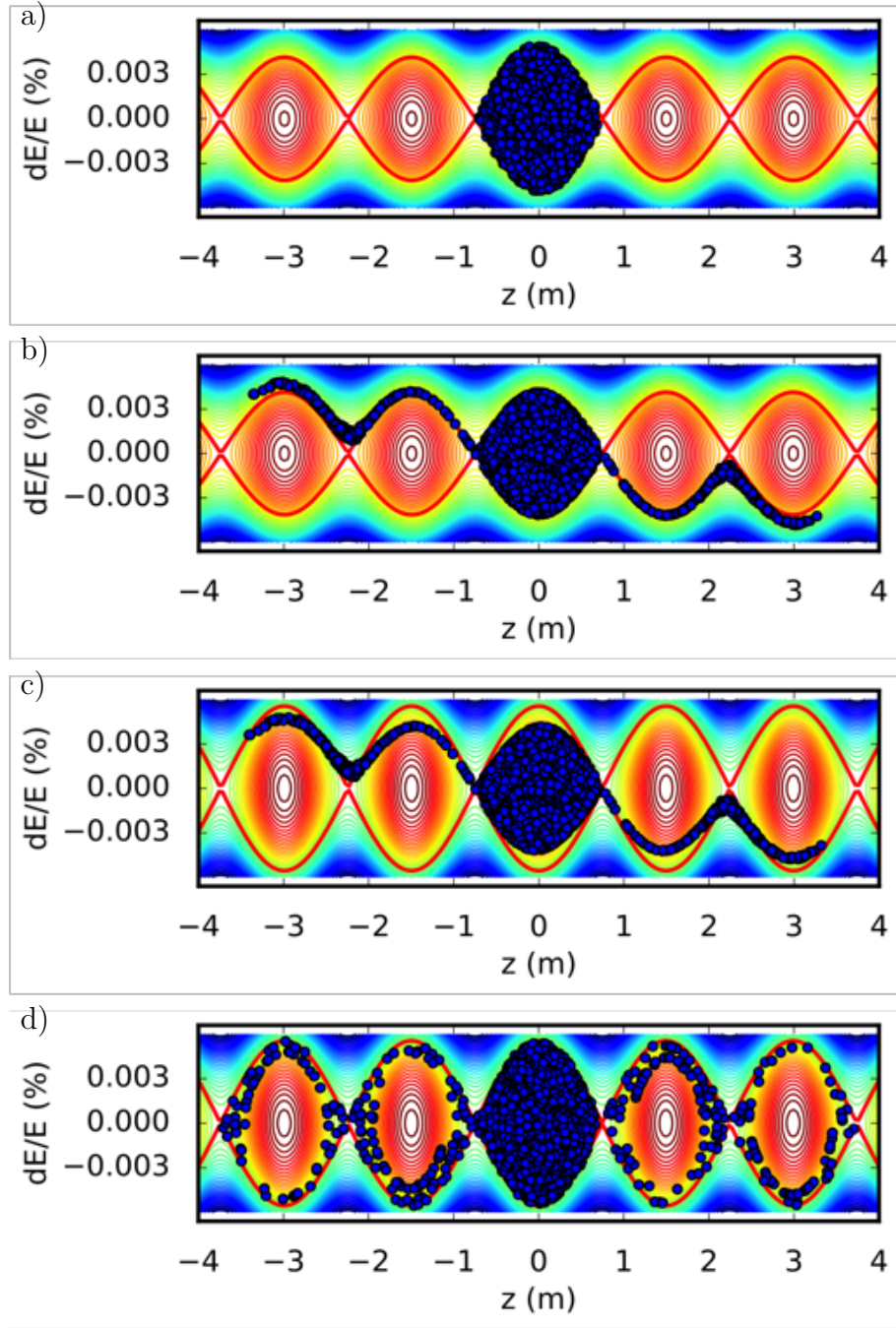
Figure 41: Visualisation of the re-capture process in the SPS over time in the longitudinal phase space. A mismatched bunch (larger than the bucket) is injected (a). Particles outside the separatrix (red) start drifting along the buckets (b). By increasing the RF-voltage the acceptance of the separatrix is increased. Coasting particles are recaptured (c). They stay stable within the initially empty buckets (d) [53].
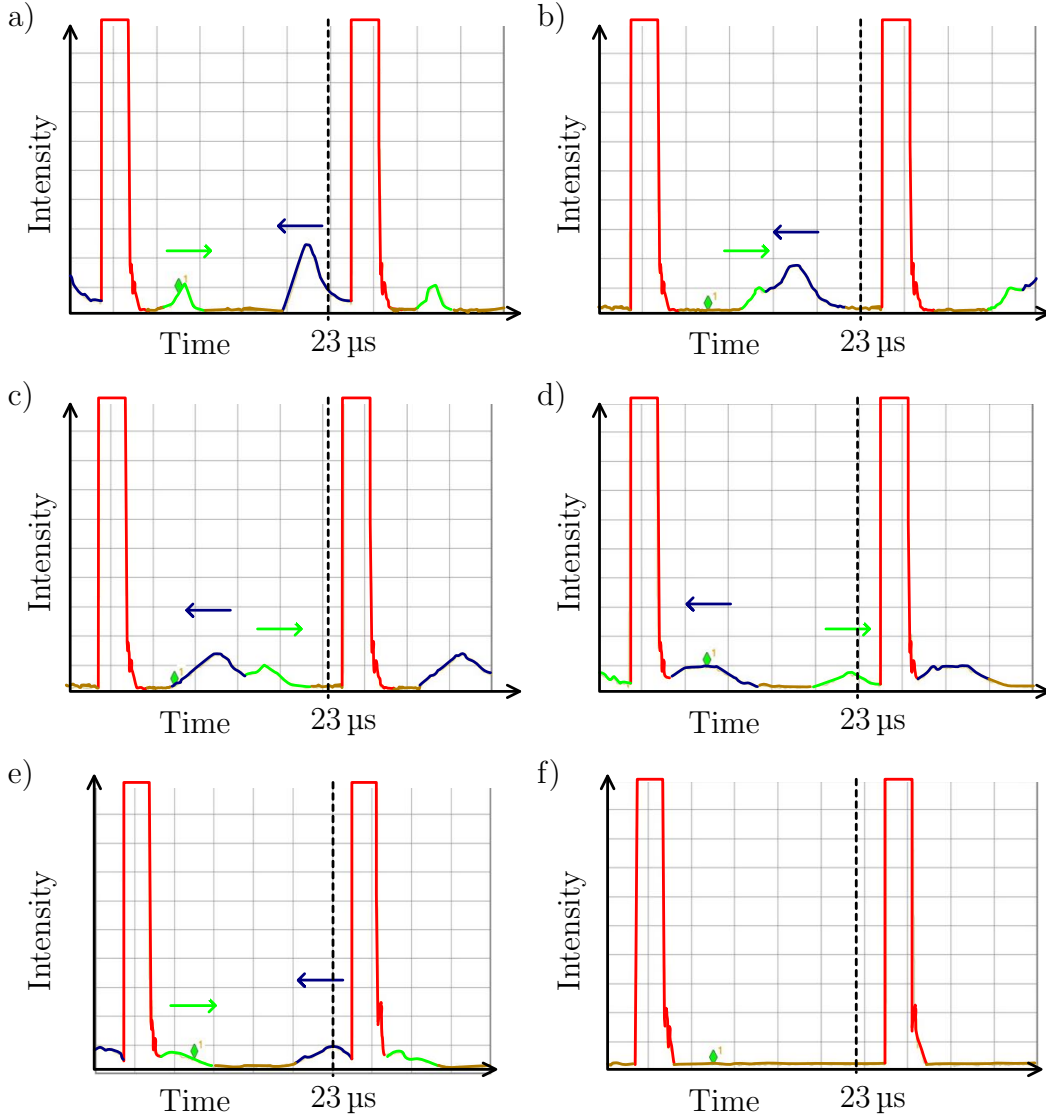
Figure 42: Measurements of the beam intensity in the SPS at different times of the injection plateau a) - e). The revolution period is about 23 µs, one and a half turns of the SPS are displayed. The very high signal (red) originates from the train of the nominal bunches. The two much lower signals correspond to the un-captured particles coasting along the SPS. The distribution of particle with higher energy $E>E_0$, green, have a longer orbit thus they move from left to right. The particles with lower energy $E<E_0$, blue, move from right to left, they have a shorter orbit. The dispersion of the un-captured particles leads to a broadening of the distributions. During the acceleration process the un-captured particles are lost. The re-captured particle intensities are so small that they can not be resolved with these measurements f).

7.2.5 Beam injection into the LHC

In order to protect the aperture of the LHC the transfer lines are equipped with collimators with a nominal opening of $4.5\,\sigma$, which intercept particles with a too large transverse offset from the design trajectory [54], [55]. The transfer line from the Super Proton Synchrotron (SPS) for injections into beam 1 ends 160 m upstream of the interaction point in insertion region two. For injections into beam 2 the transfer line ends 145 m upstream of interaction point in IR 8 respectively. The Figures 43 and 44 show the layout of the LHC injection regions. The trajectory of the injected beam is indicated in red. The incoming beams are horizontally deflected by five injection septa magnets (MSI) so that they approach the LHC from below. The injection kicker magnets[36] (MKIs) steer the beams vertically onto the closed orbit trajectory in the LHC.

Downstream of the injection kickers absorber blocks protect the components in the LHC. Especially the super conducting magnets and further downstream located experiments need to be protected from injection losses. Therefore the internal beam absorber (TDI) consisting of two vertical adjustable jaws is installed 70 m ($\pi/2$ phase advance) downstream of the injection kicker magnets. During the filling process of the LHC at injection plateau the opening of the collimator jaws is $7.5\,\sigma$. The diamond based detector is installed downstream of the absorber block close to the beam pipe, see Figures 43 and 44. If the injection kicker magnets are not triggered for an injection, the incoming beam hits the absorber block with full impact parameter and is then absorbed. Up to 288 bunches at 450 GeV can be directed with full impact parameter, i.e. no deflection by the injection kickers, onto the TDI without damaging the absorber block[37]. If particles pass the injection kickers while the fields are rising the mis-steered bunches are swept over the absorber block. With the changing impact parameter the geometry of the resulting showers changes so that per impinging particles more secondary particles are created downstream of the TDI. In this scenario of the grazing impact, already low particle intensities lost on the TDI can induce quenches in the superconducting magnets. In the worst case, the losses can even damage the jaws of the absorber block. Therefore the intensities of mis-steered particles needs to be kept as low as possible [3], [56], [55].

The beam transfer from the SPS into the LHC is closely monitored. The injection quality check routines analyse the injection and in case of irregularities, e.g. too high beam losses, it can interrupt the filling process of the LHC [56]. The ionisation chamber beam loss monitors in the injection regions provides an important input to the injection loss analysis. The icBLMs close to the diamond based beam loss monitors are used for direct comparison.

---

[36] The injection kicker magnets have a nominal deflection angle of 0.85 mrad.

[37] The resulting particle shower can cause quenches in the superconducting magnets downstream.
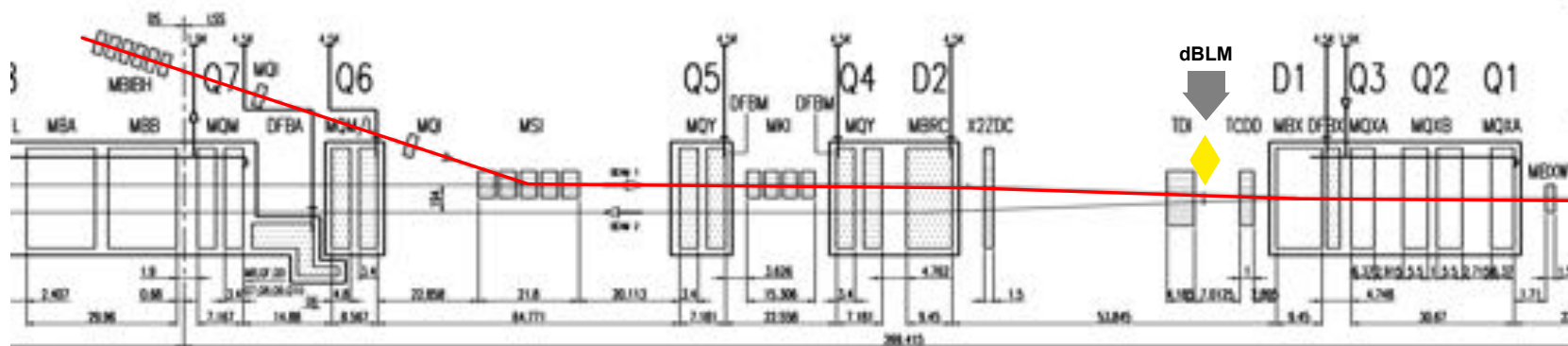
Figure 43: Injection region layout in IR 2 for beam 1. The injected beam is indicated in red. The position of the dBLM downstream of the TDI is marked with a yellow diamond.

Figure 44: Injection region layout in IR 8 for beam 2. The injected beam is indicated in red. The position of the dBLM downstream of the TDI is marked with a yellow diamond.
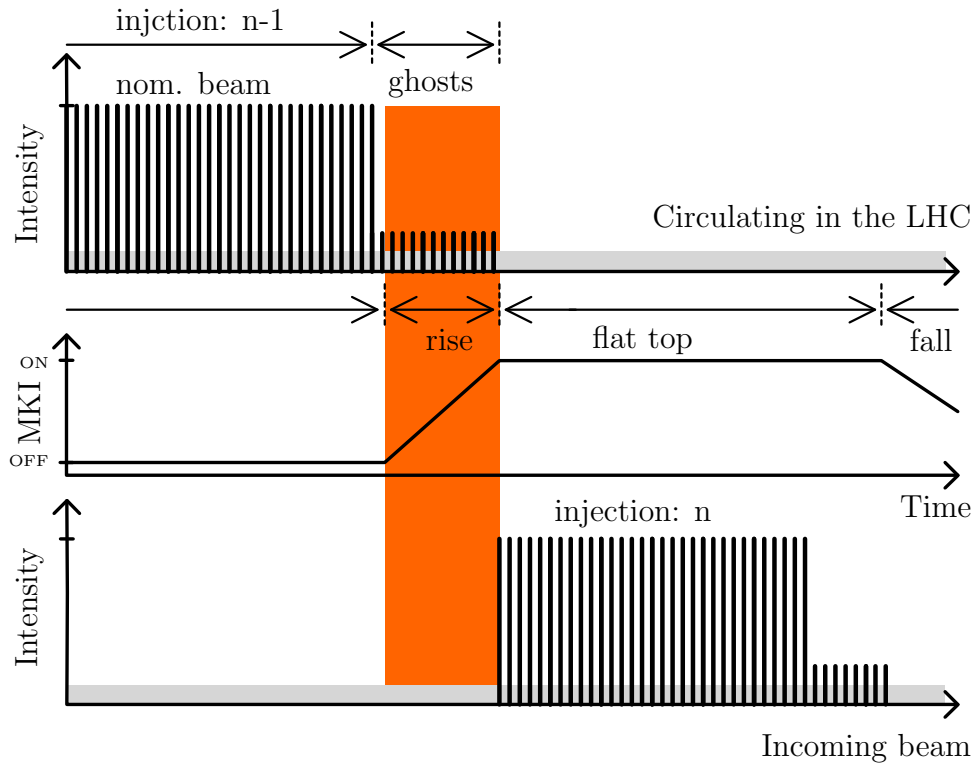
Figure 45: Creation of loss signal with ghost bunch structure. The trailing ghost bunches of the previous injection (n-1) are deflected by the rising fields of the injection kicker magnets for the next injection (n). The deflected particles impact on the absorber block downstream of the injection kicker magnets, the TDI. The dBLM installed downstream of the TDI detects the secondary shower particles.
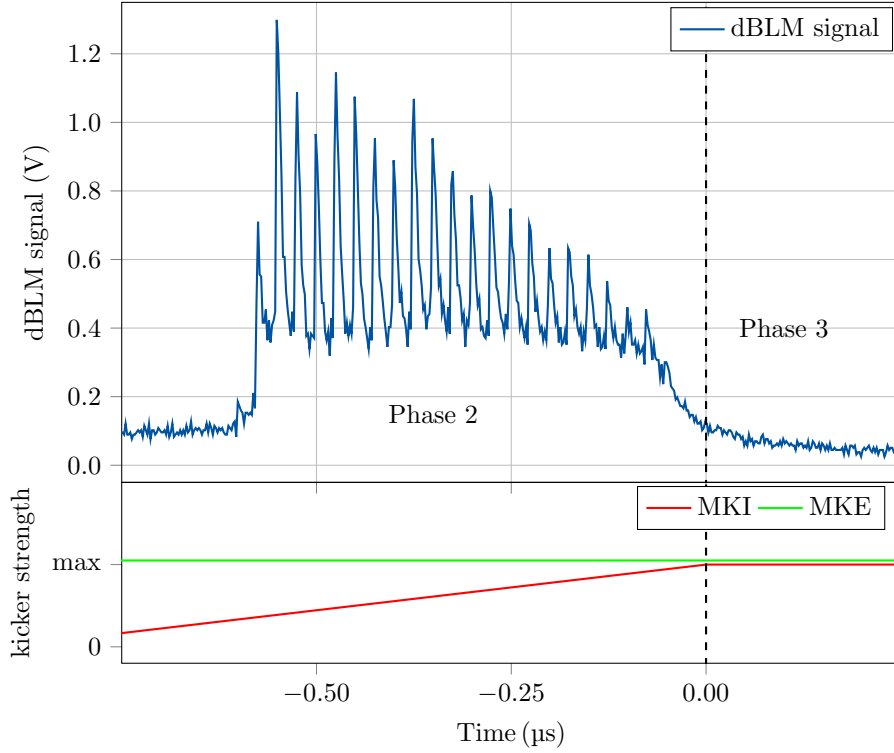
Figure 46: Signals of ghost bunches in phase 2 of the loss signature, the rise time of the injection kickers' fields. The length of the previous bunch train was 36 bunches, which were followed by more than 20 ghost bunches. The loss signal of in phase 2 is a superposition of losses due to recaptured beam and ghost bunches, therefore the signal does not drop completely to the baseline in between the ghost bunches.

The minimum spacing between two consecutive injections, i.e. bunch trains, is $0.9\,\mu s$, the rise time of the injection kicker magnets. Together with the incoming beam the trailing ghost bunches are injected into the LHC. If the next bunch train is placed directly downstream of the previous one leaving only time for the kicker magnets to rise, the trailing ghost bunches are deflected by the rising injection kickers. This will lead to loss signals during the phase two of the injection loss signature, the rise time of the kicker magnets, see Fig. 45. A loss signature with the resulting signals of ghost bunches is displayed in Fig. 46. The number of the ghost bunches depends on the number of empty buckets in the PS during the beam preparation for the previous injection. Whenever the injection kicker magnets are triggered for the next injection and ghost bunches are still passing the kicker magnets the mis-steered ghost bunches will cause the characteristic loss pattern, which is displayed in Fig. 46.

7.3 Calibration of the diamond based particle detectors in the LHC injection regions IR 2 and IR 8

In order to derive the intensities of the particles lost on the internal absorber block during the injection, calibration measurements[38] of the dBLMs in the LHC's injection regions were performed. For these measurements pilot bunches, i.e. bunches with intensities in the order of 1×10^{10} protons, were injected without triggering the injection kicker magnets so that the protons hit the absorber block with full impact parameter. This situation is similar to phase one in the injection loss signature. The pilot-bunch intensities were measured with a beam current transformer in the SPS before they were extracted. These measurements were repeated seven times for both beams. The intensities of the measured pilot bunches were in the range of 0.7×10^{10} up to 2.5×10^{10} protons per pilot bunch. The ratio between detector signal and impacting intensity is 90 nVs/10^9 particles for beam 1 and 100 nVs/10^9 particles for beam 2. The ratios and their variations are listed in Tab. 10. In Fig. 47 the linear regression of the calibration measurements in IR 2 (beam 1) and in IR 8 (beam 2) are shown. The difference in the detector responses can be a result of the different detector efficiencies. Due to the high gradient of the particle shower geometry a slight difference in the detector positions in respect to the absorber blocks can have an additional impact on the signal in the dBLM.

The calibration factor gives the upper limit of the lost particle intensities

With these calibration factors the intensity of the lost particles during an injection can be estimated. As stated above these measurements were performed with particles impacting with full impact parameter on the absorber block. This is the same situation as in phase one of the loss signature when the injection kicker magnets are still off. In the second phase the impact parameter changes, which results in a different geometry of the particles shower. With smaller impact parameters the same amount of particles create larger showers downstream of the absorber block, i.e. the particle to signal ratio changes. By applying the introduced calibration factors for the whole loss signature the total intensity of lost particles can be estimated. Due to the change of the impact parameter and resulting change of the particle to signal ratio the total intensities are over estimated. Thus estimated intensities give an upper limit of the lost particle intensities. Future experiments and simulations of the highly dynamic phase two in the loss signature will give a calibration function, which takes the change of the impact parameter into account.

---

[38]These measurements give the ratio between the number of injected particles and the signal in the dBLM for different intensities. In these measurements the influence of the layout of the injection region is taken into account, which influences the shower geometries and particle intensities impacting on the dBLM.

Table 10: Ratios of the dBLM integral to the beam intensities derived from the dBLM calibration measurements. The errors result from the linear regression

Parameter		Factor
Beam 1		
integral/intensity	$(\text{nVs}/10^9 \text{ particles})$	90 ± 3.8
Beam 2		
integral/intensity	$(\text{nVs}/10^9 \text{ particles})$	100 ± 7.0
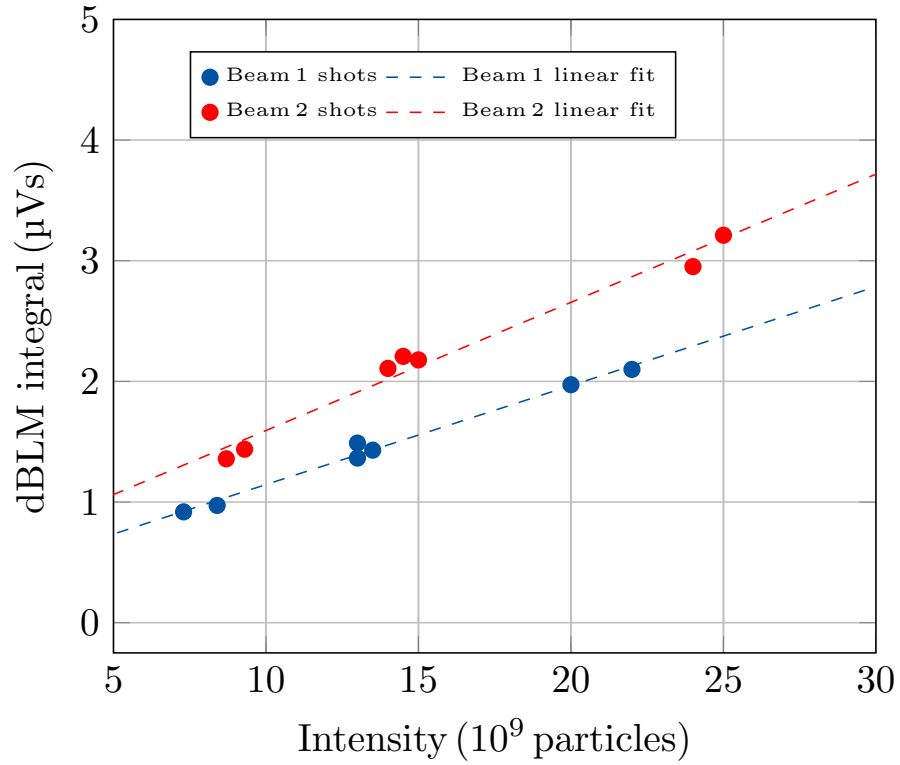
Figure 47: Calibration of the dBLMs in IR 2 (beam 1) and IR 8 (beam 2) with LHC pilot bunches directed on the internal absorber blocks. The linear regression of the dBLM signal over the bunch intensity gives the conversion signal to intensity.

7.4 Injection loss analysis of different injection schemes for filling the LHC

For the injection loss studies the recorded injection loss signatures were combined with the injection information provided by the injection quality check module (IQC). The resulting data sets provide loss signatures with nanosecond resolution from the dBLM and the loss levels recorded by the adjacent icBLMs in the injection regions.

7.4.1 Recorded injection schemes

During the recording phase[39] the standard injection scheme for filling of the LHC was the injection of 144 bunches. This scheme allowed the most compact filling the LHC in 2015 and 2016. The bunch trains in the SPS were composed of two complete fills from the PS (2×72 bunches). In addition for some fills a special configuration of the 144 bunches with 4×36 bunches was used. Shorter bunch trains of 108, 72, 36 and 12 bunches, were injected in order to realise specific filling schemes[40].
The injection scheme of the 108 bunches consists of $(1 \times 72 + 1 \times 36)$ bunches. For creating this scheme one and a half fills of the PS were used. The 72 bunches injection scheme is composed of one complete fill of the PS. For the 36 bunches injection scheme the PS is filled with three beamlets from the PSB, i.e. the PS is only half filled. The injection scheme with the shortest bunch train is the injection of 12 bunches.

7.4.2 Injection schemes showing ghost bunches

As discussed in chapter 7.2.3 the number of ghost bunches depends on the number of initially 'empty' buckets in the PS, i.e. buckets without beamlets. For creating a bunch train of 36 bunches only three of the available six buckets in the PS are filled with beamlets from the PSB. The remaining 'empty' buckets plus the seventh abort gap bucket are populated with low intensities of particles. During the splitting process every beamlet is split into 12 nominal bunches, the low intensities in the 'empty' buckets are split accordingly. This results in a maximum of 48 ghost bunches trailing the 36 nominal bunches. These ghosts cover $1.2\,\mu s$ after the last nominal bunch. If the next injection is placed directly downstream of the previous bunch train the $0.9\,\mu s$ long injection gap is populated with ghost bunches. Injections, which

---

[39] The Injection loss signatures were recorded during October and November 2015.

[40] The structure of the filling scheme, the sequence of bunches in both beams, defines which bunches collide in the centre of the four experiments.

were preceded by an injection scheme ending with train of 36 bunches, as it is for injections of 108 bunches and 36 bunches, tend to show strong ghost bunch signals in phase two of the injection loss signatures.

In Fig. 48 the beginning of the loss signatures of two injections of 144 bunches are displayed. The injection loss signature indicted in blue is preceded by an injection of 72 bunches (one complete fill of the PS). This injection does not show any ghost bunch signals in phase two of the loss signature. The second signature in red shows the loss signal of an injection of 144 bunches, which was preceded by an injection of 36 bunches. The 144 bunches were placed 0.9 µs downstream of the last bunch of the bunch train. The ghost bunch signal in phase two is clearly visible.

The amplitude of the ghost bunches is very sensitive to the settings in the pre-accelerators. Especially the initial particle distribution in the PS strongly influences intensity of the ghost bunches. The amplitude of the signals varies between 0.2 V and 1.0 V. The integral of the second phase of loss signatures with ghost bunches and without ghost bunches are in the same order.

7.4.3 Losses during the fall time of the injection kicker magnets due to trailing re-captured beam

The flat top length of the injection kicker magnets was set to 5.1 µs during the measurements. With a fixed flat top length, the time between the last bunch and the end of the flat top time depends on the length of the bunch train. The intensity of re-captured particles downstream of the beam from the SPS decreases with the distance to the bunch train, which is schematically shown in Fig. 49. For injections of 144 bunches the loss signatures show an additional loss signal during phase four, the fall time of the injection kicker magnets, see Fig. 50. These losses are caused by re-captured particles trailing the injected bunch train. The additional losses in phase four make up to 60% of the total losses recorded for injections of 144 bunches. A bunch train of 144 bunches has a length of 3.8 µs, 144×25 ns+200 ns gap between the two trains of 72 bunches from the PS. The intensity of the re-captured particles downstream of the 144 bunches at the beginning of the injection kicker fall time is still high enough to create a significant loss signal. This gives a minimum length of the trailing particle intensities downstream of the bunch train of 1.3 µs. For injections of 108 bunches, the second longest injection scheme (108×25 ns+200 ns gap = 2.9 µs), no significant losses during the fourth phase were observed, see Fig. 50. This means that the intensity of the re-captured beam decreases within 2.2 µs[41] below the detection limit.

---

[41] With 5.1 µs injection kicker flat top length - 2.9 µs duration of the train of 108 bunches the resulting time between the last bunch and the end of the flat top time is 2.2 µs.
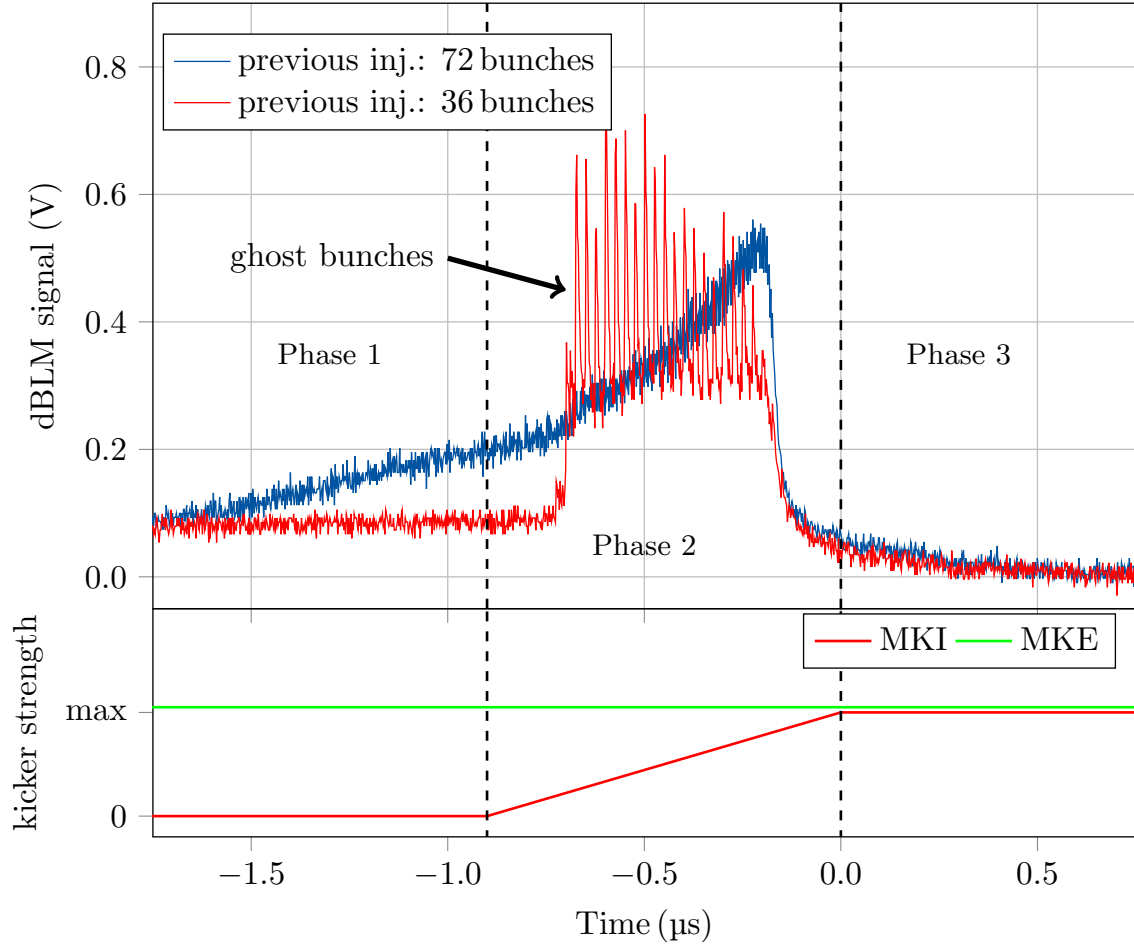
Figure 48: Injection losses of two injections with injected 144 bunches. For the injection, which is preceded by an injection of 72 bunches, blue, no ghost bunches were detected. In the loss signature of the injection, which was preceded by an injection of 36 bunches, red, the ghost bunches were clearly visible. The vertical lines separate the different phases of the injection loss signatures. In the plot below the status of the SPS extraction kicker and the LHC injection kickers are displayed.
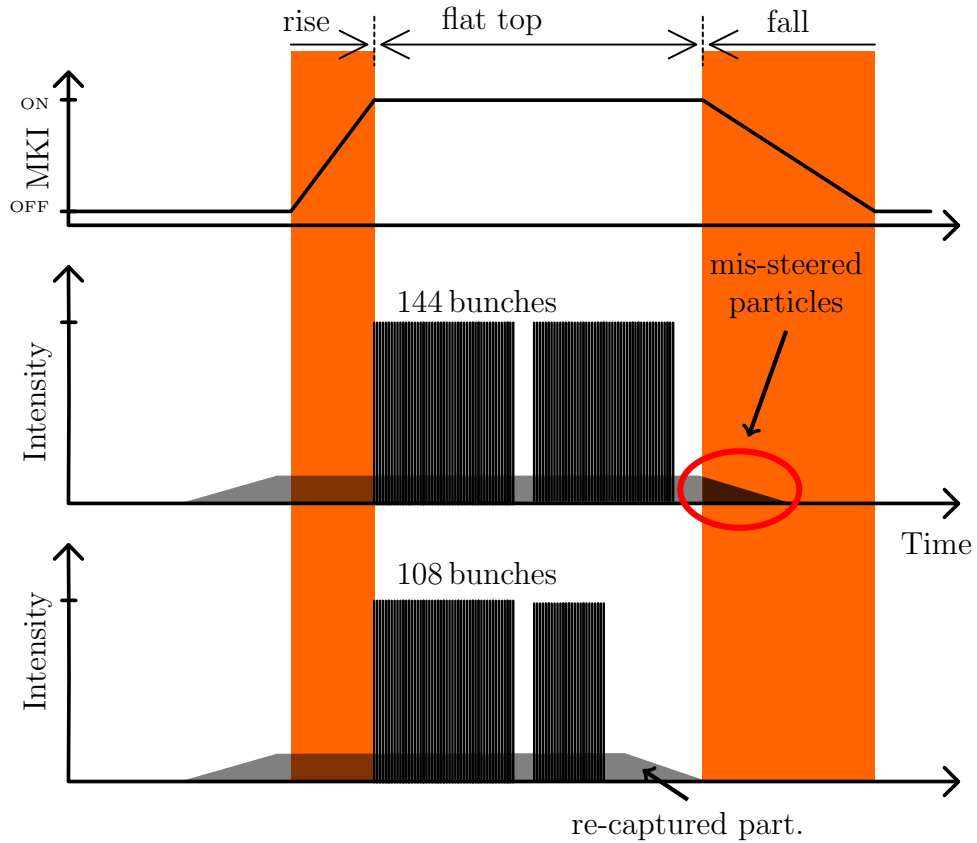
Figure 49: Schematic representation of the SPS beam and its re-captured beam intensity distribution. The re-captured particle intensity depends on the distance to the last bunch of the injected bunch train. With a fixed flat top length of the injection kicker magnets the time between the last nominal bunch and the beginning of the injection kickers' fall time depends on the bunch train length. For injections with 144 bunches the recaptured beam intensity during the MKI fall time is high enough to create high losses during this phase. For injections of 108 bunches the trailing particle intensity is too low to create a signal.
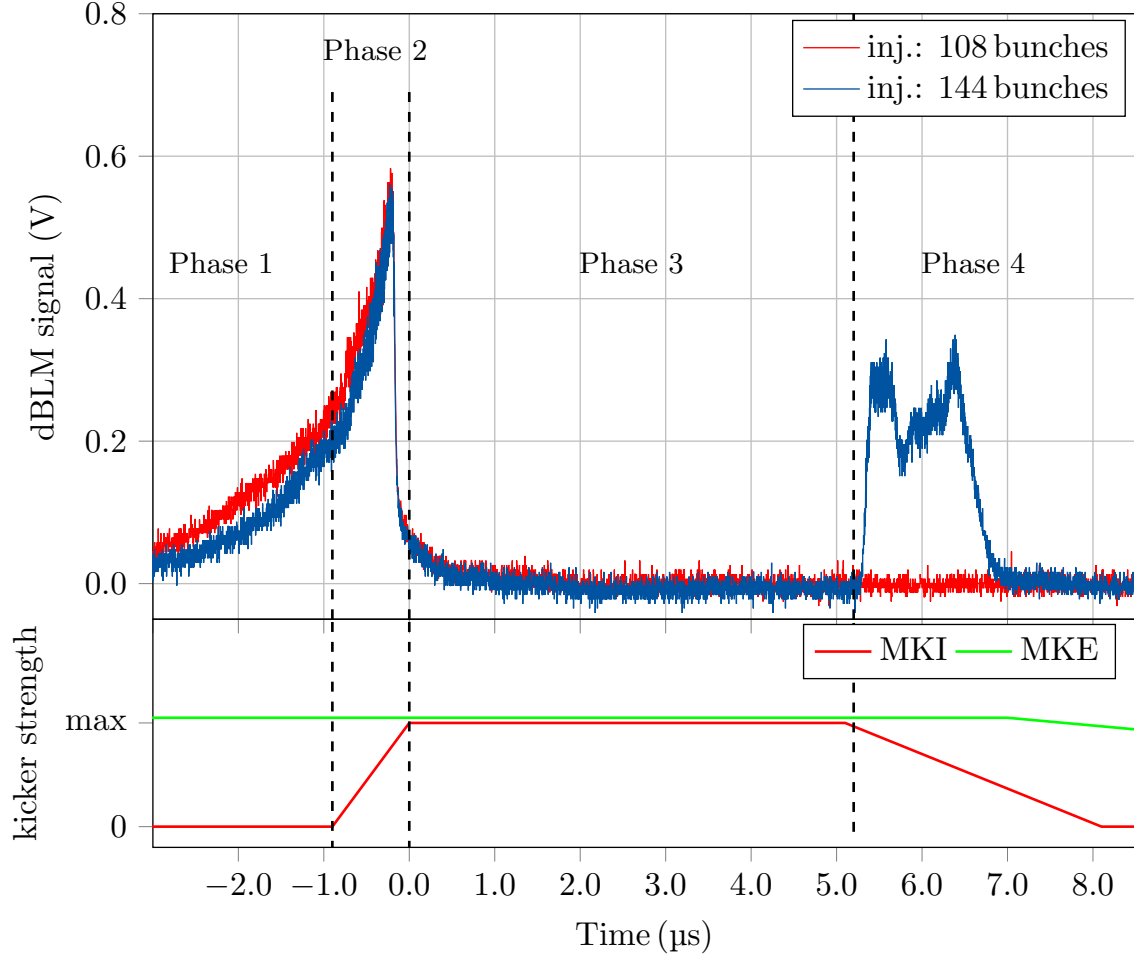
Figure 50: Loss signatures of injections of 108 bunches and 144 bunches. The injection of 144 bunches shows an additional loss signal during the fall time of the MKI (phase four). Re-captured particles downstream of the bunch train are swept back over the TDI. The intensity of the recaptured beam depend on the distance to the last bunch of the injected bunch train. For injections with shorter bunch trains, e.g. 108 bunches, the re-captured beam intensity has fallen below the detection limit.
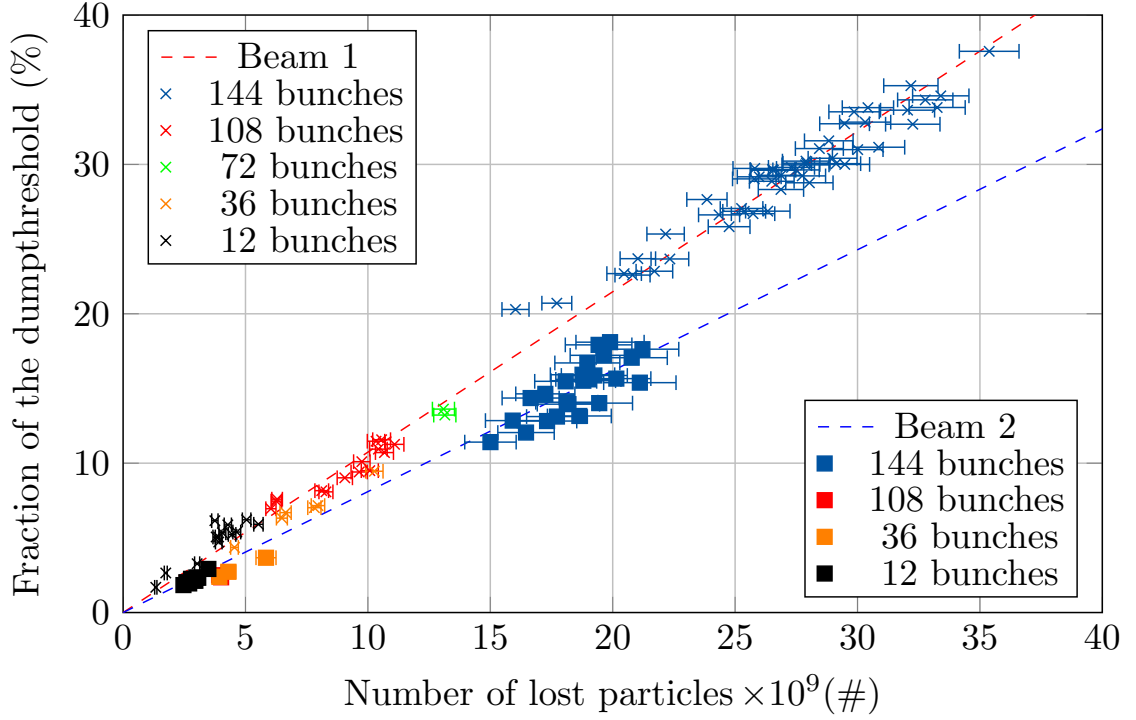
Figure 51: Fraction of dump threshold over the number of lost particles for beam 1 and beam 2 injections. The number of lost particles were calculated from the dBLM measurements by applying the conversion factors given in Tab. 10. A linear trend is clearly visible.

7.4.4 Lost particles intensities on the internal absorber block during injection

Figure 51 shows the fraction of dump threshold over the particle intensities lost on the internal absorber block. The lost particles intensities were calculated from the integrals of the dBLM signals by applying the conversion factors, which were introduced in chapter 7.1. The fraction of dump threshold was retrieved from the injection quality check module for every injection loss signature. Loss signatures were recorded for 12, 36, 72 (only beam 1), 108 and 144 bunches injected into beam 1 and beam 2 of the LHC. The intensities of the lost particles for injections into beam 1 vary between 2×10^9 protons for injections of 12 bunches and 35.1×10^9 protons for injections of 144 bunches. The maximum lost intensity compares to 7 LHC pilot bunches or 33% of a nominal bunch. The losses in IR 8 for injections of beam 2 are almost a factor two lower compared to beam 1 but the losses still reach 22×10^9 protons which is equivalent to 4 LHC pilot bunches.

The loss intensities for the same injection scheme differ between the two injection regions in IR 2 and IR 8. The losses in IR 8 are at least 35% lower than in IR 2. But the general shape of the loss signature is the same. The results of the detailed

analysis of the loss contribution of every phase and injection scheme for beam 1 and beam 2 are listed in Tab. 11. Injections with one complete fill from the PS, 72, 108 and 144 bunches, show comparable losses in phase 1 and phase 2 of the loss signatures. For shorter trains with no complete fill of the PS, 36 and 12 bunches, the loss amplitudes are lower in this phase. The losses depend on the intensity of the first bunch train from the PS injected into the SPS where the bunch trains are composed for injections into the LHC. The amplitude in phase two varies strongly between the injections. Circulating particles and ghost bunches from the previous injection into the LHC are mis-steered by the rising fields of the injection kickers. At the same time the incoming particles are swept over the absorber block with a decreasing impact parameter. The intensities of these losses are very sensitive to the machine setup.

The lost particle intensities of injections showing ghost bunches are not significantly higher than the intensities for injections without ghost bunches. Therefore the two loss signatures, with and without ghost bunch signals, are not distinct.

In phase three the loss amplitude is relatively low, the contribution to the total loss signature is less than 5%, which means almost no transversal[42] losses were observed on the absorber blocks in IR 2 and IR 8. As mentioned before, only injection scheme with 144 injected bunches shows a significant loss amplitude in the fourth phase. For this injection scheme the losses in phase four make up to 60% of the total loss signature.

The average loss intensities and the standard deviations per injection scheme are listed in Tab. 11. The measurement setup is very sensitive to slight variations in the settings of the pre-accelerator chain. Therefore small fluctuations in the beam preparation cause a relatively wide data spread.

---

[42] Transversal losses are caused by particles with a too large deviation from the design trajectory. These particles are normally intercepted by the collimators in the transfer lines.

Table 11: Average upper limit of particle intensities lost during injections of beam 1 and beam 2. The intensities are given for the four phases of the injection loss signature and the sum, the total of the lost intensities. The conversion factors of $90\,\mathrm{nV}/10^9$ particles for beam 1 and $100\,\mathrm{nV}/10^9$ particles for beam 2 were applied

Beam	Nr. of inj.	Inj. bunches	Phase 1 (10^9 p)		Phase 2 (10^9 p)		Phase 3 (10^9 p)		Phase 4 (10^9 p)		Total (10^9 p)	
			μ	σ	μ	σ	μ	σ	μ	σ	μ	σ
1	80	**144**	4.4	0.83	5.5	2.1	0.3	0.20	14.1	5.14	24.3	5.3
1	16	**108**	4.4	0.57	3.5	1.15	0.19	0.19	0.0	0.11	8.1	1.5
1	2	**72**	4.3	1.3	7.0	1.3	0.55	0.015	0.0	0.01	11.8	0.03
1	14	**36**	1.8	0.58	4.2	1.6	0.45	0.20	0.0	0.01	6.55	1.7
1	10	**12**	1.3	0.41	1.2	0.33	0.0	0.13	0.8	0.5	3.4	1.0
2	32	**144**	1.4	0.27	3.5	1.3	0.3	0.13	13.3	1.26	18.6	1.6
2	2	**108**	1.19	0.076	2.59	0.01	0.20	0.06	0.0	0.06	3.96	0.058
2	0	**72**										
2	4	**36**	0.5	0.12	3.9	0.7	0.34	0.21	0.0	0.06	4.7	1.0
2	12	**12**	0.43	0.04	1.4	0.18	0.1	0.05	0.84	0.095	.8	0.28

Discussion of the injection loss measurements and implications for future injection schemes with 288 bunches

The measurements show that the injection losses in IR 8 are at least 25% lower than the losses in IR 2. This can be caused by two effects. The shower intensities caused by particles impacting on the internal absorber block (TDI) are very sensitive to changes in the geometry and the detector positioning. Here for instance the positions of the internal absorber jaws have a strong influence on the signal amplitude. For getting a better understanding of the evolution of the particle showers in dependency of the jaw position detailed FLUKA studies are needed.

The other effect, which can explain the difference between the two injection regions is that the detector charge collection efficiencies of LHC type dBLM differ up to 20% from detector to detector, see chapter 5. The installation of characterised dBLMs would allow to take the different detector efficiencies into account for the injection loss analysis.

The measurements of the different injection schemes have shown that with the increase of the bunch train length the loss amplitudes increase. Especially for the injection scheme with 144 bunches where the trailing re-captured particle intensities are still high enough to cause high loss signals during the fall time of the injection kicker magnets. In order to increase the luminosity in the next years of the LHC a higher number of bunches per beam is needed (maximum 2808 bunches). That means that the filling scheme needs to be more dense. The SPS can provide a maximum of 288 bunches per cycle, which is the maximum number of bunches per injection into the LHC. The bunch train consists of four full fills of the PS, i.e. four times 72 bunches plus the PS abort gaps. The length of the resulting trains 7.8 μs ($4 \times 72 \times 25 + 3 \times 200\,\text{ns} = 7800\,\text{ns}$). The length of these bunch trains is very close to the maximum flat top length of the injection kicker magnets, which is 7.9 μs. As discussed before the particles downstream of the bunch train will be deflected by the falling kicker magnets fields after the flat top time. The particle intensities decreases with distance to the bunch train. Hence the intensity close to the last bunches of the train is higher than the intensity, which caused the losses during the injection of the 144 bunch injection scheme. Since the time between last bunch of the injection scheme with 144 bunches and the start of the fall of the injection kicker magnets was about 1 μs due to the fixed flat top length of 5.1 μs. For 288 bunch injections a very high loss signal during the fall time of the injection kicker magnets can be expected because for this scheme the time between the last bunch and the start of the fall of the injection kicker fields, is about 0.1 μs. There are two possibilities to avoid these high losses during the phase four of the injection loss signature, the fall time of the injection kicker magnets. The first one is to increase the maximum flat top time of the injection kickers. This would increase the time between the last bunch and the start of the fall of the kicker fields. In order to realise this solution the hardware of the kicker system needs to be modified. The second approach to reduce the losses

due to trailing particles, which pass the falling kicker fields is to reduce the intensity of the recaptured particles downstream of the bunch train. The assessment of the expected high losses during phase four of the injection loss signature for injections of 288 bunches underlines the need for reducing the re-captured particle intensities in the SPS.

7.4.5 Injection losses at the primary collimators in IR 7

The primary collimators (TCPs) in IR 7 of the LHC form the aperture bottleneck. Particles with too large offsets from the closed orbit, i.e. too large betatron amplitudes, will impact on the primary collimators, the resulting showers are attenuated by the downstream secondary and tertiary collimators. In order to measure the losses at the collimators dBLMs are installed close to the beam line 10 m downstream of the primary collimators.

Due to a slight mismatch of the transfer line and LHC optics, the bunch train is injected with a small offset from the design orbit. This results in injection oscillation of the bunch train around the design orbit, which leads to losses on the primary collimators[43]. Figure 52 shows the superposition of the two loss signatures, which were recorded in IR 2 (blue) and in IR 7 (red), during an injection of 144 bunches. For this injection the injected beam was composed of four bunch trains, each consisting of 36 bunches. In order to show both loss signatures in one plot the signal recorded close to the primary collimators in IR 7 is time corrected by 58 µs, the time it takes the bunch train to travel from IR 2 to IR 7. The displayed loss signal, which was recorded in IR 7, is amplified by a factor 100 (40 dB) so the four trains of the 36 consecutive bunches are clearly visible allowing the identification of the first bunch of the train. The beginning of the first bunch train shows a higher signal compared to the other three bunch trains. This effect is caused by the rising fields of the injection kicker magnets. When the fields reach 85% of their deflection angle, the deflection is large enough to inject the incoming particles into the LHC. These particles are not absorbed by the internal absorber block (TDI) in the injection region anymore. Due to the incorrect deflection angle, 85% instead of 100%, these particles perform larger injection oscillations than particles, which are injected with the nominal deflection angle of the injection kicker magnets.

At the end of the loss signature recorded in IR 7 an additional steep loss signal is visible. This loss signal origins from the recaptured particles downstream of the nominal bunch train. When the fields of the injection kickers fall after the flat top time the deflection angle is in the beginning still larger than 85% so the incoming particles still pass the internal absorber block. Due to the smaller deflection angle of the kicker magnets these particles perform large injection oscillations which results in large losses on the collimators in IR 7. This is the same effect, which causes

---

[43]This oscillations are damped by the LHC's transverse damper system (ADT) [57].
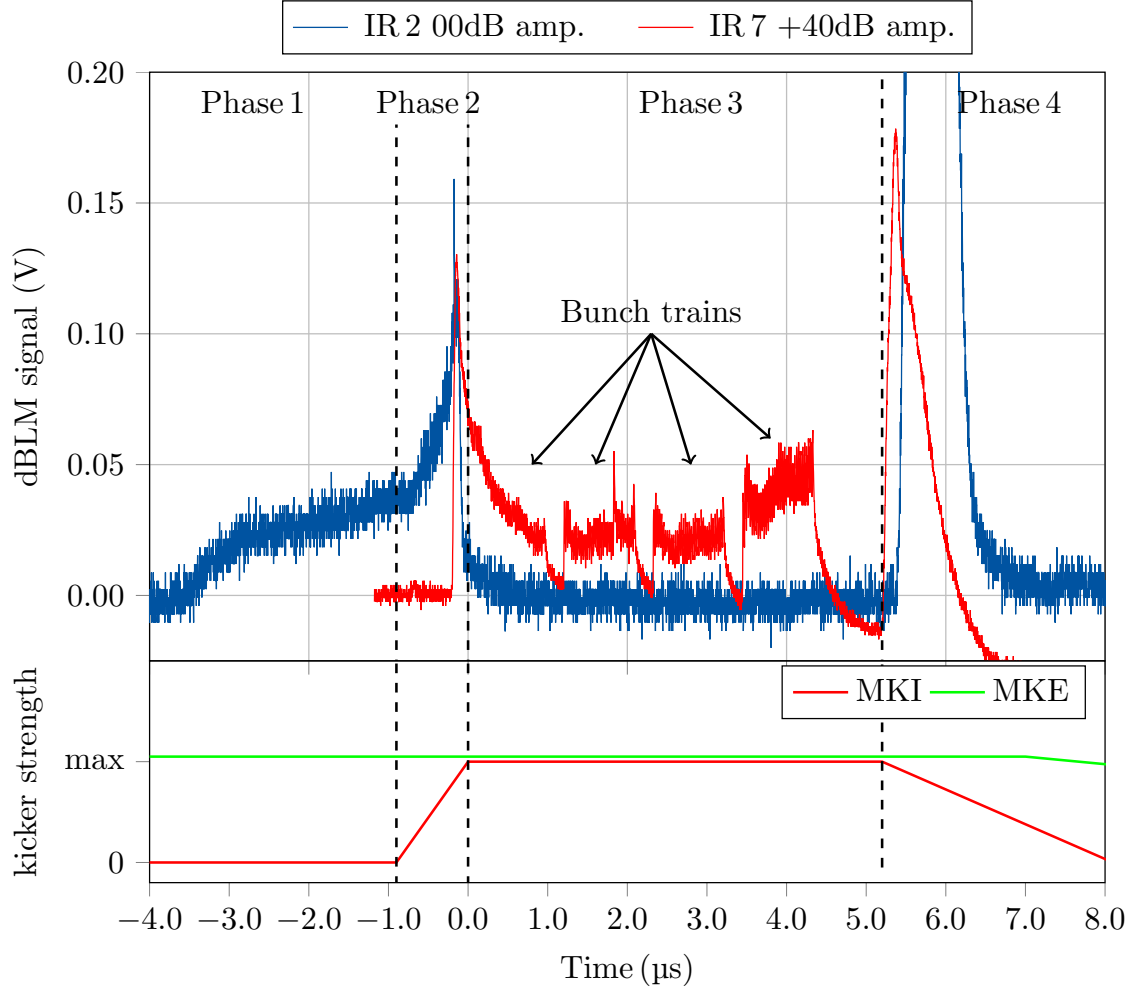
Figure 52: Superposition of injection loss signatures of an injection of 144 bunches, 4×36 bunches, which were recorded in the injection region in IR 2 and close to the primary collimators in IR 7. The four phases of the loss signature are indicted. The transverse losses in IR 7 show clearly the four bunch trains. When the injection kicker fields have reached more than 85% of their nominal field strength, the passing particles are injected into the LHC. However, the injected particles are mis-steered due to the small deflection angle. The injection kickers just reach their nominal field strength when the first bunch of the beam passes the kickers. The high signal at the end is caused by the falling kicker fields, the particles are still injected but due to the decreasing deflection angle they perform large oscillations around the closed orbit. If the deflection angle is less than 85%, the particles are lost on the internal absorber block (TDI) in the injection region.

the high loss signals in the beginning of the bunch train. If the deflection angle of the injection kicker magnets is smaller than 85% the particles are absorbed by the internal absorber in the injection region. This results in a cut off of the loss signal in IR 7.

The time between the first bunch of the injected train and the beginning of the loss caused by the falling fields of the injection kickers on the primary collimators is 5.1 μs, which matches with the 5.1 μs flat top time of the injection kicker magnets. Figure 53 shows a zoom into the beginning of the time corrected loss signatures of the measurements in IR 2 and IR 7. The transition from losses due to recaptured particles to transverse losses from the nominal bunches at $t = 0.25$ μs is clearly visible. An additional loss signal is visible at about -0.5 μs. These losses are created by mis-steered circulating particles. At the beginning of the rise time of the injection kickers the deflection angle is not large enough to steer the circulating particles onto the internal absorber block in the injection region. These mis-steered particles perform oscillations around the design orbit. Due to their large oscillation amplitude the particles are lost on the primary collimators in IR 7.

7.5 Mitigation of the injection losses

In the previous sections the injection losses and their underlying mechanisms have been discussed. The presented measurements have shown the impact of the injection scheme, i.e. the length of the bunch trains and their composition on the injection losses. Based on a better understanding of the loss mechanisms mitigation techniques for reducing these losses were developed and implemented into the LHC operation routines. In the following sections different approaches for reducing the injection losses in the injection regions of the LHC will be discussed.

7.5.1 Introduction of 'empty' injection magnets kicks

A simple method to reduce the loss amplitude during an injection is the introduction of 'empty' kicks. This means that the injection kicker magnets are triggered without transferring beam from the SPS to the LHC. During the rise, flat top and fall time of the injection kickers, the particles populating the injection slot are steered onto the internal absorber block (TDI). Due to the cleaning of the injection slot the intensity of circulating particles is reduced. A short time after this procedure the injection with beam is triggered. This does not reduce the total losses but distributes the losses over time. This technique is frequently used by the LHC operators.
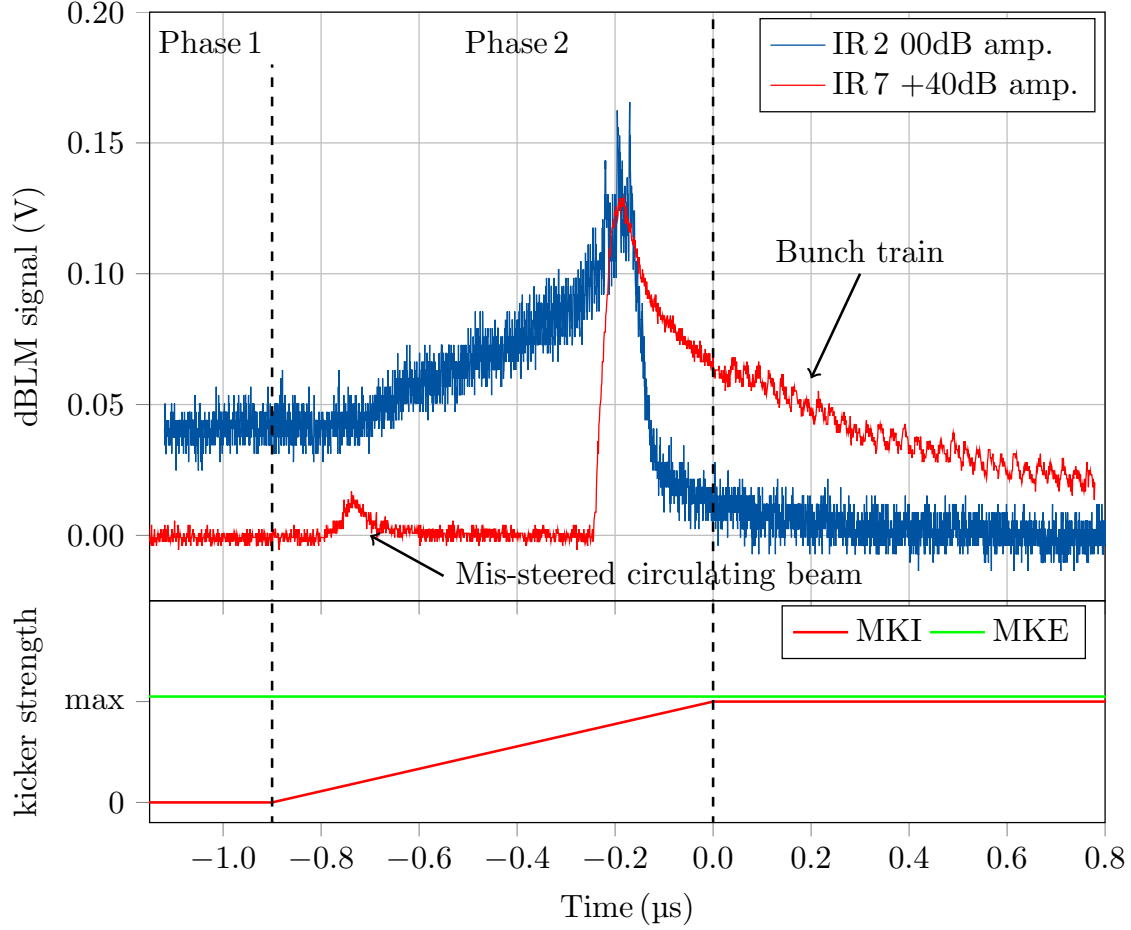
Figure 53: Zoom into the beginning of the loss signatures, which are displayed in Fig. 52. In the loss signature, which was recorded in IR 7, the transition of losses from re-captured particles to transverse losses of the injected bunch train is clearly visible. In the beginning of the injection kicker rise time the deflection angel is not large enough to steer passing circulating particles onto the absorber block in the injection region. These particles continue on their trajectory performing large oscillations around the closed orbit until they are lost on the primary collimators in IR 7. The resulting loss signal is visible at -0.75 μs.

7.5.2 Cleaning the injection gap with the LHC's transverse damper system

The LHC is equipped with a fast gated transverse magnet system (ADT). This system is used for damping the injection oscillations of the injected beam by applying counteracting kicks when the injected bunch train passes. The system can be used in the opposite manner, it can be used for increasing the particle oscillation. If the particle's amplitude exceeds the collimator limits they are lost on the collimators in IR 7. This can be used for 'cleaning' the beam from unwanted particles [57]. Up to now the transverse damper system is gated to the part where the next bunch train will be injected. The gate of the cleaning system can be extended for cleaning the part synchronised to the injection kicker rise time. This would reduce the losses due to mis-steered circulating particles. Cleaning the beam close to the bunch train upstream of the injection slot could lead to an unwanted excitation of the last bunches of the train. Studies on bringing the 'cleaning' window closer to the upstream bunch train are ongoing. The advantage of this procedure compared with the 'empty' kick method is that the local particle losses in the injection regions are reduced since the particles with large betatron amplitudes are lost on the collimators in IR 7.

7.5.3 Reducing the losses during the fall time of the kicker magnets by increasing the injection kicker flat top length

As shown in chapter 7.4.4 the loss signature of an injection of 144 bunches is dominated by losses during the fall time of the injection kickers (phase four). The intensities downstream of the bunch train decrease with the distance to the bunches. Therefore a lengthening of the flat top time for injections of 144 bunches leads to a reduction of the losses during the injection kicker fall time. In Fig. 54 two injections with 144 bunches are shown. The first one had the nominal flat top length of 5.1 μs. For the second injection the flat top length was increased by 1 μs to 6.1 μs. In the first loss signature the second loss signal in phase four is clearly visible. This signal vanishes completely when the flat top time is increased by 1 μs. With the increased flat top time the time between the last bunch of the train of 144 bunches and the end of the flat top is 2.3 μs. This time is comparable with the time for the injection scheme of 108 bunches, where the time between the last bunch and the start of the kicker fall time was 2.2 μs long, see chapter 7.4.4. For this scheme no additional losses in phase four were observed. With the increase of the flat top time the losses during an injection of 144 bunches is reduced by 60%. The particles which caused the losses during injections with short injection kicker flat top times are now injected with the nominal bunch train into the LHC. These particles populate the LHC downstream of the injected bunch train, which is a possible slot for the next injection. If the injection slot is not cleaned, these particles will contribute to the

loss signature of the following injection. An increase of the flat top length of the injection kicker magnets is only a solution for reducing the injection losses if it is accompanied by either a cleaning of the injection slot or an 'empty' kick before the next injection.
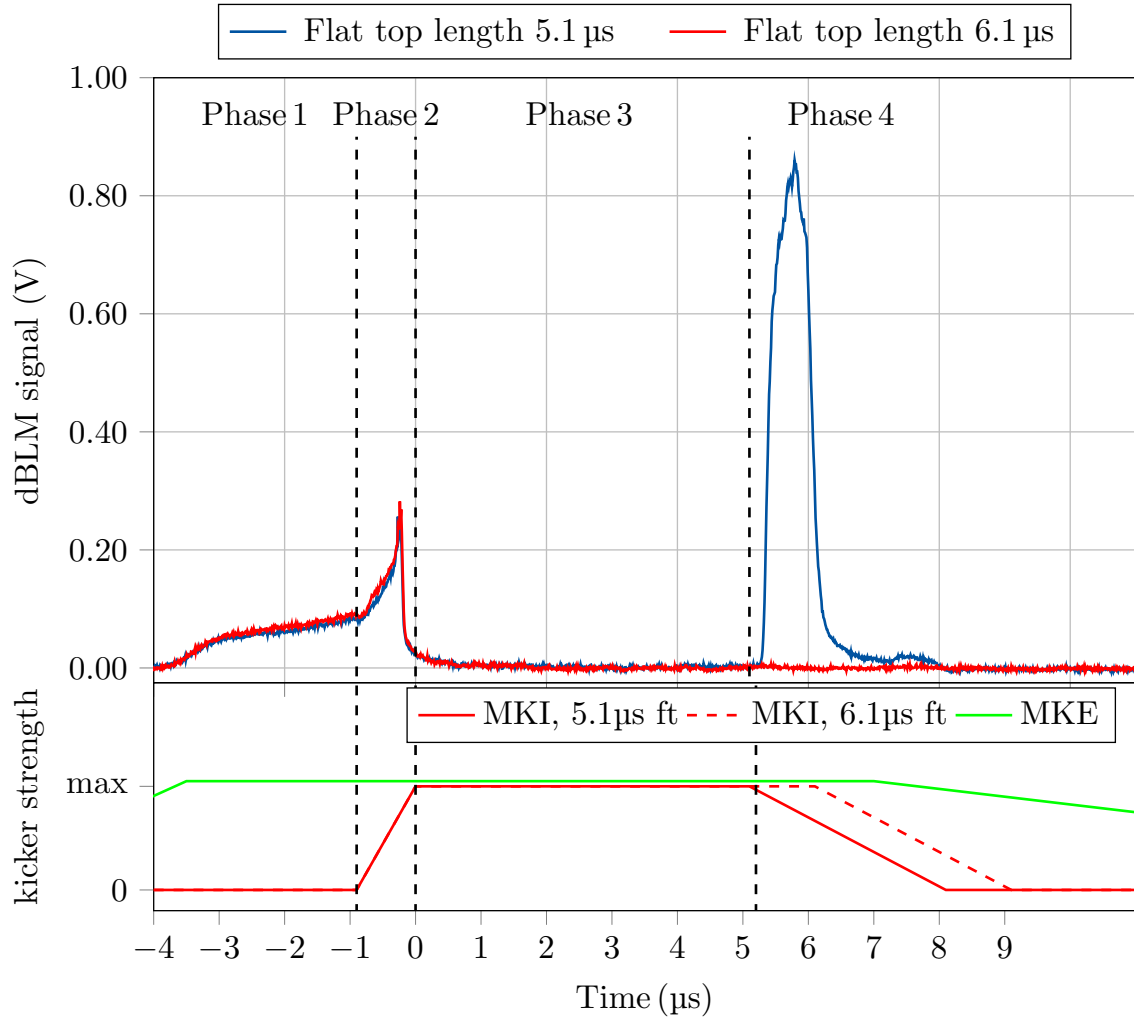

Figure 54: Injections of 144 bunches, the first injection with nominal injection kicker flat top length of 5.1 μs. For the second injection the kicker flat top length was increased by 1 μs to 6.1 μs total flat top length. The second loss signal in phase four vanishes completely when the flat top length was increased.

7.5.4 Using the SPS tune kicker magnets for reducing the intensities of re-captured particles in the SPS

A more promising approach to reduce the injection losses is to reduce the re-captured particle intensities *before* these particles are injected into the LHC. As discussed the coasting particles in the SPS are re-captured at the end of the injection plateau at $26\,\text{GeV}$, see chapter 7.2.4. The SPS is equipped with a fast gated transverse kicker magnet system (MKQ), which is originally used for tune measurements. This system is comparable with the transverse damper system in the LHC. By gating the transverse kickers in the SPS to the part where the re-captured particles populate the buckets, the magnets can be use for cleaning the SPS beam at injection plateau, reducing the losses of high energetic ($450\,\text{GeV}$) particles.

In Fig. 55 two turns of the SPS are displayed. The green graph represents the particle intensity in the SPS, the bunch train of 144 bunches with 4×36 bunches is clearly visible. The fast transverse kicker magnet (yellow) is gated to the section outside the bunch train[44]. The settings of the fast gated transverse kicker magnet system are displayed in the Fig. 56. The injection losses of the cleaned beam injections (MKQ
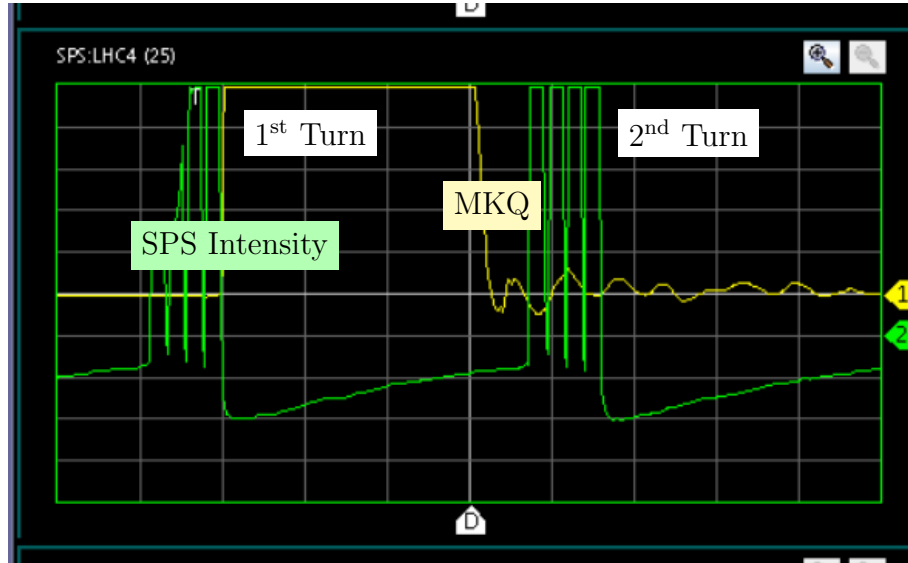
Figure 55: Screenshot of the SPS tune kicker display showing two turns of the SPS. The yellow line indicates the waveform of the MKQ's field. The green line represents the beam intensity in the SPS. The low bunch train signals in the first turn are electronics related. The beam intensity is constant. The four high signals result from the four trains of 72 bunches circulating in the SPS.

---

[44]For this measurements only one (MKQV3) of the eight available magnets was used.

Figure 56: SPS tune kicker display with kicker magnets' parameters. In total eight tune kicker magnets are available. These fast gated magnets allow to excite the particles oscillations until their trajectories are not stable anymore, so that they are lost. For cleaning the SPS from re-captured particles only one kicker MKQV(3) was used.

on) are displayed in Fig. 57 together with two loss signatures without the cleaning (MKQ off)[45]. Both loss signatures of the cleaned beam injections show in phase one a reduced loss signal compared to the loss signatures of the injections without the cleaning. The loss reduction with cleaning on was about 24% in phase one. A zoom in the fourth phase of the loss signature, the fall of the LHC's injection kicker fields is shown in Fig. 58. The cleaning effects only the width of the signal. For the two recorded loss signatures with the SPS's transverse kicker magnet on the loss signal in phase four is about $0.1\,\mu s$ shorter. The variation of the losses from injections with similar settings shows the large variance of the loss signatures for the same injection scheme, e.g. the measurements without cleaning show a significant variation in the signal amplitude, see Fig. 58. Comparing the two injections with cleaned beam from the SPS with the normal injections, the cleaned beam injections show 20% less losses during the fall time of the injection kicker magnets. For more detailed conclusions of the cleaning effects on the signal amplitude in the last phase a higher statistic of injections with the same set of settings are needed. The performed measurements already showed that by using the transverse kicker magnets in the SPS a reduction of the re-captured beam and so a reduction of the losses during injection into the LHC can be achieved. Up to now the injection losses were reduced by about 25% using this method. In the future measurements are needed to optimise the settings (gate lengths, and magnet strength) for a further reduction of the re-captured particles in the SPS.

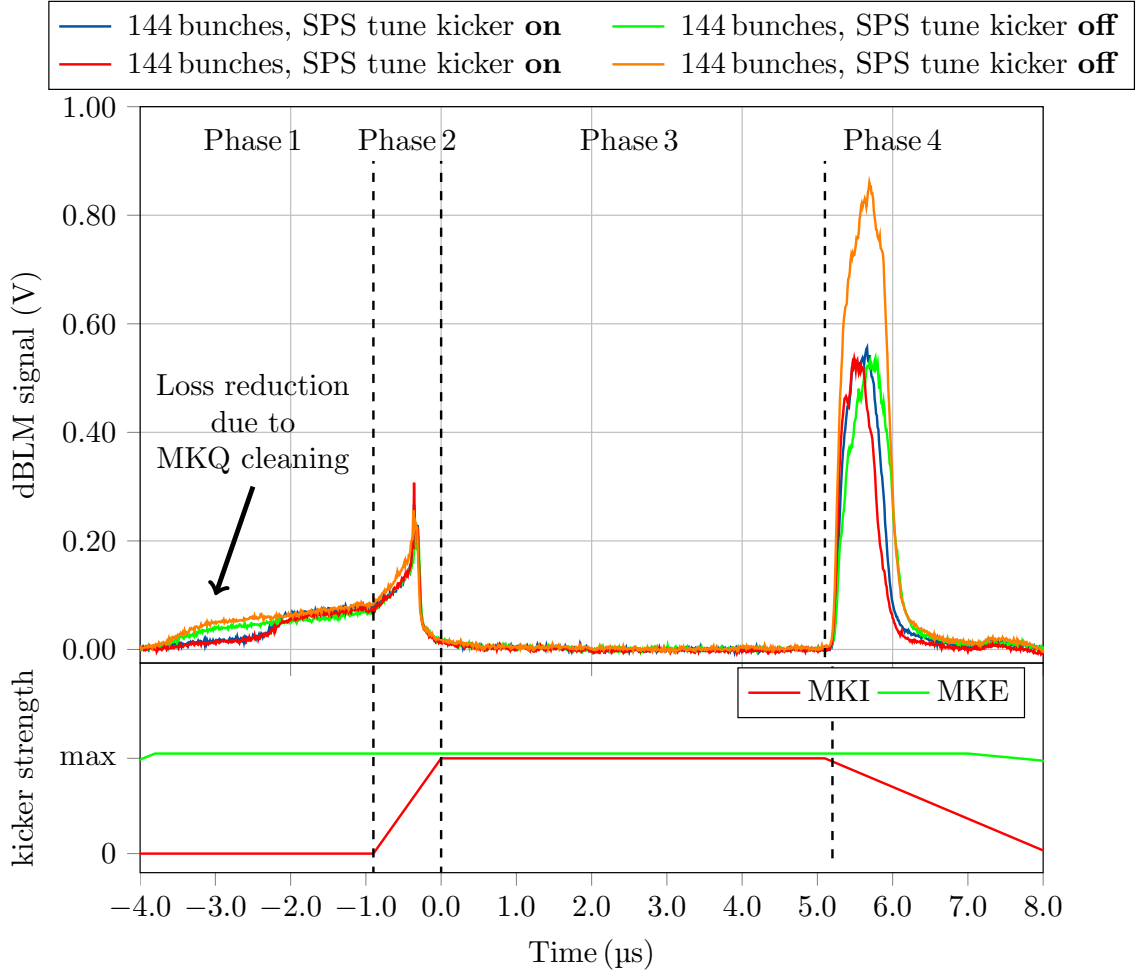[45]The four measurements were performed consecutively during a dedicated beam time at the LHC.

Figure 57: Four loss signatures of injections of 144 bunches. For the first two injections the SPS tune kickers were used for reducing the re-captured particle intensities in the SPS. This procedure resulted in reduced losses in phase one and four of the loss signatures. The two loss signatures were recorded with the same LHC settings for comparison, directly after the injections with the cleaning on.
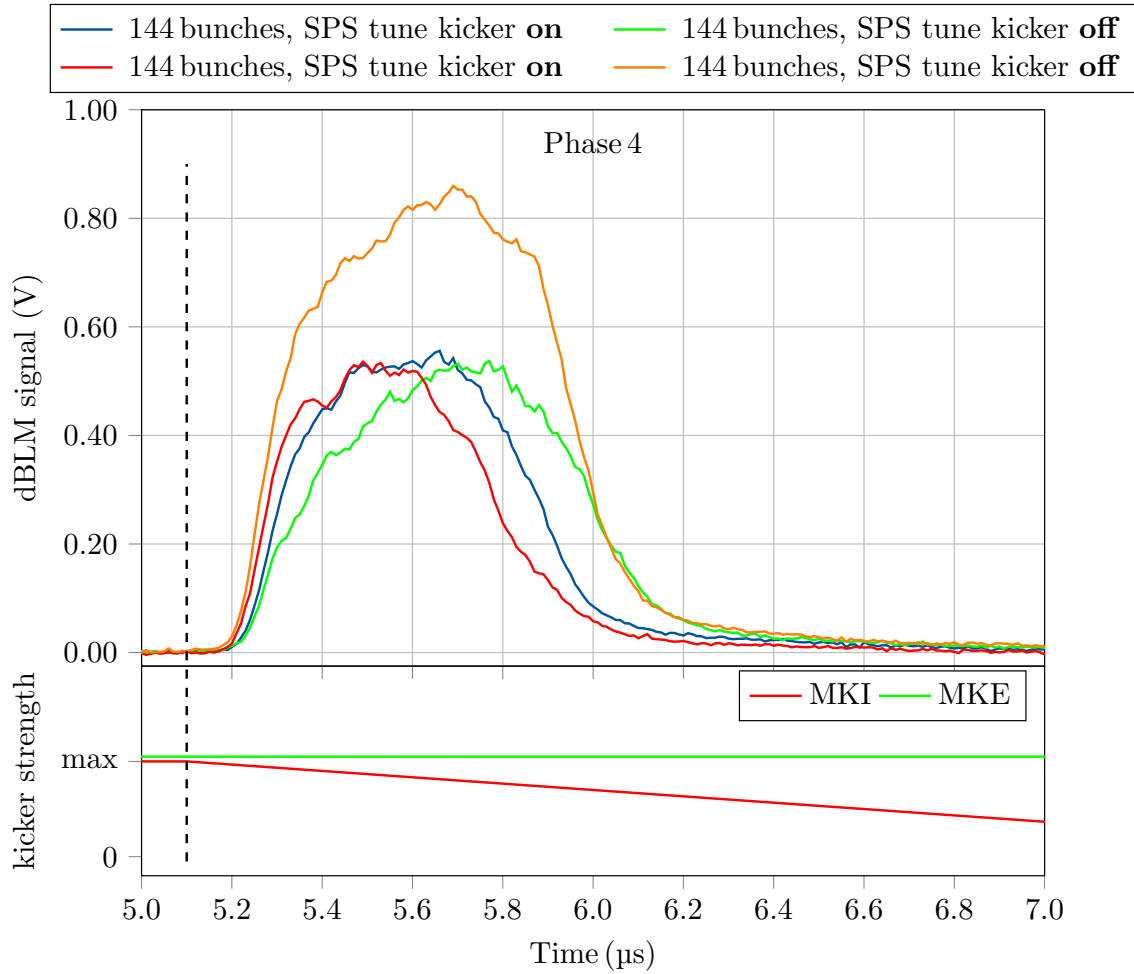
Figure 58: Detailed display of the second loss signal in phase four of the loss signatures shown in Fig. 57. The length of the loss signal of 'cleaned' injections (tune kicker on) is about 0.1 µs shorter than for the normal injection (tune kicker off). The losses in phase four were reduced by 20% by using the SPS tune kicker magnets. The loss signals in phase four show a large variation even with similar LHC parameters.

7.5.5 Using an additional RF-cavity in the PS for reducing the recaptured particle intensities in the SPS

The re-captured bunch intensity in the SPS depends on the coasting particle intensity after the beam transfer from the PS into the SPS. The coasting beam intensity again depends on the beam transfer from the PS and the injection quality into the SPS. In order to improve the beam transfer an additional RF-cavity for rotating the bunches at the end of the PS cycle was introduced. In order to fit the SPS

beam in the 200 MHz RF-buckets of the SPS the bunches need to be shortened, see chapter 7.2. Until Summer 2016 only one RF-cavity was used. The resulting bunch geometry caused a large amount of un-captured beam during the injection into the SPS. By using an additional cavity for the rotation process the bunch geometry was optimised, which resulted in a reduction of un-captured particles during the injection process into the SPS. With less un-captured particles available the re-captured particle intensities were reduced accordingly. As a final result, the injection losses in the LHC injection regions were reduced by a factor 10 by using the additional RF-cavity in the PS. With this optimised bunch rotation the loss levels were reduced from formerly 95% to below 10% of the dump thresholds, which is an acceptable level for continuous operations. Since September 2016 the bunch rotation procedure with two cavities is implemented in the PS cycle.

7.5.6 Future plans for mitigating the injection losses

The above described mitigation techniques were successfully demonstrated. The 'empty' kicks are applied on regular a basis. The same applies for the second cavity in the PS for rotating the bunches.

Nevertheless for a further reduction of the injection losses the other techniques have to be optimised in the future. A focus will be on the reduction of re-captured beam by using the SPS transverse kicker magnets. For this method the window and magnet strength of the fast gated magnets have to be optimised. The continuous recording of the injection losses in the LHC will indicate how effective the beam cleaning in the SPS can be.

The injection gap cleaning is used for most of the injections into the LHC. As described above the cleaning window can be adjusted further so that not only the slot for the next bunch train is cleaned from circulating beam but also the injection gap. This optimisation has to be done carefully during a dedicated beam time. The optimum between the cleaning and the least possible excitation of the last bunch of the upstream bunch train needs to be explored.

Ideally the beam is cleaned from unwanted particles outside the bunch train as early as possible in the beam preparation phase. The lower the energy of the particles, the less dose is deposited in the accelerator components during the cleaning due to lost particles. Therefore the optimised bunch rotation at particle energies of 26 GeV at the end of the PS cycle is a good and efficient technique.

7.6 Identification of injection faults

The diamond based beam loss monitors can record very short signals with a very large loss amplitude due to their high time resolution and the wide dynamic range. Therefore ultra fast unexpected losses during the injection can be measured, which indicate a failure in the injection procedure. The position of these high losses within the loss signature provides information about the type of failure.

7.6.1 Example: High losses due to faulty over injection of a pilot bunch

At the beginning of the LHC filling procedure the accelerator setup is validated by injecting a pilot bunch (1×10^{10} protons). Later in the filling process a train of nominal bunches will be injected at the position of the pilot bunch, which means that the pilot bunch is deflected by the injection kicker magnets and is then lost on the internal absorber block, this procedure is called over injection. In case of a normal over injection the pilot bunch passes the injection kickers during the flat top time, resulting in a deflection of the pilot with the nominal field strength. The pilot bunch then hits the absorber block with full impact parameter. The thresholds of the BLM system are set high enough to not trigger a dump due to the particle showers created by the pilot bunch downstream of the absorber block. On 24.06.2016 the LHC beam was dumped several times during the filling process due to high losses during an injection. The reason for these dumps was a faulty over injection of the pilot bunch. The settings in the LHC injection sequencer were wrong[46]. The result was that during an injection the pilot bunch passed the injection kickers while the fields were already falling. This lead to a smaller deflection angle and so to a smaller impact parameter on the absorber block. As described in chapter 7.3, with a smaller impact parameter the particle to shower ratio changes, i.e. the same amount of particles created larger showers. With the pilot bunch impacting on the absorber block with a smaller impact parameter the created losses were high enough to trigger a beam dump. The identification of this fault took several hours.

The loss signature recorded with the diamond based beam loss monitors revealed directly the problem of localised high losses during the fall time of the injection kicker magnets. In Fig. 59 the loss signature of the injection is displayed, which shows the additional high loss signal resulting from the misplaced and then over injected pilot bunch[47]. The loss in the fourth phase, during the fall time of the injection kickers is clearly visible. The localised losses, the width of the signal is 15 ns, indicates that the losses must be caused by a bunch like particle distribution (high intensity within 2 - 5 ns). Figure 60 shows the same signal recorded with the low gain channel (CH2),

[46]The injection sequencer is a tool, in which the injection schemes and the LHC buckets for the injections are listed.

[47]The loss signal is cutoff at 400 mV due to limitations in the readout electronics.

which is limited to 10 V. The pilot bunch signal amplitude exceeds the rest of the lost signature by two orders of magnitude.

With this information of the loss signature the misplaced bunch as major loss contributor could have been identified instantaneously.
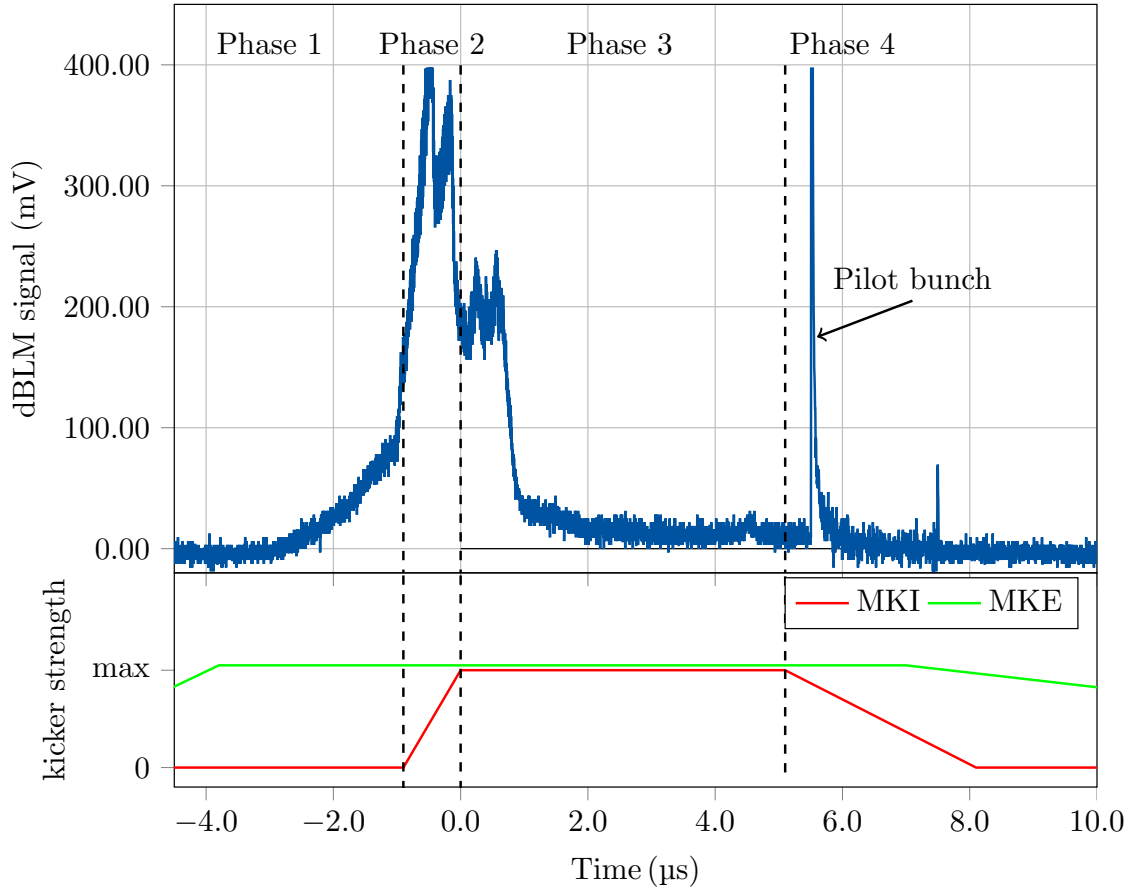

Figure 59: Over injection of a mis-placed pilot bunch, the pilot is placed in a slot where the injection kicker (MKI) fields are falling. This lead to very high losses due to a small impact parameter. The localised high loss signal, signal width of 15 ns, indicates that the losses came from a bunch like structure, high intensities in 2 - 5 ns. The signal is cut off due to resolution limits in the readout electronics at 400 mV.
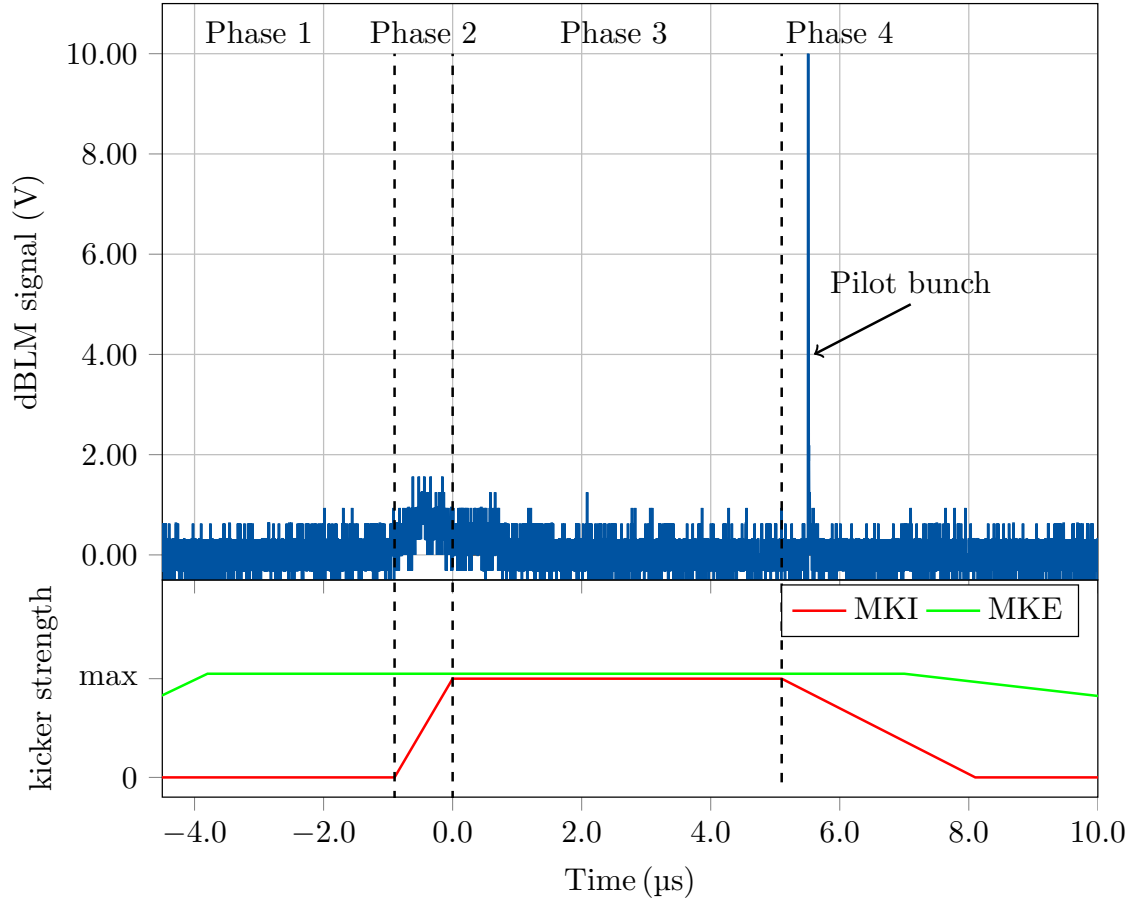
Figure 60: Over injection of a misplaced pilot bunch, same event as shown in Fig. 59, recorded on the low gain channel of the readout electronics which covers a larger range of loss amplitudes. The pilot loss signal amplitude exceeds the rest of the loss signature by two orders of magnitude which makes this loss signal even more visible and easy to identify.

7.6.2 Automated injection loss analysis based on the diamond based beam loss monitor data

The presented analysis of the injection loss measurements in chapter 7.4 shows that the diamond based beam loss monitors give a lot of valuable information of the injection loss signatures and so about the quality of the injection. With the LHC injection quality check system (IQC) every injection into the LHC is analysed [56]. With these systems the operators get an instant feedback of the injection quality based on various inputs (trigger of the extraction and injection kicker magnets, beam losses in the transfer lines and injection regions). Loss measurements in chapter 7.4 have shown that due to the high time resolution of the dBLMs different loss mechanisms were identified. The inclusion of the dBLM data into the injection quality check routines and the visualisation of the data would give more detailed information about the injection loss signatures. By logging these loss signatures for every injection scheme standard loss signatures could be derived. By comparing the actual injection loss signature with the corresponding standard signature automatically, a powerful additional injection quality check would be available. Since the injection losses strongly depend on the beam preparation, these measurements would give information about the quality of the beam preparation in the pre-accelerator chain as well. An inclusion of the loss measurement in IR 7 close to the primary collimators would give an even more complete picture of the injection losses. This would combine the measurements of the longitudinal and the transversal losses of the injected bunch train. With this additional information the operators could easily identify the driving mechanisms for the losses during injections. With the fast identification of the underlying mechanisms in case of high losses the correct countermeasures could be applied without losing time.

8 Additional applications of the diamond based beam loss monitors at the LHC

8.1 Measuring the ultra fast beam losses during the beam dump procedure in IR 6 and calculations of expected loss signals during an asynchronous beam dump
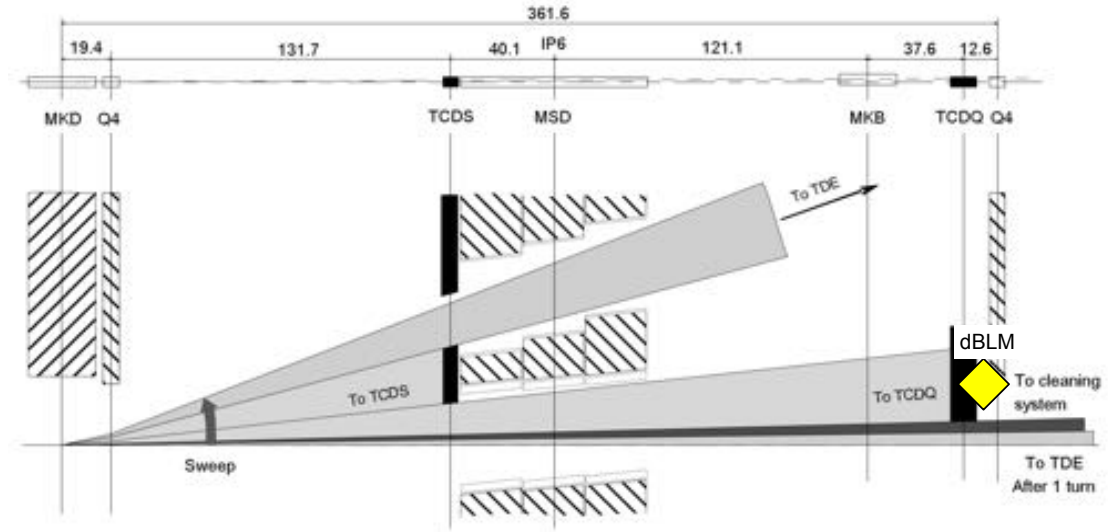

Figure 61: Conceptual layout of the LHC beam extraction in IR 6. The beam is steered by the extraction kicker magnets (MKDs) into the dump line towards the dump block (TDE). Absorber blocks (TCDS, TCDQ) protect the downstream accelerator components from mis-steered particles [58]. The diamond based beam loss monitor, yellow, downstream of the TCDQ detects the ultra fast extraction losses.

Beside the injection loss measurements the dBLMs have more applications. During the beam dump procedure ultra fast beam losses were observed in IR 6 with loss durations less than 3 µs. In order to avoid high losses due to mis-steered nominal bunches the extraction kicker magnets are synchronised to the 3 µs long ideally particle free abort gap. During the 2.9 µs long rise time of the extraction kickers the deflection angle is too small to steer the passing particles into the dump line, instead they are lost downstream of the kicker magnets. In order to protect the accelerator components from extraction losses, massive absorber blocks are installed downstream of the extraction kickers, see Fig. 61. The abort gap is not completely empty, it is populated with small amounts of particles which result from coasting beam, see chapter 2. These particles are mis-steered by the rising kicker fields caus-
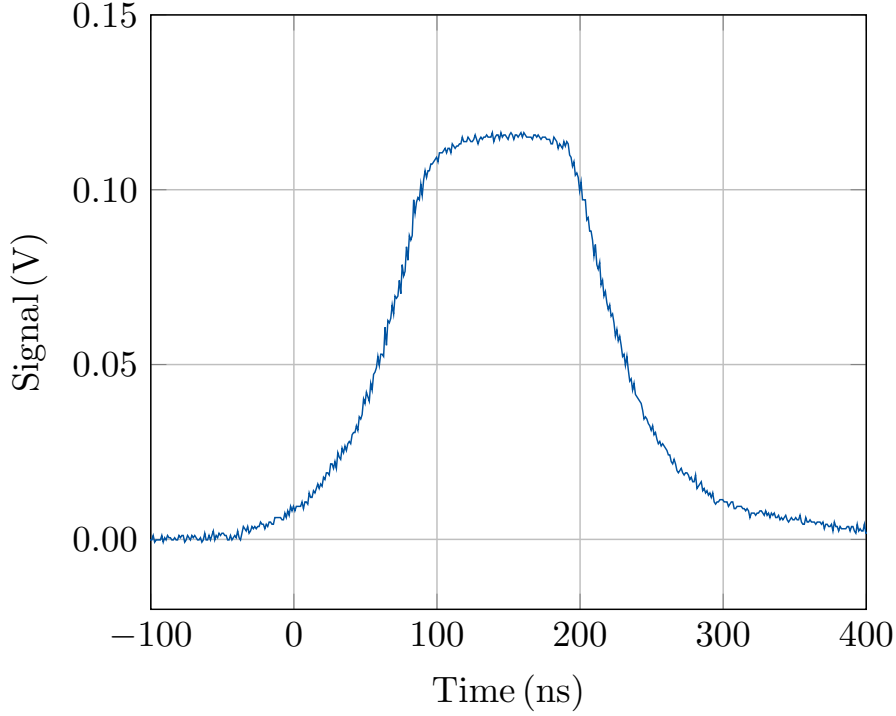
Figure 62: Loss signal of an end of physics fill beam dump. The signal results from mis-steered particles, which populate the abort gap. The dBLM detects the showers from particles impinging on the TCDQ absorber.

ing the ultra fast extraction losses, which scale with the abort gap population. High extraction losses resulting in secondary showers downstream of the absorber block, which can cause quenches in the superconducting magnets. Abort gap populations up to 5×10^9 protons are acceptable [59]. If the maximum acceptable population is exceeded, the abort gap is cleaned by using the LHC's transverse damper system [60]. In order to measure the ultra fast extraction losses LHC type diamond based beam loss monitors were installed downstream of the absorber block protecting the superconducting quadrupole downstream of the extraction kickers. In Fig. 62 an exemplary dump signal is displayed, which is representative for normal beam extraction. The signal width is about $150\,\mathrm{ns}$ and the loss amplitude is $0.12\,\mathrm{V}$. The abort gap population for the loss signal shown was about 3×10^9 protons in $3\,\mathrm{\mu s}$, which corresponds to 1.5×10^8 protons within $150\,\mathrm{ns}$ assuming an equal distribution of the protons in the abort gap.

By using the response function of the LHC type dBLM, which was measured during a dedicated test campaign, see chapter 5, the intensity of 4.5×10^4 particles impacting on the dBLM was calculated[48]. This gives the conversion between the number of particles impacting on the absorber block and the number of particles impinging on the diamond based beam loss monitor.

8.1.1 Estimation of shower intensities during an asynchronous beam dump and dBLM setup optimisation

An asynchronous beam dump, a failure scenario during beam extraction where the extraction kicker magnets are not synchronised to the abort gap, will result in massive beam losses in the extraction regions of the LHC due to mis-steered nominal bunches. In Fig. 63 the difference between a synchronous and an asynchronous beam dump are depicted schematically. In the worst case, the extraction kickers rise due to a faulty trigger while trains of high energetic bunches are passing the abort gap. This can result in up to 116 mis-steered bunches[49] lost downstream of the kicker magnets. The layout of extraction region with its massive absorber blocks should be capable to absorb the high energetic bunches and so protect the accelerator components from damage. However, quenches in the superconducting magnets are expected. Until beginning of 2017 no full scale asynchronous beam dump event happened during LHC operation, i.e. an asynchronous beam dump with high energetic high intensity beams. During an asynchronous beam dump up to a maximum of 1.3×10^{13} protons would be lost on the absorbers, which is almost four orders of magnitude higher than the accepted maximum abort gap population intensity. In addition, the particle intensities would not equally be distributed but bunched, which resulted in very high loss peaks with a 25 ns spacing. The study of the loss signature and loss amplitudes of an asynchronous beam dump are of great interest for the operators. Loss signatures with high time resolution will reveal how many bunches were lost on the absorbers in the extraction region, which will give valuable information about the dump process.

At the moment only the installed dBLMs provide the required time resolution for bunch-by-bunch measurements for identifying the number of lost bunches during an asynchronous beam dump. In addition, the wide dynamic range of the dBLMs allows to record the high loss amplitudes without saturating the detectors.

The aforementioned extraction loss measurements have shown that during a normal dumping process with an abort gap population of 3×10^9 protons about 4.5×10^4 particles are detected in the diamond based beam loss monitor.

---

[48] As shown in chapter 5 the charge collection efficiency differ between the detectors, but nevertheless the the response function can be used to estimated the impacting particle intensity.

[49] With a bunch spacing of 25 ns 116 bunche can pass the kicker magnets during the rise time of 2.9 µs.

Using this conversion, the loss of a full bunch with 1.1×10^{11} can be estimated to 2×10^7 particles impacting on the dBLM. These intensities are very close to the tested limits of the LHC type dBLMs, see chapter 5. Therefore, the LHC type dBLMs were replaced with special diamond based beam loss monitors[50], which were developed for measuring very high particle intensities [61]. These detectors are characterised for intensities up to 2×10^{10} particles within $10\,\mathrm{ns}$ [62]. With the optimised diamond based beam loss monitor setup asynchronous beam dump loss signatures can be measured with bunch-by-bunch resolution without being limited by saturation effects.

---

[50]These polycrystalline CVD dBLMs have a smaller surface and charge collection efficiency is lower than 10%.
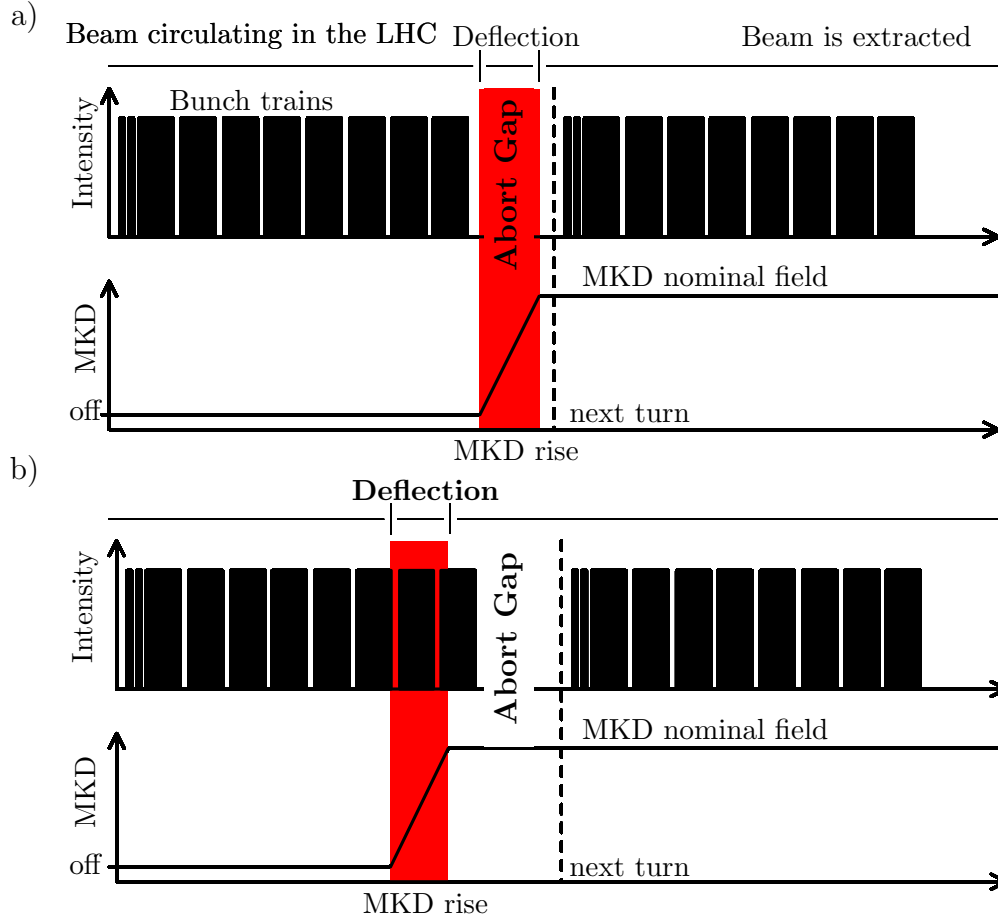
Figure 63: The extraction kicker magnets (MKD) have a rise time of about 2.9 µs, red. During a normal dump procedure, a), the extraction kickers are synchronised to the 3 µs long abort gap, so that ideally no high energetic particles are mis-steered due to rising kicker fields. The extraction kickers are at their nominal field strength when the next bunches pass, so that the beam is steered into the extraction line and safely dumped. In case of an asynchronous beam dump, b), the extraction kicker magnets are triggered without the synchronisation to the abort gap. In this case high intensity bunches are deflected by the rising kicker fields, which results in massive beam losses in the extraction region leading to quenches in the downstream magnets.

8.2 Experimental setup for measuring the abort gap population by detecting beam gas interaction in IR 4

This section gives an overview of the ongoing study about using dBLMs for measuring the LHC's abort gap population by detecting the showers from interactions of the circulating particles in the abort gap with the rest gas. Simulations and first measurements will be presented.

To guarantee a safe beam dump the extraction kicker magnets are synchronised to the abort gap. This abort gap is not completely empty but, it is populated with small amounts of particles, which lead to ultra fast extraction losses, see chapter 8.1. Populations up to 5×10^9 particles over the $3\,\mu s$ long abort gap are acceptable before cleaning processes are started [59]. For reducing the abort gap particle population the transverse damper system is used. For cleaning the abort gap this system is gated on the $3\,\mu s$ long abort gap, where it excites the particles' trajectories so that they are lost on the collimators in collimation regions in IR 7 [57]. A continuous operation of the transverse damper for cleaning the abort gap can compromise the life time of the circulating beam. Therefore, the abort gap has to be monitored continuously and only if the population exceeds the thresholds the cleaning is switched on. The abort gap population is measured with the synchrotron light monitor (BSRA), which is integrated into synchrotron light telescope (BSRT). This device detects the synchrotron light, which is emitted by the high energetic particles passing the dipole field of the beam separation magnets in IR 4. The BSRA is gated to the abort gap and detects the light emitted by the particles in the abort gap [63].

The motivation for an additional abort gap monitoring system is redundancy such that in case of a failing BSRA the abort gap can be still monitored. In the scope of this thesis the feasibility of a dBLM based abort gap monitor was investigated resulting in an experimental setup, which is installed in IR 4 of the LHC.

8.2.1 Experimental setup of a dBLM based beam loss monitor

The basic idea for the setup is to measure the abort gap population by detecting the showers from interactions of the particles in the abort gap with the rest gas. At a constant rest gas pressure and known beam gas interaction cross section the interaction rate depends on the circulating particle intensity. Therefore, the abort gap population can be calculated from the detection rate of the beam gas interactions. The high time resolution of the diamond based beam loss monitors allows the localisation of the origin of the beam gas interaction, i.e. if the interaction happened in the abort gap or somewhere else in the beam. In the feasibility study the optimised setup parameters were calculated. The conceptual layout of the setup is shown in Fig. 64. In order to achieve high count rates the setup was installed close the beam gas ionisation monitor (BGI), where neon gas can be injected. An increase
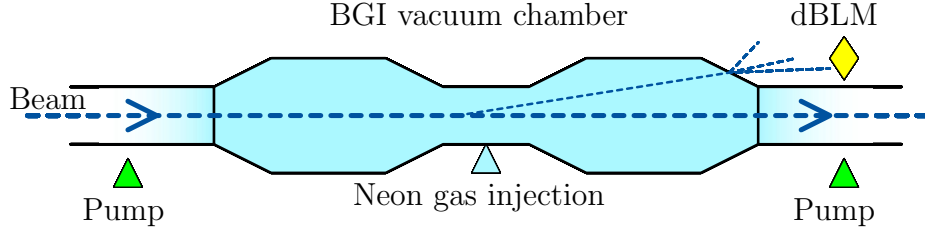
Figure 64: Schematic layout of the experimental setup for measuring beam gas interactions with the dBLM at BGI in IR 4. To increase the interaction rate neon gas is injected into the vacuum chamber. Pumps upstream and downstream of the BGI vacuum chamber confine the gas. A dBLM downstream of the vacuum chamber detects particle shower resulting from beam gas interactions.

of the gas pressure in the vacuum chamber results in a higher count rate since the interaction rate scales with the gas pressure. For detecting the particle showers a CMS type single crystalline dBLM was installed downstream of the BGI vacuum chamber. The maximum neon pressure is limited to 8.8×10^{-8} mbar so that the beam life time is not compromised. With this setup the abort gap population can be measured in parallel to the normal beam operation.

The expected detection rate of the beam gas interactions is in the order of 1 - 10 Hz. In order to achieve a significant statistic the interactions have to be integrated over minutes. Therefore, a readout system with a corresponding acquisition time is required. The CIVIDEC ROSY data acquisition system was installed, which is operated in the histogram mode[51] with a bin width of 1.6 ns, see Fig. 65 [46]. This mode allows loss measurements with nanosecond bin resolution over minutes or even up to hours.

8.2.2 First measurements of beam gas interactions

Figure 66 shows a full loss histogram of beam 1, which was recorded with the diamond based beam loss monitor in IR 4. The trains consisting of 72 bunches are clearly visible. The LHC was filled with 1824 bunches resulting in a longer gap as the required 3 μs at the end of the filling patter. The counts in the bunch free gap result from particle losses in beam 2, referred to as cross talk[52]. These measurements were performed with a lower neon pressure of 5×10^{-9} mbar due to LHC opera-

[51]In the histogram mode the LHC turn is discriminated into 55750 bins. If the signal from the dBLM exceeds at a certain point in the turn a set threshold the corresponding bin is incremented, see Fig. 65.

[52]The distance to the second beam pipe is 25 cm. Particle losses in the second beam due to beam gas interactions and the resulting secondary showers are detected by the dBLM as well.
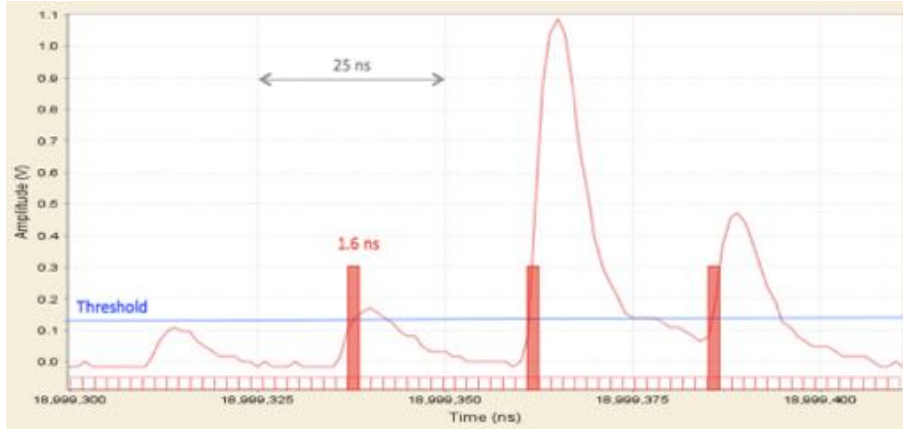
Figure 65: Illustration of the two measurement modi of the CIVIDEC ROSY system. The first modus allows time-loss measurement. The red line represents the signal from the dBLM. In the second mode, the histogram mode the LHC turn is divided into 55750 bins with a width of 1.6 ns. When the signal exceeds the preset threshold the corresponding bin is incremented, red bars. This mode allows long time integrations of beam losses.
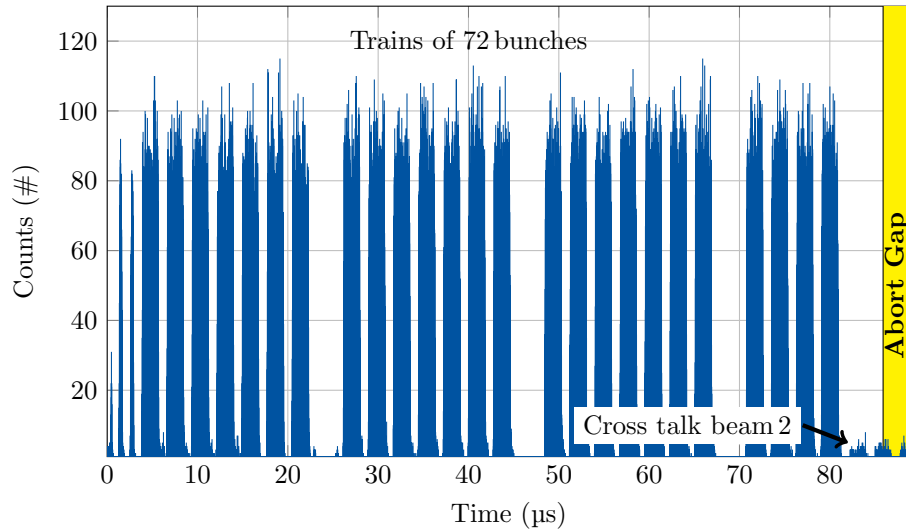

Figure 66: First measurements of the beam gas interactions of beam 1. Neon gas was injected into the vacuum chamber for increasing the interaction rate. The filling pattern, the sequence of trains of 72 bunches, is clearly visible. Each blue block represents a train of 72 nominal bunches. The abort gap is located at the end of the filling pattern. The low signals at the end of the filling pattern and in the abort gap come from cross talk of the second beam.
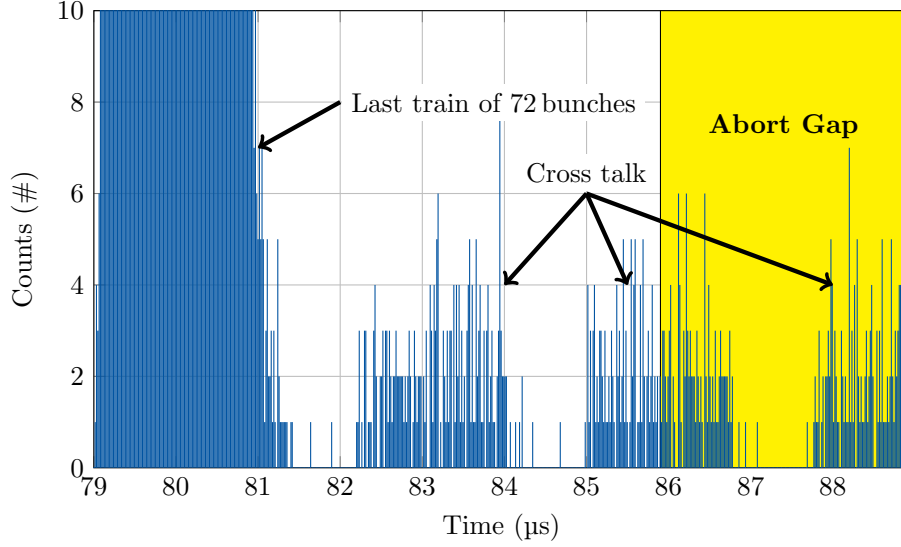
Figure 67: Zoom into the end of the filling pattern of the loss histogram shown in Fig. 66. In this case the gap was longer as the indicated 3 µs due to a reduced number of bunches in the beam. The cross talk from the second beam is visible. The data is smeared out so that single bunches can not be identified.

tion reasons, instead of 8.8×10^{-8} mbar, which were used in the simulations. The measurement shows that the setup is capable of detecting the beam gas interaction since this is the dominant loss mechanism in the region of the setup. The zoom into the abort gap, displayed in Fig. 67, shows that the resolution of the setup with the CIVIDEC ROSY data acquisition system does not reach the bunch-by-bunch resolution, which is necessary to distinguish between the losses from particles in the abort gap, losses from nominal bunches and from cross talk coming from beam 2. The signals of the single bunches are smeared out and overlap each other. The same effect was observed in the cross talk signals. During a dedicated beam time the loss histogram of a single circulating bunch was recorded, see Fig. 68. The measurements shows that a single bunch is smeared out over about 62 bins, i.e. 100 ns. Previous measurements with the same readout system showed that a single bunch covers 2-3 bins corresponding to 3-5 ns [46]. This indicates that there are issues with the readout electronics most likely with the timing, so that the histogram does not stay synchronised to the beam. The count rates were calculated by including the integration time of the displayed histogram. The derived rates were a factor 70 below the rates, which were calculated in the feasibility study [64]. In the feasibility study a linear dependency between count rate and neon gas pressure was assumed.
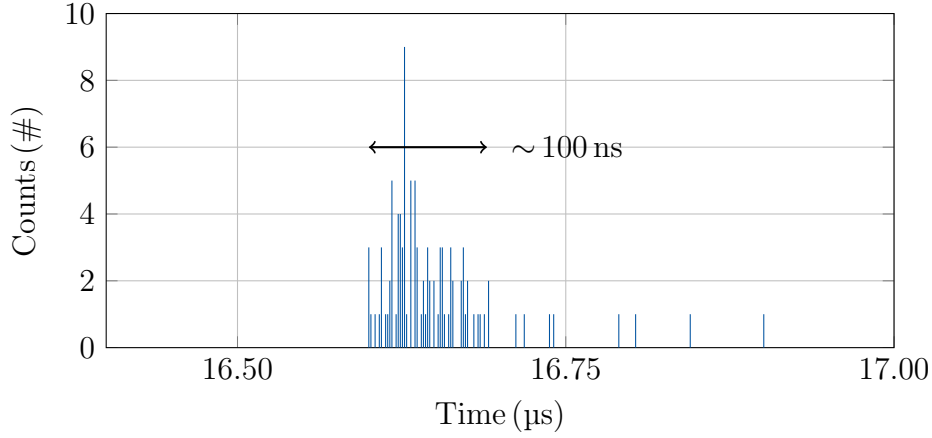
Figure 68: Loss histogram of one isolated nominal bunch in the LHC. The bunch width is about 100 ns, which is much wider than the expected 3 - 5 ns. Bunch-by-bunch or even intra bunch measurements are not possible at the moment due to the smeared out bunch signals.

8.2.3 Next steps to progress the study of the experimental abort gap monitor based on dBLMs

Unfortunately it was not possible to complete the study on the dBLM based abort gap monitor within the time of this PhD project. Therefore, recommended next steps for progressing the study will be briefly discussed.

Solving the timing issues of the readout electronics

The distinction between losses from nominal bunches and from other particles is only possible if these losses can be clearly identified in terms of position in the beam. Therefore, it is important to achieve the bunch-by-bunch resolution in the loss histograms. In other test setups it was demonstrated that the installed acquisition system is capable of recording loss histograms with bunch-by-bunch resolution. Therefore, it is speculated that there is a failure in the synchronisation of the histogram unit with the beam. The signal smears out due to the resulting time jitter. By optimising the input of the timing information into the readout system will likely solve this issue.

Continuous loss measurements with different gas pressures

The presented measurements were all performed at very low neon gas pressures. Conducting tests with different pressure levels will reveal the influence of the gas pressure on the count rate. These measurement will confirm that the assumption of the linear dependency of the interactions and the neon gas is valid.

Exchange of the CMS type dBLMs with LHC type diamond based beam loss monitors

If the aforementioned two steps do not allow an improvement of the quality of the measurements, the CMS detectors can be exchanged with LHC type detectors. The CMS type detectors have a very high charge collection efficiency of more than 95% so that they are sensitive to single particles but their surface is small, see chapter 6.1.2. LHC type detectors have a lower charge collection efficiency, about 25% to 40%, but the surface of the diamond crystal is four times larger compared to the CMS type detectors, which results in a higher particle fluence through the diamond material, which should more than compensate the lower sensitivity. In contrast to the CMS detectors the signal in the LHC type detectors is not shaped, see chapter 6.1. The raw signal has a larger amplitude, which will result in a better signal to noise ratio.

8.2.4 Conclusion

At this stage of the study the first measurements have given a proof of principle that beam gas interactions can be detected with the dBLM setup. The beam gas interactions from the nominal bunch trains were successfully measured. Problems with the synchronisation of the data acquisition system to the LHC beams result in a time jitter in the data, which prevents bunch-by-bunch resolution. To continue with the measurements the timing issues have to be solved first. With the operational readout electronics the cause for the low count rates has to be investigated. Even if the predicted count rates, which were calculated in the feasibility study, can not be reached the setup will allow continuous measurements of the beam gas interactions of the whole beam. The resulting loss histograms will give valuable information of the particle distribution in the circulating beams.

8.3 High resolution loss measurements at the primary collimators in IR 7

The primary collimators in IR 7 form the aperture bottleneck in order to define the precise transverse dimensions of the beam. Particles with a large transverse deviation from the closed orbit exceeding the aperture limits are lost on the jaws of these collimators. To measure these losses with bunch-by-bunch resolution LHC type diamond based beam loss monitors are installed downstream of the collimators. Equipped with a fast sampling oscilloscope the loss signatures can be recorded with nanosecond resolution. As already discussed in chapter 7.4.5 with the dBLMs at the collimators the transversal losses of the injected bunch trains can be measured when they pass the collimators.

Another very fast / ultra fast beam loss scenario are the unknown falling objects (UFO) [47], [32]. These UFOs are dust particles in the range of micrometers, which fall from the top of the beam pipe into the circulating beam. The circulating particles are scattered by the dust particle, which results in local losses for large scattering angles. For small scattering angles the particle's continue on their trajectory but the amplitude of the particle's oscillation around the closed orbit is increased. These particles are lost on the primary collimators in the collimation region. Therefore it is possible to measure the UFO events in IR 7 even if the actual UFO event happened somewhere else in the LHC [15]. The UFO loss events can last from about one hundred microseconds up to several milliseconds, which compares to several turns of the LHC. UFO events are a frequent loss event. During the LHC recommissioning phase after the long shutdown (LS1) in 2015, the rate of the UFO events
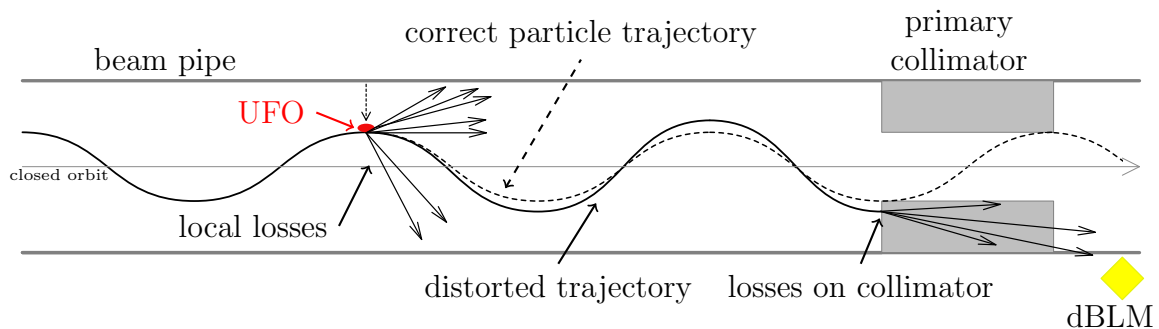
Figure 69: Schematic representation of a UFO loss event. A dust particle, red, falls into the circulating particles. The scattered particles create local losses at the position of the UFO. Particles with a small scattering angle continue on a trajectory with an increased oscillation amplitude. These particles are lost on the primary collimators, the aperture bottleneck of the LHC. The losses are detected with the dBLM downstream of the collimators.

was about 40 UFOs/hour. This rate decreased during the year and stabilised at 10 UFOs/hour. In some cases the losses even exceeded the dump threshold of the beam loss monitors, which resulted in a beam dump. In a few cases the UFO events actually caused quenches in the superconducting magnets [31]. The detailed loss mechanisms and the cause for the UFO events is not yet fully understood and is still under investigation. A dedicated system using the ionisation chamber beam loss monitors of the LHC beam loss monitoring system was developed and commissioned in the past years for detecting the UFO events and their locations in the LHC [65]. Since the system uses the icBLMs, the time resolution is limited to 80 μs, see chapter 3. For high time resolution measurements of the UFOs dBLMs are used. It has been demonstrated already, that all bunches in the beam contribute to the loss event and the trend of the loss signature can be approximated with a gaussian function [47]. In 2016 the dBLM setup in IR 7 was recommissioned for measuring UFO events at beam energies of 6.5 TeV. In Fig. 70 the loss signature of a UFO event is displayed, which led to a beam dump after five turns. The losses increased with every turn until the beams were dumped. The losses end with a high signal resulting from particles in the abort gap, which were mis-steered by the rising extraction kicker magnets. The zoom into the loss signature allows the identification of the bunch trains in the beam, see Fig. 71. The high resolution data allows even the analysis of losses from single bunches during the UFO event, see Fig. 71. These high resolution measurements give information of shapes and lengths of the loss signatures of the UFOs. Therefore, the diamond based beam loss monitors in IR 7 are an excellent tool for the operators to investigate the ultra fast beam losses at the primary collimators with a nanosecond time resolution. In addition to the data from the ionisation chamber beam loss monitors, the results of diamond based beam loss monitor measurements will contribute to a better understanding of the loss mechanisms of the UFO events in the future.
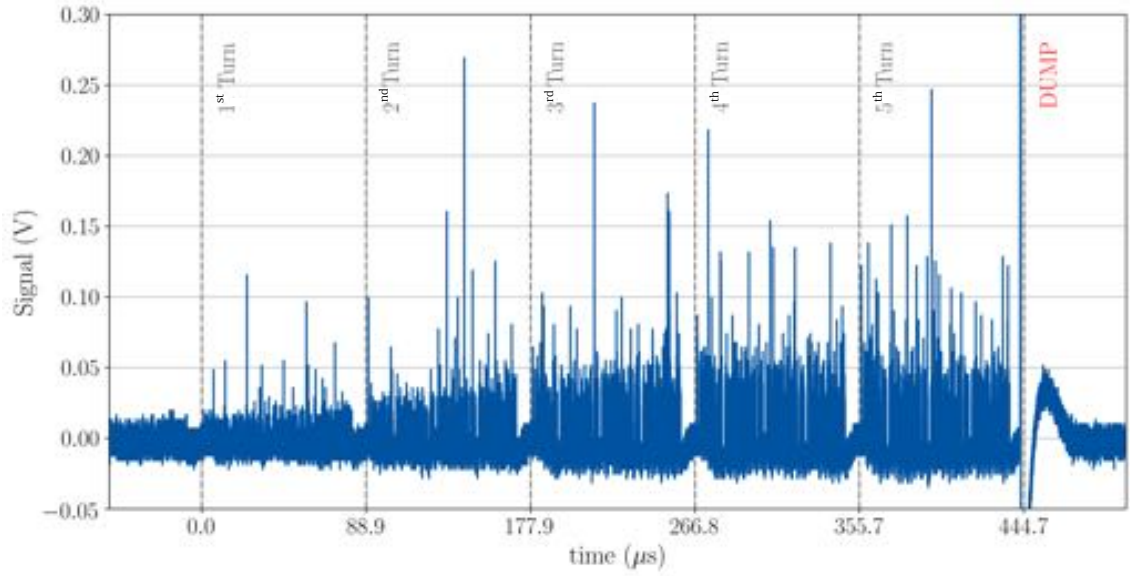
Figure 70: Loss signature of a UFO event, which led to a beam dump. The loss signature shows that the losses built up over several turns. All bunches in the LHC contribute to the loss event. At the end of the 5th turn the beams are extracted. The last extreme high loss signal origins from particles in the abort gap, which were deflected by the rising extraction kicker fields.
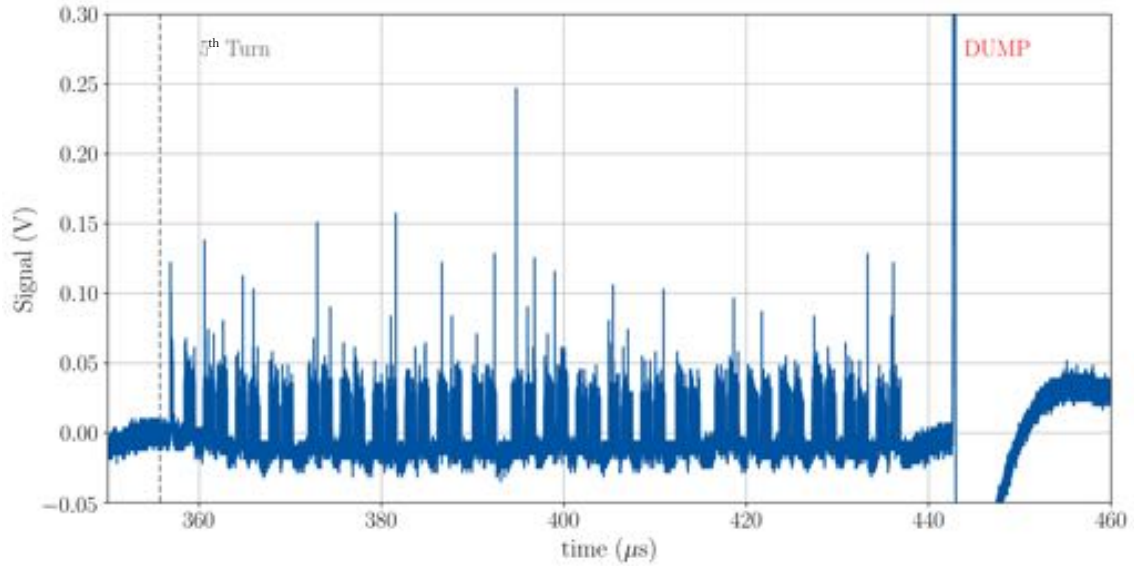

Figure 71: Zoom into the data of the 5th turn of the UFO loss signature, which is displayed in Fig. 70. The sequence of bunch trains in the beam is clearly visible.
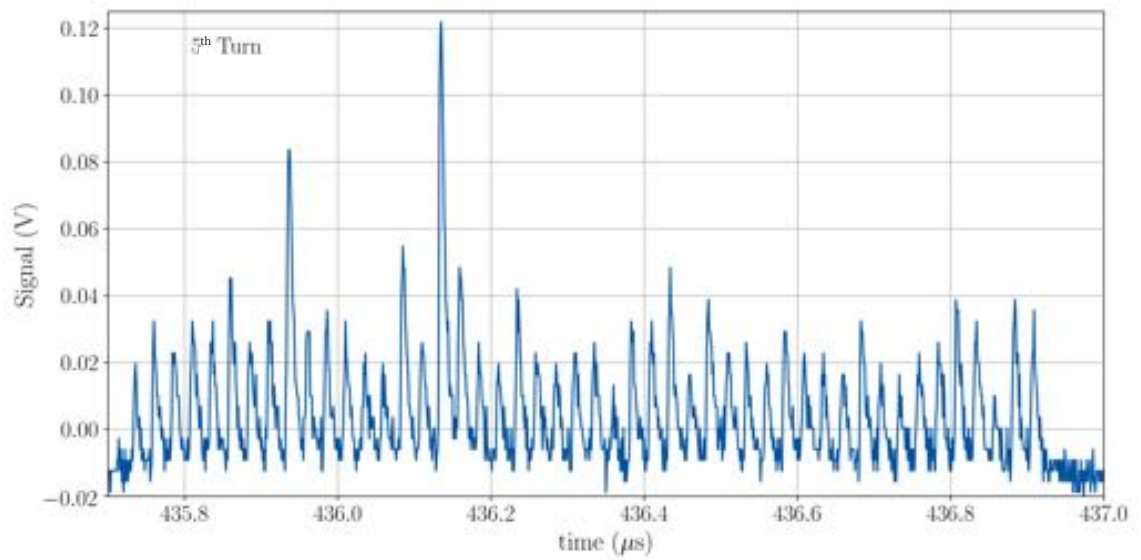
Figure 72: Zoom into the data of the 5th turn of the UFO loss signature, which is displayed in Fig. 70. The high resolution data allows the analysis of losses from single bunches during a UFO event.

9 Discussion on the use of diamond based beam loss monitors for detecting ultra fast beam losses

The presented work shows that the diamond based beam loss monitors are an excellent tool for measuring ultra fast beam losses at the LHC. Former experiments have shown that the dBLMs are radiation tolerant [39]. Therefore these detectors can even be used in regions with continuously high radiation levels, as for example in the collimation region in IR 7 of the LHC where the dBLMs are used to measure the injection oscillations and global losses, see chapter 8.3.

In addition the dBLMs have a wide dynamic range, which allows the use these detectors in various locations in the LHC with very different loss amplitudes. The high sensitivity of single crystalline dBLMs allows the measurements of particle showers of single beam gas interactions, see chapter 8.2. A polycrystalline dBLM is used for measuring the losses in case of an asynchronous beam dump, where multiple nominal bunches are lost in the extraction region. The intensity impinging on the detector will be in the order of 10^7 particles, see chapter 8.1.

The most attractive characteristics of the dBLM is the excellent temporal resolution in the nanosecond regime. Therefore, these detectors were chosen for the measurements of the ultra fast beam losses in the context of this thesis. The analysis of the high resolution loss signatures, presented in chapter 7, revealed that the majority of the injection losses do not come from the injected bunch train itself but from particles populating the beam upstream and downstream of the nominal bunches. Even the losses of short bunch like structures were identified, e.g. the ghost bunches and the misplaced pilot bunches during an erratic injection. Based on this work it was decided to install additional diamond based beam loss monitors in the LHC's injector chain for detailed monitoring of the beam preparation. In summary, the work presented in this thesis highlights the benefits of a beam loss measurement system based on dBLMs in a storage ring with a dense filling pattern of short bunches with high particles intensities at highest energies.

10 Conclusion

In the scope of this thesis ultra fast beam losses were measured at the LHC to understand the underlying loss mechanisms. These losses can reach potentially dangerous levels within less than $270\,\mu s$, i.e. reaction time of the beam dumping system, and are for example caused by dust particles falling into the beam or by incorrect deflection due to fast changing fields of the kicker magnets. In order to resolve the signature of these particle losses diamond based beam loss monitors with nanosecond resolution were installed at different positions of the LHC.

A special focus was put on the injection loss measurements, which were limiting the LHC operation in 2015 and 2016. The high resolution measurements revealed that the majority of the losses originated from particles populating the incoming beam upstream and downstream of the train of nominal bunches. These particles pass the injection kicker magnets when the magnetic fields do not have the nominal strength, which then results in an incorrect deflection of particles and ultimately to high losses. Up to 3.5×10^{10} particles were lost in the injection region. The optimisation of the beam preparation in the injector chain led to a reduction of the unsynchronised particles and thus to a reduction of the injection losses by one order of magnitude. In addition it was shown that the high time resolution loss signatures allow a much faster identification of the driving loss mechanism in case of erratic losses during the beam injection.

Similar to the beam injection, kicker magnets are used to extract the beams in case of a beam dump. During the extraction procedure ultra fast losses were observed due to particles populating the abort gap, which are then mis-steered by the changing kicker fields. From measurements of these losses the loss amplitudes during an asynchronous beam dump were extrapolated. The setup of the diamond based beam loss monitors were optimised to enable recording of the very high losses that were expected during an asynchronous beam dump, without the loss of information from saturation effects.

In addition it was demonstrated that beam gas interactions can be measured with a dedicated setup of diamond based detectors, which can be used for monitoring the particle population in the abort gap in the future.

In summary, the work presented in this thesis illustrates that the analysis of high resolution beam loss measurements provide a better understanding of the underlying loss mechanisms of ultra fast beam losses. Based on this knowledge loss mitigation techniques can be developed which contributes to better accelerator safety and availability.

Abbreviations and acronyms

CERN	European organization for nuclear research
LHC	Large Hadron Collider
PSB	Proton synchrotron booster
PS	Proton synchrotron
SPS	Super proton synchrotron
RF	Radio frequency
IR	Insertion region
BLM	Beam loss monitor
icBLM	Ionisation chamber beam loss monitor
dBLM	Diamond based beam loss monitor
pCVD	polycrystalline chemical vapour deposition
sCVD	single crystalline chemical vapour deposition
CCE	Charge collection efficiency
CCD	Charge collection distance
MIP	Minimum ionising particle
BTF	Beam test facility
MKE	Extraction kicker magnet in the SPS
MKI	Injection kicker magnet in the LHC
TDI	Internal absorber in the injection region
TCP	Primary collimator at the LHC
TCDQ	Absorber block protecting the superconducting quadrupole downstream of the extraction magnets
AG	Abort gap
BGI	Beam gas ionisation monitor
UFO	Unknown falling object

Acknowledgements

References

[1] J. Blanco Sancho, F. Burkart, D. Grenier, R. Schmidt, and D. Wollmann, "Results of an Experiment on Hydrodynamic Tunnelling at the SPS HiRadMat High Intensity Proton Facility", in Proceedings of IPAC (2013), http://epaper.kek.jp/IPAC2013/papers/moodb103.pdf.

[2] R. Schmidt, R. Assmann, E. Carlier, B. Dehning, R. Denz, et al., "Protection of the CERN Large Hadron Collider", New Journal of Physics **8**, 290 (2006) DOI: 10.1088/1367-2630/8/11/290, http://stacks.iop.org/1367-2630/8/i=11/a=290?key=crossref.a37bbcb24db3160b5ac78ed7e00b6657.

[3] O. Brüning, P. Collier, P. Lebrun, M. Stephen, R. Ostojic, et al., "LHC Design Report" (CERN, Geneva, Switzerland, 2004), DOI: 10.5170/CERN-2004-003-V-1, http://cds.cern.ch/record/782076?ln=en.

[4] *LHC Logbook*, https://op-webtools.web.cern.ch/elogbook/.

[5] CERN, *Accelerator Performance and Statistics*, https://acc-stats.web.cern.ch/acc-stats/{\#}lhc/overview-panel (visited on 07/01/2017).

[6] B. Muratori and W. Herr, "Concept of luminosity", (2006) DOI: 10.5170/CERN-2006-002.361, https://cds.cern.ch/record/941318?ln=de.

[7] J.-L. Caron, *Cross section of LHC dipole*, 1998, https://cds.cern.ch/record/841539?ln=en (visited on 01/25/2017).

[8] E. Courant and H. Snyder, "Theory of the alternating-gradient synchrotron", Annals of Physics **3**, 1 (1958) DOI: 10.1016/0003-4916(58)90012-5, http://linkinghub.elsevier.com/retrieve/pii/0003491658900125.

[9] F. Hinterberger, "Physik der Teilchenbeschleuniger und Ionenoptik" (Springer Berlin Heidelberg, 2008), http://www.springer.com/de/book/9783540752813.

[10] K Ehret, M Funcke, S Issever, T Jagla, T Lohse, et al., "Observation of coasting beam at the HERA proton-ring", Nuclear Instruments and Methods in Physics Research Section A: Accelerators, Spectrometers, Detectors and Associated Equipment **456**, 206 (2001) DOI: 10.1016/S0168-9002(00)00588-X, http://linkinghub.elsevier.com/retrieve/pii/S016890020000588X.

[11] R. W. Assmann, F. Zimmermann, F. Schmidt, and M. P. Zorzano-Mier, "Equilibrium Beam Distribution and Halo in the LHC", in 8th European Particle Accelerator Conference (2002), https://cds.cern.ch/record/569470?ln=de.

[12] M. Solfaroli, "LHC Operation and Efficiency in 2015", in LHC Performance Workshop, (2016), https : / / indico . cern . ch / event / 448109 / contributions / 1942062 / attachments / 1216263/1794003/LHC{_}operation{_}and{_}efficiency{_}MS.pdf.

[13] K. Fuchsberger, "Turnaround: Analysis and possible improvements", in 7th Evian Workshop (2016), https : / / indico . cern . ch / event / 578001 / contributions / 2366287 / attachments / 1370581/2276699/turnaround-analysis-improvements-paper.pdf.

[14] R. Schmidt, "Machine Protection", in *CAS - CERN Accelerator School: Advanced Accelerator Physics Course* (Trondheim, Norway, 2016), DOI: 10.5170/CERN-2014-009.221, https://cds.cern.ch/record/1982423.

[15] S. Rowan, "LHC main dipole magnet circuits: sustaining near-nominal beam energies", PhD thesis (University of Glasgow, 2016), https://cds.cern.ch/record/2229989?ln=de.

[16] A. Bertarelli, "Updated robustness limits for collimator materials", in Proceedings of MMP Workshop (2013), https://indico.cern.ch/event/227895/.

[17] A. Infantino, R. G. Alia, and M. Brugger, "Monte Carlo Evaluation of Single Event Effects in a Deep-Submicron Bulk Technology: Comparison Between Atmospheric and Accelerator Environment", IEEE Transactions on Nuclear Science **64**, 596 (2017) DOI: 10.1109/TNS.2016.2621238, http://ieeexplore.ieee.org/document/7676310/.

[18] B. Puccio, A. Castañeda Serra, M. Kwiatkowski, I. Romera Ramirez, and B. Todd, "The CERN Beam Interlock System: Principle and Operational Experience Backbone of the Machine Protection", in Proceedings of IPAC (2010),

[19] E. Ciapala, R. Schmidt, J. Wenninger, and F. Rodríguez-Mateos, "The LHC Post-mortem System", tech. rep. (CERN, Geneva, Switzerland, 2002), https://cds.cern.ch/record/691828?ln=de.

[20] O. O. Andreassen, V. Baggiolini, A. Castaneda, R. Gorbonosov, D. Khasbulatov, et al.,
"The LHC Post Mortem Analysis Framework", in 12th International Conference on Accelerator and Large Experimental Physics Control Systems (2009),
https://cds.cern.ch/record/1235888/files/CERN-ATS-2010-009.pdf.

[21] A. Arauzo Garcia, B. Dehning, G. Ferioli, and E. Gschwendtner,
"LHC Beam Loss Monitors", in 5th European Workshop on Diagnostics and Beam Instrumentation (2001),
DOI: 10.5170/CERN-2016-002.303,
https://cds.cern.ch/record/509291?ln=en.

[22] M. Stockner, B. Dehning, C. Fabjan, E. Holzer, C. Fabjan, et al.,
"Classification of the LHC BLM Ionization Chamber", in 8th European Workshop on Beam Diagnostics and Instrumentation for Particle Accelerators (2007),
https://cds.cern.ch/record/1045385?ln=en.

[23] A. Lechner, C. Bracco, V. Vlachoudis, A. Alnuaimi, F. Cerutti, et al.,
"Energy Deposition Studies for Fast Losses during LHC Injection Failures", in Proceedings of IPAC (2013),
https://cds.cern.ch/record/1636176?ln=en.

[24] E. Nebot Del Busto, G. Kruk, A. Nordt, C. Roderick, M. Sapinski, et al.,
"Handling of BLM abort thresholds in the LHC", in Proceedings of IPAC (2011),
https://cds.cern.ch/record/1379461?ln=en.

[25] E. B. Holzer, B. Dehning, E. Effinger, J. Emery, C. F. Hajdu, et al.,
"COMMISSIONING AND OPTIMIZATION OF THE LHC BLM SYSTEM", in Proceedings of HB (2010),
http://accelconf.web.cern.ch/Accelconf/HB2010/papers/weo1c01.pdf.

[26] H. Nyquist,
"Certain Topics in Telegraph Transmission Theory", Transactions of the American Institute of Electrical Engineers **47**, 617 (1928)
DOI: 10.1109/T-AIEE.1928.5055024,
http://ieeexplore.ieee.org/document/5055024/.

[27] D. Alves, S. Jackson, and I. Rodis,
"A monitoring system for the beam-based feedbacks in the LHC", in 2016 IEEE-NPSS Real Time Conference (RT) (2016),
DOI: 10.1109/RTC.2016.7543107,
http://ieeexplore.ieee.org/document/7543107/.

[28] P Baudrenghien and T Mastoridis,
"The LHC RF 2011 and beyond", in 3rd Evian Workshop on LHC beam operation (2012),
https://cds.cern.ch/record/1975497?ln=de.

[29] M. Zerlauth, *FMCM sensitivity to EMC transients*, CERN, Geneva, Switzerland, 2011,
https://indico.cern.ch/event/146119/{\#}2-fmcm-sensitivity-to-emc-tran.

[30] G. Iadarola and G. Rumolo,
"Electron Cloud Effects", ICFA Beam Dyn.Newslett. **69**, 208 (2016),
http://inspirehep.net/record/1505682.

[31] G. Papotti, M. Albert, B. Auchmann, E. B. Holzer, M. Kalliokoski, et al.,
"Macroparticle-Induced Losses During 6.5 TeV LHC Operation", in Proceedings of IPAC (2016),
https://cds.cern.ch/record/2207376/files/tupmw023.pdf.

[32] T. Baer, J. Wenninger, and E. Elsen,
"Very Fast Losses of the Circulating LHC Beam, their Mitigation and Machine Protection", PhD thesis (Hamburg, 2013),
https://cds.cern.ch/record/1637966?ln=en.

[33] B. Hall, G. Burt, R. Apsimon, C. Lingwood, A. Tutte, et al.,
"Design and testing of a four rod crab cavity for High Luminosity LHC",
Physical Review Accelerators and Beams **20**, 012001 (2017)
DOI: 10.1103/PhysRevAccelBeams.20.012001,
https://link.aps.org/doi/10.1103/PhysRevAccelBeams.20.012001.

[34] H. Padamsee, J. Knobloch, and T. Hays,
"RF superconductivity for accelerators" (Wiley-VCH, 1998),
DOI: 10.1080/10506899008260746.

[35] K. Olive,
"Review of Particle Physics", Chinese Physics C **38** (2014)
DOI: 10.1088/1674-1137/38/9/090001,
http://stacks.iop.org/1674-1137/38/i=9/a=090001?key=crossref.47735154e79ac9c858085df9b5a1f93a.

[36] M. Guthoff and W. De Boer,
"Radiation Damage to the diamond-based Beam Condition Monitor of the CMS Detector at the LHC", PhD thesis (Karlsruhe U., EKP, 2014),
https://cds.cern.ch/record/1977429?ln=de.

[37] C. Canali, E. Gatti, S. Kozlov, P. Manfredi, C. Manfredotti, et al.,
"Electrical properties and performances of natural diamond nuclear radiation detectors", Nuclear Instruments and Methods **160**, 73 (1979)
DOI: 10.1016/0029-554X(79)90167-8,
http://linkinghub.elsevier.com/retrieve/pii/0029554X79901678.

[38] C. Weiss, G. Badurek, E. Griesmayer, and C. Guerrero,
"A CVD Diamond Detector for (n,a) Cross-Section Measurements", PhD thesis (Technischen Universität Wien, Austria, 2014),
https://cds.cern.ch/record/1752629?ln=de.

[39] W. de Boer, J. Bol, A. Furgeri, S. Mueller, C. Sander, et al.,
"Radiation hardness of diamond and silicon sensors compared", physica status
solidi (a) **204**, 3004 (2007)
DOI: 10.1002/pssa.200776327,
http://doi.wiley.com/10.1002/pssa.200776327.

[40] C. F. Powell, J. H. Oxley, J. M. Blocher, and J. Klerer,
"Vapor Deposition", Journal of The Electrochemical Society **113**, 266C (1966)
DOI: 10.1149/1.2423765,
http://jes.ecsdl.org/cgi/doi/10.1149/1.2423765.

[41] B. Dehning, E. Effinger, H. Frais-Kolbl, D. Dobos, E. Griesmayer, et al.,
"Test of a Diamond Detector Using Unbunched Beam Halo Particles", tech.
rep. (2010),
https://cds.cern.ch/record/1258407?ln=en.

[42] B. Bounomo, C. Di Giulio, L. Foggetta, and P. Valente, *DAFNE Beam-Test
Facility INFN Frascati, Italy*,
http://www.lnf.infn.it/acceleratori/btf/ (visited on 01/20/2016).

[43] L. Foggetta, B. Buonomo, and P. Valente,
"Beam Optimization of the Daphne Beam Test Facility", in Proceedings of
IPAC (2015),
http://jacow.org/IPAC2015/papers/mopha048.pdf.

[44] M. Stockner,
"Beam Loss Calibration Studies for High Energy Proton Accelerators", PhD
thesis (Technische Universität Wien, 2007),
https://cds.cern.ch/record/1144077?ln=en.

[45] E. Griesmayer, *CIVIDEC Instrumentation GmbH*, 2016,
cividec.at (visited on 02/09/2016).

[46] E. Effinger, B. Dehning, T. Baer, R. Schmidt, H. Frais-Kölbl, et al.,
"A Prototype Readout System for the Diamond Beam Loss Monitors at LHC",
in Proceedings of IBIC (2013),
https://cds.cern.ch/record/1743060/files/mopc45.pdf.

[47] M. Hempel, W. Lohmann, and R. Schmidt,
"Application of Diamond Based Beam Loss Monitors at LHC", Master thesis
(Brandenburg Tech. U., 2013),
https://cds.cern.ch/record/1547086?ln=de.

[48] A. Bell, E. Castro, R. Hall-Wilton, W. Lange, W. Lohmann, et al.,
"Fast beam conditions monitor BCM1F for the CMS experiment", Nuclear
Instruments and Methods in Physics Research Section A: Accelerators, Spec-
trometers, Detectors and Associated Equipment **614**, 433 (2010)
DOI: 10.1016/j.nima.2009.12.056,
http://arxiv.org/abs/0911.2480.

[49] E. Griesmayer, E. Effinger, H. Pernegger, D. Dobos, and B. Dehning,
"A Fast CVD Diamond Beam Loss Monitor for LHC", in 10th European
Workshop on Beam Diagnostics and Instrumentation for Particle Accelera-
tors (2011),
https://cds.cern.ch/record/1528616?ln=de.

[50] F. Burkart,
"Expected damage to accelerator equipment due to the impact of the full
LHC beam: beam instrumentation, experiments and simulations", PhD thesis
(University of Frankfurt, 2016),
https://cds.cern.ch/record/2229595?ln=de.

[51] P Baudrenghien,
"The LHC RF: Operation 2010 and Plans for 2011", in 2nd Evian 2010 Work-
shop on LHC Beam Operation (2010),
https://cds.cern.ch/record/1359151?ln=en.

[52] K. HANKE,
"Past and Ppresent Operation of the CERN PS Booster", International Jour-
nal of Modern Physics A **28**, 1330019 (2013)
DOI: 10.1142/S0217751X13300196,
http://cds.cern.ch/record/1709399?ln=en.

[53] E. Metral, T. Argyropoulos, H. Bartosik, N. Biancacci, X. Buffat, et al.,
"Beam Instabilities in Hadron Synchrotrons", English, IEEE Transactions on
Nuclear Science **63**, 1001 (2016)
DOI: 10.1109/TNS.2015.2513752,
http://ieeexplore.ieee.org/articleDetails.jsp?arnumber=7445885.

[54] H. Burkhardt,
"Do We Need Collimation in the Transfer Lines?", in Workshop on LHC per-
formance (2003),
https://cds.cern.ch/record/642469?ln=de.

[55] V. Kain,
"Machine Protection and Beam Quality during the LHC Injection Process",
PhD thesis (Universität Wien, 2005),
https://cds.cern.ch/record/902813/files/thesis-2005-047.pdf.

[56] L. Drosdal, V. Kain, and S. Stapens,
"LHC Injection Beam Quality During LHC Run I", PhD thesis (University of
Oslo, 2015),
https://cds.cern.ch/record/2118801?ln=de.

[57] W. Hofle,
"Progress In Transverse Feedbacks and Related Diagnostics for Hadron Ma-
chines", in Proceedings of IPAC (2013),
http://cds.cern.ch/record/1595483?ln=en.

[58] B. Goddard, R. Riffaud, M. Sans-Merce, and W Weterings, "Conceptual Design of the LHC Beam Dumping Protection Elements TCDS and TCDQ", in Proceedings of 9th European Particle Accelerator Conference (2004),
https://cds.cern.ch/record/789994?ln=en.

[59] J. Uythoven, E. Bravin, D. Jacquet, A. Boccardi, W. Höfle, et al., "Abort Gap Cleaning for LHC Run 2", in Proceedings of IPAC (2014),
https://cds.cern.ch/record/2003159?ln=en.

[60] M Meddahi, A. S. Fisher, D Valuch, G. H. Hemelsoet, D Jacquet, et al., "LHC Abort Gap Monitoring and Cleaning", in Proceedings of IPAC (2010),
https://cds.cern.ch/record/1277630?ln=en.

[61] F. Burkart, "Expected damage to accelerator equipment due to the impact of the full LHC beam: beam instrumentation, experiments and simulations", PhD thesis (University of Frankfurt, 2016),
https://cds.cern.ch/record/2229595?ln=de.

[62] O. Stein, F. Burkart, B. Dehning, R. Schmidt, C. Buhl Sorensen, et al., "Response of Polycrystalline Diamond Particle Detectors Measured with a High Intensity Electron Beam", in Proceedings of IPAC (2015),
http://accelconf.web.cern.ch/AccelConf/IPAC2015/papers/mopty058.pdf.

[63] E. Bravin, G. Burtin, F. Roncarolo, A. Jeff, A. Fisher, et al., "First Beam Measurements with the LHC Synchrotron Light Monitors", in Proceedings of IPAC (2010),
https://cds.cern.ch/record/1271742?ln=en.

[64] O. Stein, F. Burkart, B. Dehning, R. Schmidt, C. Buhl Sorensen, et al., "Feasibility Study of Monitoring the Population of the CERN-LHC Abort Gap with Diamond Based Particle Detectors", in Proceedings of IPAC (2015),
http://accelconf.web.cern.ch/AccelConf/IPAC2015/papers/mopty057.pdf.

[65] T. Baer, F. Zimmermann, V. Vlachoudis, C. Zamantzas, J. Wenninger, et al., "UFOs in the LHC: Observations, studies and extrapolations", in 3rd Evian Workshop on LHC beam operation, (2011),
https://cds.cern.ch/record/1975492?ln=en.